NUREG/CR-1516
LA-8299-PR

Progress Report

Nuclear Reactor Safety

Quarterly Progress Report

October 1—December 31, 1979

University of California

LOS ALAMOS SCIENTIFIC LABORATORY
Post Office Box 1663 Los Alamos, New Mexico 87545

The four most recent reports in this series, unclassified, are NUREG/CR-0762 LA-7769-PR, NUREG/CR-0868 LA-7867-PR, NUREG/CR-0993 LA-7968-PR, and NUREG/CR-1201 LA-8171-PR.

This report was not edited by the Technical Information staff.

Work supported by the US Department of Energy, Division of Reactor Development and Demonstration.

NUREG/CR-1516
LA-8299-PR
Progress Report
R4, R7, and R8

Nuclear Reactor Safety

Quarterly Progress Report

October 1—December 31, 1979

Compiled by

James F. Jackson
Michael G. Stevenson

Los Alamos Scientific Laboratory
Q (Energy) Division
William G. Davey, Division Leader
William L. Kirk, Alternate Division Leader

Manuscript submitted: March 1980
Date published: May 1980

Prepared for
Office of Nuclear Regulatory Research
Division of Reactor Safety Research
Office of Nuclear Reactor Regulation
Division of Systems Safety
US Nuclear Regulatory Commission
Washington, DC 20555

NRC FIN Nos.

D022	R287	R414	R670
D023	R403	R421	R672
D553	R404	R422	R680
R282	R411	R423	R682
R284	R413	R429	

UNITED STATES
DEPARTMENT OF ENERGY
CONTRACT W-7405-ENG. 36

CONTENTS

CONTENTS (cont)

CONTENTS (cont)

CONTENTS (cont)

FIGURES

FIGURES (cont)

FIGURES (cont)

FIGURES (cont)

FIGURES (cont)

TABLES

ABSTRACT

During the last quarter, work continued on development and verification of TRAC-PD2, the next release of a detailed TRAC version, and on development of TRAC-PF1, the first release of a faster, less detailed TRAC version. The new reflood model was installed in TRAC-PD2 and testing was initiated. A coarse-mesh rebalance method for vessel calculations was implemented in PD2. This method allows substantial cost savings for cases in which pressure convergence must be extremely tight (10^{-7}) to control mass conservation errors. A new gap conductance model implemented for TRAC-PD2 was shown to improve significantly TRAC calculated peak clad temperatures in LOFT experiments. Several other analyses of experiments were completed successfully as part of TRAC-PD2 developmental assessment, including FLECHT and University of California (Berkeley) reflood tests, Semiscale Test S-06-3, and ORNL Thermal-Hydraulic Test Facility Test 177. As another part of TRAC assessment, pretest predictions for LOFT small-break test L3-1 and LOBI (Ispra) test A1-01 were completed. In applications of TRAC, further parametric calculations were performed to investigate variations of the TMI-2 accident scenario. As another TMI follow-on activity, a study was begun of other "multifault" accidents in LWRs. A catalog of multifault accidents was developed to provide a structure for further analyses using TRAC and other methods as appropriate.

In basic thermal-hydraulic model development, the non-equilibrium flashing model for critical two-phase flow already tested against Semiscale and Marviken experiments was further tested against data from low-pressure critical flow experiments. Data from multirod de-entrainment experiments at LASL were compared to an analytical correlation developed from single-rod experiments, with excellent agreement.

Work in LMFBR safety research continued with important results obtained from SIMMER-II analyses of transition-phase behavior in a Clinch River Breeder Reactor disruptive accident. These analyses indicate that transition-phase recriticalities are likely unless core material can find escape paths that lead to large negative reactivities. Also, these analyses involving large motions of core materials indicated a sensitivity to the neutronics treatment, i.e., diffusion or transport theory. Analyses of Purdue-Omega nitrogen blowdown experiments provided additional confirmation that purely fluid dynamics effects can be modeled adequately with SIMMER-II. Similar analyses of Purdue-Omega flashing water blowdown experiments were successfully completed only with the addition of a number-density-dependent

bubbly flow regime model. Phase I of the LASL Upper Structure Dynamics experimental program ended with the successful completion of four tests using Freon-113 as core material simulant blowing down into a simulated LMFBR upper subassembly. SIMMER-II analyses of these tests are in progress.

In HTGR safety research, two- and three-dimensional finite element models were used to calculate thermal stresses in the Fort St. Vrain Core Support Blocks during a Firewater Cooldown accident. The thermal stresses in all cases did not exceed the minimum ultimate tensile strength of the graphite structural material.

The first coupled convective heat transfer and rod bowing analyses for the GCFR cladding melting and relocation tests were performed. A quantitative analytical tool for studying heater-rod/spacer-grid interaction is now close at hand. The large Guarded Core Module pressure vessel was installed in the high bay. This is a major milestone in preparation for performing the cladding melting tests on full subassemblies with additional guard rows of pins.

NUCLEAR REACTOR SAFETY

Compiled by

James F. Jackson and Michael G. Stevenson

I. INTRODUCTION

(M. G. Stevenson, Q-DO)

This quarterly report summarizes technical progress from a continuing nuclear reactor safety research program conducted at the Los Alamos Scientific Laboratory (LASL). The reporting period is from October 1 to December 31, 1979. This research effort concentrates on providing an accurate and detailed understanding of the response of nuclear reactor systems to a broad range of postulated accident conditions. The bulk of the funding is provided by the US Nuclear Regulatory Commission (NRC), with part of the advanced reactor work funded by the US Department of Energy (DOE).

The report is mainly organized according to reactor type. Major sections deal with Light-Water Reactors (LWRs), Liquid Metal Fast Breeder Reactors (LMFBRs), High-Temperature Gas-Cooled Reactors (HTGRs), and Gas-Cooled Fast Reactors (GCFRs).

The research discussed was performed by several technical divisions and groups within LASL. The names and group affiliations of the individual staff members responsible for the work are given at the beginning of each section. Most of the work was performed in the reactor safety portion of the Energy (Q) Division. An organization chart showing the Q-Division groups with major reactor safety activities is presented on the following page. Other divisions contributing to the program were the Theoretical (T) Division and Dynamic Testing (M) Division.

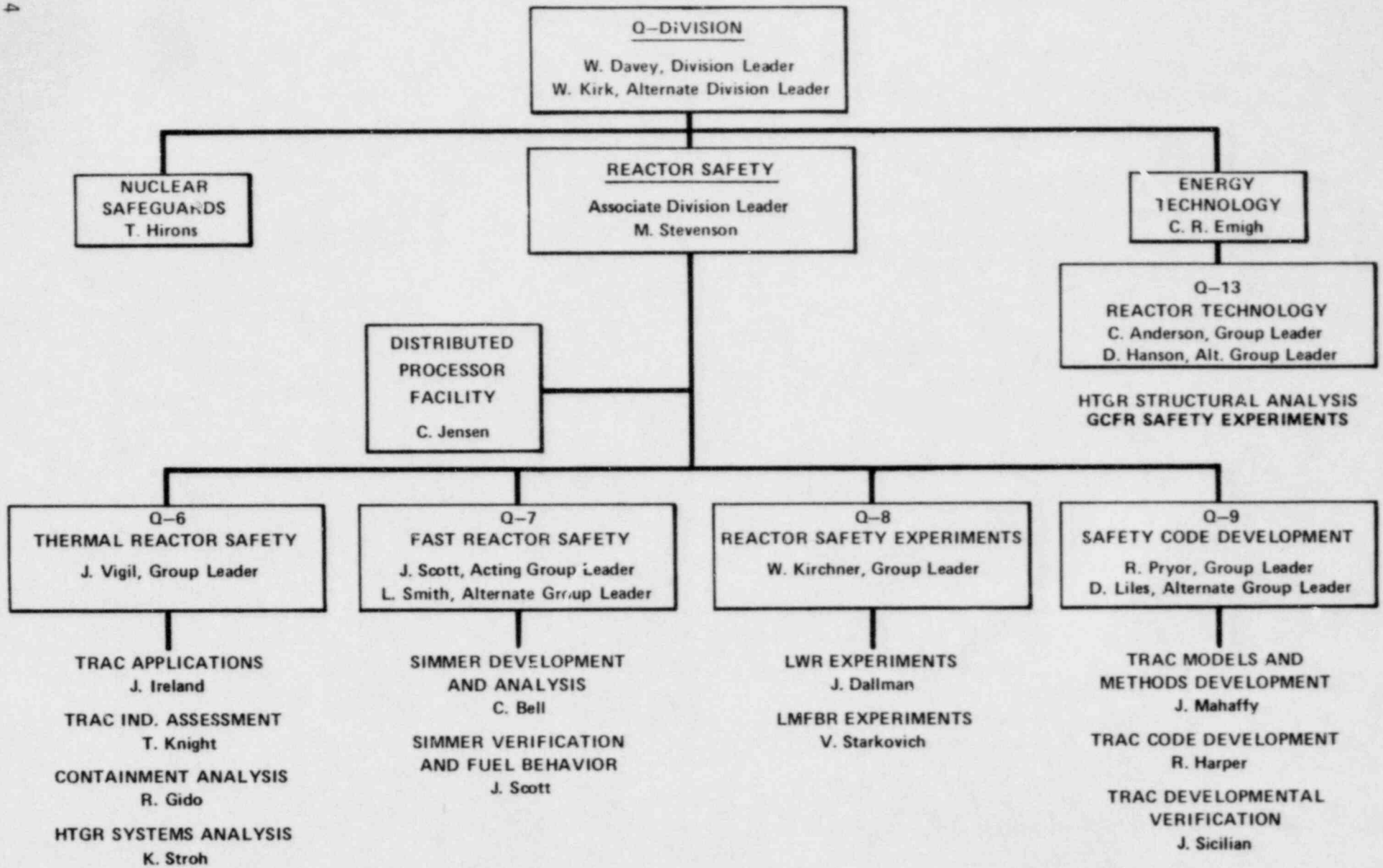
Q–DIVISION
W. Davey, Division Leader
W. Kirk, Alternate Division Leader
NUCLEAR SAFEGUARDS
T. Hirons
REACTOR SAFETY
Associate Division Leader
M. Stevenson
ENERGY TECHNOLOGY
C. R. Emigh
Q–13
REACTOR TECHNOLOGY
C. Anderson, Group Leader
D. Hanson, Alt. Group Leader
HTGR STRUCTURAL ANALYSIS
GCFR SAFETY EXPERIMENTS
DISTRIBUTED PROCESSOR FACILITY
C. Jensen
Q–6
THERMAL REACTOR SAFETY
J. Vigil, Group Leader
Q–7
FAST REACTOR SAFETY
J. Scott, Acting Group Leader
L. Smith, Alternate Group Leader
Q–8
REACTOR SAFETY EXPERIMENTS
W. Kirchner, Group Leader
Q–9
SAFETY CODE DEVELOPMENT
R. Pryor, Group Leader
D. Liles, Alternate Group Leader
TRAC APPLICATIONS
J. Ireland
TRAC IND. ASSESSMENT
T. Knight
CONTAINMENT ANALYSIS
R. Gido
HTGR SYSTEMS ANALYSIS
K. Stroh
SIMMER DEVELOPMENT AND ANALYSIS
C. Bell
SIMMER VERIFICATION AND FUEL BEHAVIOR
J. Scott
LWR EXPERIMENTS
J. Dallman
LMFBR EXPERIMENTS
V. Starkovich
TRAC MODELS AND METHODS DEVELOPMENT
J. Mahaffy
TRAC CODE DEVELOPMENT
R. Harper
TRAC DEVELOPMENTAL VERIFICATION
J. Sicilian

II. LWR SAFETY RESEARCH

(J. F. Jackson, DAD/NRC and M. G. Stevenson, Q-DO)

Five major projects in LASL's light-water reactor safety research program are reported in this section. The first is the development and testing against experimental data of the Transient Reactor Analysis Code (TRAC). The second concentrates on the application of TRAC to the multinational 2D/3D LWR safety research program. The third area focuses on the independent assessment of the TRAC code by performing blind predictions of pertinent experiments. The fourth project involves component code development and thermal-hydraulic research in key LWR safety problem areas. The fifth, and final effort, is an experimental program that supports model development activities and provides advanced instrumentation for reactor safety experiments.

A. TRAC Code Development and Assessment

(R. J. Pryor, Q-9)

TRAC is an advanced, best estimate computer program for the analysis of postulated accidents in LWRs. It features a nonhomogeneous, nonequilibrium, multidimensional fluid dynamics treatment; detailed heat transfer and reflood models; and a flow-regime-dependent constitutive equation package to describe the basic physical phenomena that occur under accident conditions. It calculates initial steady-state conditions and complete accident sequences.

The first version of TRAC, completed in December 1977 and called TRAC-P1, is primarily directed toward loss-of-coolant accidents (LOCAs) in pressurized water reactors (PWRs). A refinement of this version, called TRAC-P1A, was released to the National Energy Software Center (NESC) in March 1979. An improved version, designated TRAC-PD2, will be released in mid-1980. This code contains improved reflood and heat transfer models and improvements in the numerical solution strategy. A fast-running version called TRAC-PF1 will be released in late 1980. TRAC-PF1 will be capable of treating noncondensible gases and a

wide range of accident types, including transients similar to that which occurred during the Three Mile Island (TMI) incident. TRAC-PD3 will be released in 1981 and will provide detailed analyses of Anticipated Transients Without Scram (ATWS), Reactivity Insertion Accidents (RIAs), and operational transients.

As part of a closely coupled code assessment effort, all versions of TRAC are being applied to a broad range of water reactor safety experiments. These data comparisons are designed to evaluate code performance during all accident phases. TRAC posttest calculations are compared with experimental results to evaluate the thermal-hydraulic models in the code; pretest calculations are made to test predictive capability.

During the past quarter, the new reflood model was installed in TRAC-PD2 and testing was initiated. A new numerical method for problems containing vessels was installed to reduce computing cost and eliminate mass conservation errors. A new test problem set was defined and will be implemented next quarter. Development of TRAC-PF1 continued with the addition of models to treat two separate sets of field equations for one-dimensional components and an air field in all components. Development of the graphics postprocessor continued and will be included with the release of TRAC-PD2. Details of these efforts and other work follow.

1. Hydrodynamics and Heat Transfer

(D. R. Liles, Q-9)

During the quarter a new procedure for improving the convergence of the vessel pressure iteration was implemented and tested. Improvements were made in the TRAC minimum-film-boiling temperature correlation and in the rod-gap conductance model. Work continued on the addition of a noncondensible gas field for version PF1 and the metal-water reaction model in TRAC was improved. The Massachusetts Institute of Technology (MIT) neutronics code QUANDRY was implemented on the LASL computing system.

a. Coarse-Mesh Rebalance Method for Vessel Calculations

(R. J. Pryor and J. H. Mahaffy, Q-9)

The vessel pressure solution matrix is solved directly if the number of mesh cells (regions) in the vessel is sufficiently small, for example, less than 30. Otherwise, a Gauss-Seidel iteration algorithm is employed in which the pressures are solved by level, beginning at the bottom of the vessel. We have noticed that for cases requiring iteration, the prescribed convergence criteria of 10^{-5} in pressure could allow significant mass errors. Tightening the convergence tolerance to 10^{-7} eliminated the mass error but forced the iteration count to be enormously high.

To solve this problem, a vessel coarse-mesh rebalance method was devised. During the iteration the pressure solution is scaled nonuniformly to reduce the overall iteration error. Such scaling can be represented as

$$P'^{(i)} = S^{(i)} P^{(i)} , \tag{1}$$

where $P^{(i)}$ is the pressure solution vector after i iterations and $S^{(i)}$ is its scaling matrix. For our purposes, S is a diagonal matrix with elements s_j; that is s_j scales the j^{th} element of the vector P. We define a coarse-mesh region as those vessel regions having the same scale factor. The scaled solution vector P' can then be written as

$$P' = s_1 P_1 + s_2 P_2 + s_3 P_3 + \ldots , \tag{2}$$

where P_1 is a vector of pressures belonging to coarse-mesh region i and s_i are simple scalar quantities. Using this equation in the vessel pressure equation,

$$A \cdot P = B : \tag{3}$$

and requiring that the least-squares error of P' be a minimum yields the following equation for the scale factors.

$$U \cdot S = V \qquad (4)$$

where $U_{ij} = (P_i, AP_j)$ and $V_i = (P_i, B)$. The notation (X,Y) means the inner-product of the vectors X and Y. The matrix size of U is equal to the number of coarse-mesh regions.

The choice of coarse-mesh regions is extremely important. We have chosen a scheme that "follows" the flow path in the vessel; that is, the coarse-mesh regions are coupled to one another in the direction of flow. Use is made of the fact that the vessel matrix A is a seven-stripe matrix for a three-dimensional vessel and that coupling is only to nearest neighbors. There is no coupling if neighbors are separated by a wall, such as a downcomer boundary. Based on these facts, we infer the coarse-mesh regions as follows. All mesh cells on a level in the downcomer form a single coarse-mesh region. All other coarse-mesh regions are defined one per level, excluding regions in the downcomer. This prescription is illustrated in Fig. 1, where the total number of coarse-mesh regions is equal to the number of levels in the downcomer plus the total number of levels in the vessel. The resulting size of the U-matrix is normally small enough to be solved directly.

Although this choice of coarse-mesh regions is not unique, it may reduce the number of vessel iterations; also, doing the coarse-mesh rebalance after each Gauss-Seidel iteration for the pressure seems to work best. The effect of rebalancing is shown in Fig. 2 for a typical problem. Note that for a given pressure convergence criterion, the total number of iterations is greatly reduced using the coarse-mesh rebalancing method. The cost savings is substantial for the required convergence of 10^{-7}.

b. Minimum Stable Film Boiling Temperature

(D. A. Mandell, Q-9)

As previously indicated,[1] the minimum stable film boiling temperature (T_{min}) has a significant effect on loss-of-fluid test (LOFT) predictions (for example, see Ref. 2 for LOFT L2-3 predictions). A number of T_{min} correlations are compared in Ref. 1 and the Iloeje correlation was used for the predictions in Ref. 2. To assess the Iloeje correlation

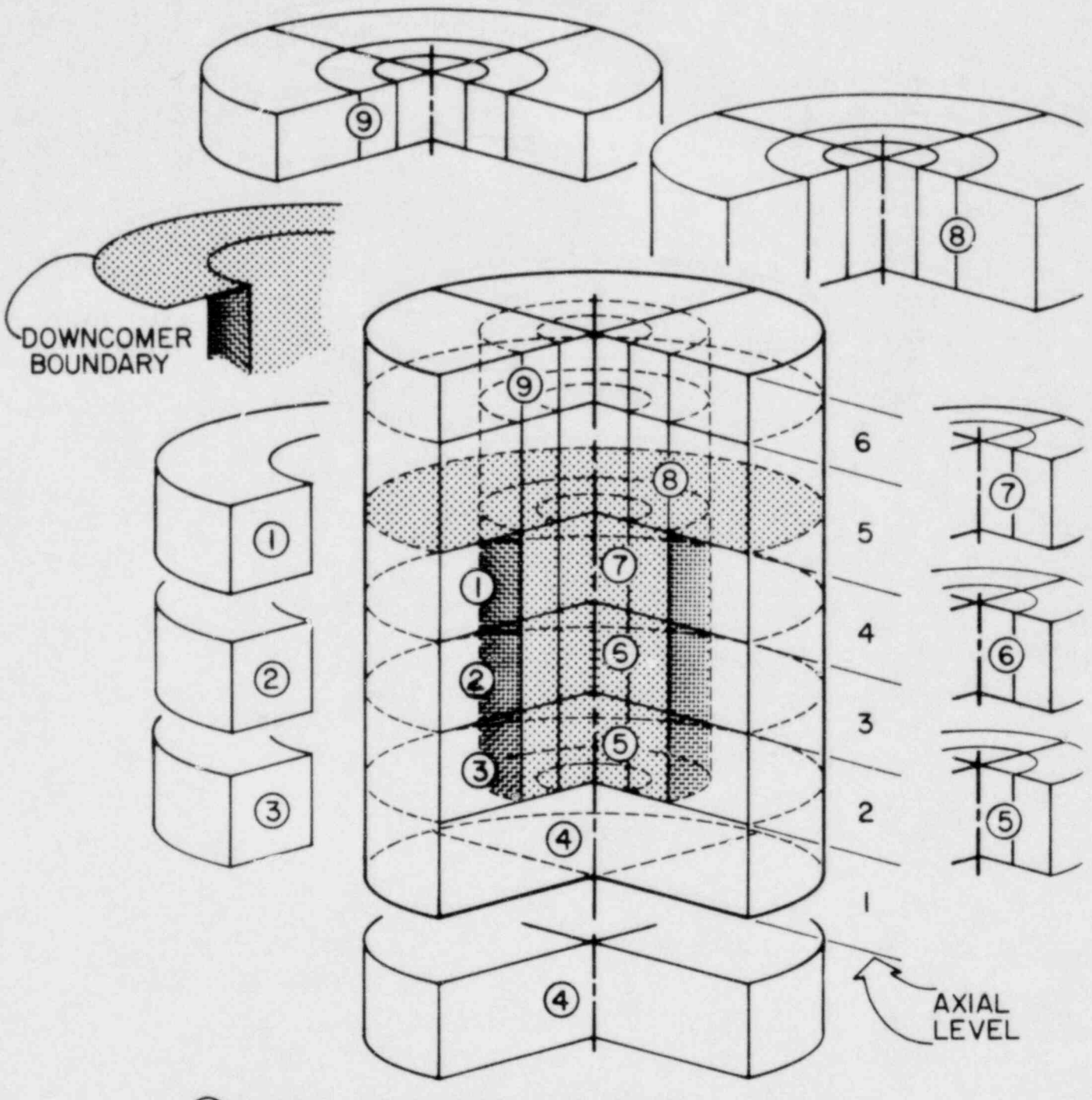

Fig. 1. Coarse-mesh region assignment.

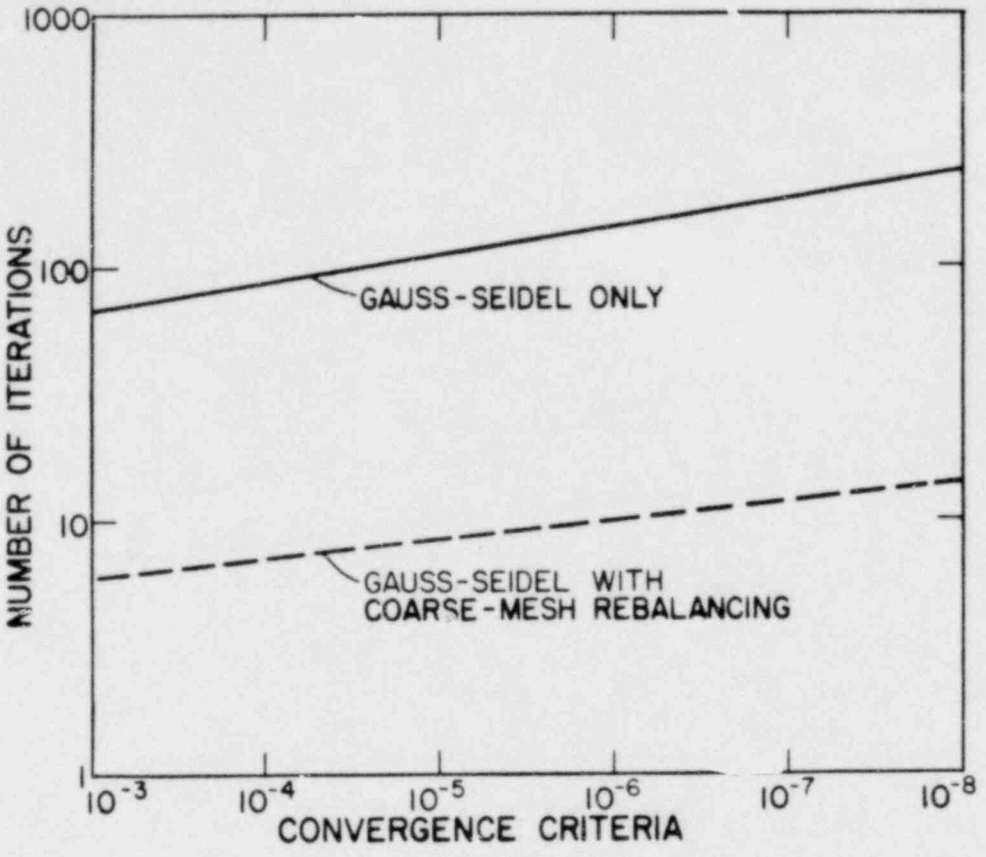

Fig. 2. Comparison of Gauss-Seidel iteration with coarse-mesh rebalancing.

further, TRAC analyses are being compared to data from other test facilities. This includes TRAC calculations with and without the Iloeje T_{min} correlation for Semiscale experiments and for the Oak Ridge Blowdown Facility experiments. Oak Ridge results are discussed in Sec. II.A.3.c.

Figure 3 shows a comparison of data and TRAC predictions for Standard Problem Five (Semiscale Test S-02-8).[3,4] Figure 3 shows three data curves at the axial midplane. The top and middle curves represent the band of data containing all of the thermocouple measurements. The lowest curve on Fig. 3 reflects a thermocouple that indicated a rewet. A number of the thermocouples faced the cold shroud; and thus radiative heat transfer, which is not modeled in TRAC, may have been important in reducing their temperatures. As would be expected, the TRAC predictions using the Iloeje T_{min} are lower than the predictions using the

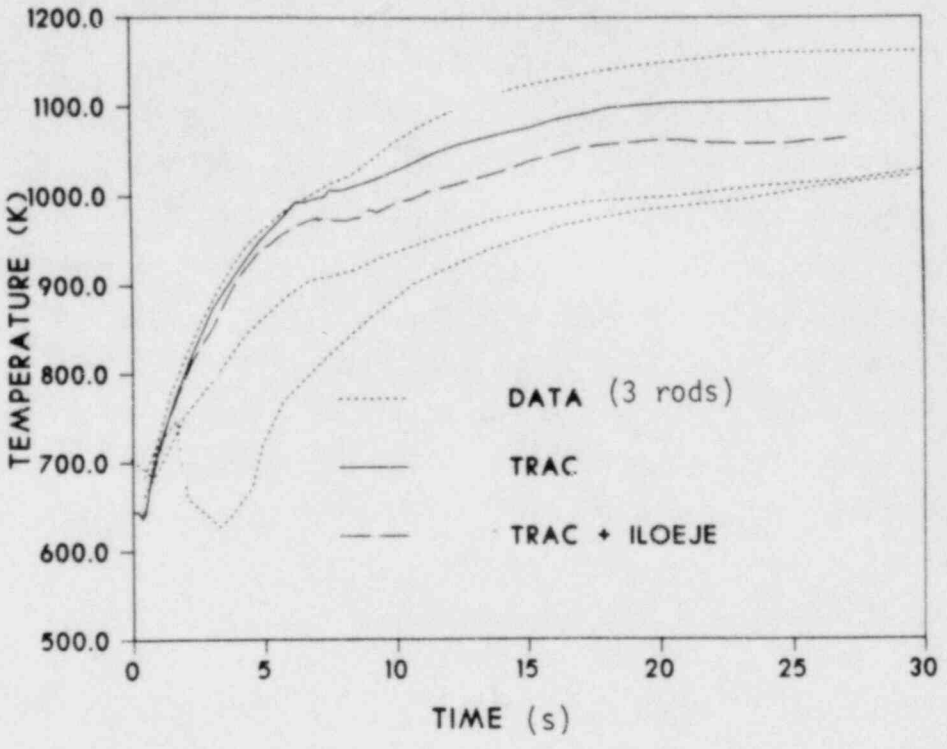

Fig. 3. Standard Problem Five clad temperature.

homogeneous nucleation T_{min}, but both calculations are within the data band.

Pending further assessment, the Iloeje T_{min} correlation has been implemented as an option in TRAC-PD2.

c. Gap Conductance

(D. A. Mandell and S. W. Hatch,* Q-9)

TRAC-P1A[5] contains a model in which the radial gas gap conductance is constant throughout the entire transient. The gap conductance changes only through the temperature effects on the gas thermal conductivity and the radiative heat transfer. TRAC-PD3 will utilize the FRAPCON code for steady-state gap conductance calculations and the FRAP-T code for the transient calculations.[6,7] An interim gap-conductance model has been developed for use in TRAC-PD2.

---

*Graduate Research Assistant. Present address: Sandia Laboratories, Nuclear Fuel Cycle Systems Division, Albuquerque, NM.

The interim model uses the uncoupled, quasi-static approximation for the fuel rod mechanical equations that omits the mechanical coupling term in the energy equation and the inertial term in the mechanical force balance. By neglecting these terms the influence of the strains in the fuel and clad on the temperature distribution are assumed to be small and that displacements are instantaneous. The fuel clad gap system is modeled in three regions as shown in Fig. 4. Gap changes are found by calculating the radial displacement of each region due to thermal expansion.

A solution for the uncoupled, quasi-static approximation[8] is used to calculate displacement in the solid fuel and clad regions. The calculations for the deformation of a hollow or solid circular cylindrical body of outer radius b and of height h are given in Ref. 8 for the case of plane strain where the ratio h/b is large compared to unity. Other assumptions are that the cylindrical surfaces are free of forces and that axial displacement is allowed. It should be noted also that because we are using the uncoupled, quasi-static approximation, the temperature distributions are assumed known from the energy balance.

The fuel pellet cracked region is assumed to start at a fixed, input radius, r'. A smooth parabolic temperature distribution is assumed across the pellet and is continuous at the solid fuel/cracked fuel boundary. (See Ref. 9 for the equation used to calculate cracked fuel displacement and Ref. 10 for details of the model.)

The fuel rod gap conductance generally exists only in nuclear fuel rods and not in electrically heated rods; thus, it is necessary to compare gap-conductance models with nuclear experiments. In the present work, TRAC-P1A calculations with and without the new gap-conductance model are compared to LOFT nuclear test L2-2 data.[11] The results for the midplane of the central module are shown in Fig. 5, where the new gap-conductance model is referred to as "DELTAR." Thirty per cent of the fuel was assumed cracked.

The new gap-conductance model affects the LOFT predictions only during two periods of the calculation (Fig. 5). The peak clad

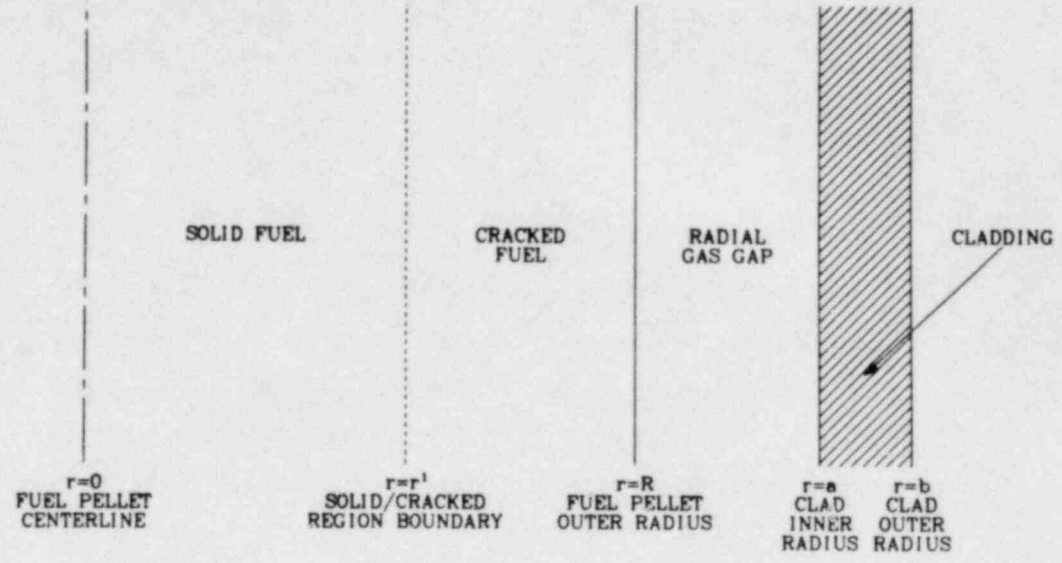

Fig. 4. Fuel clad gap configuration.

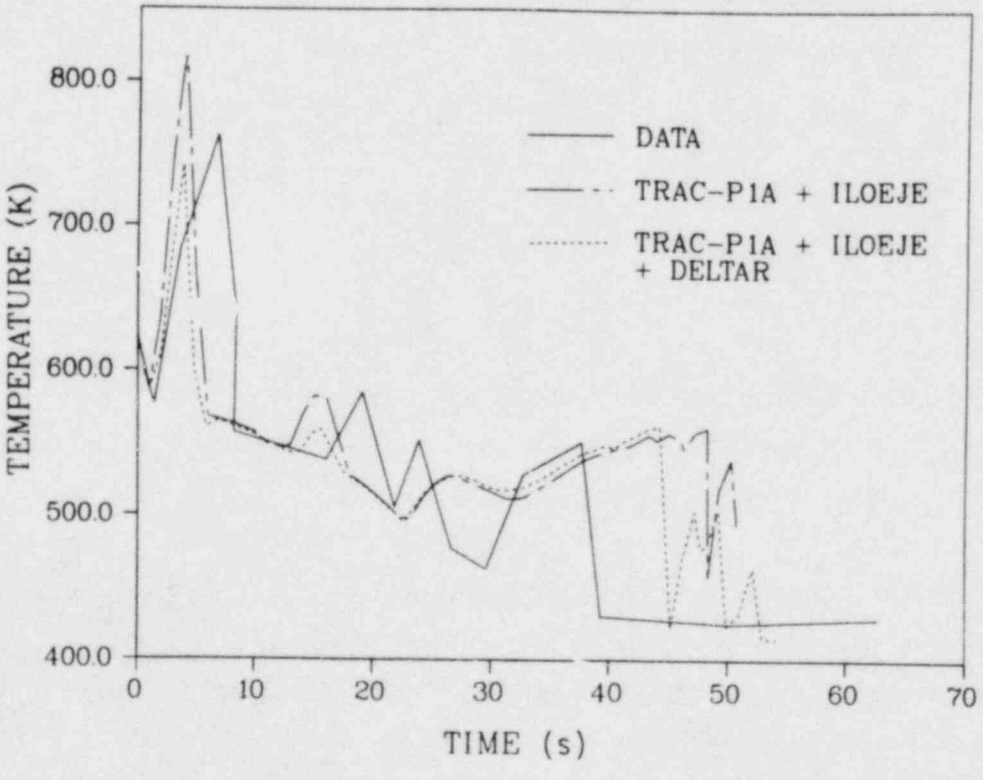

Fig. 5. Cladding temperature comparison for LOFT test L2-2.

temperature (PCT) prediction of TRAC-P1A early in the run is approximately 60 K above the data and the new model is about 20 K below the data. During the reflood portion of the transient, TRAC-P1A predicted reflood to occur 10 s later than the measurement, while the new model showed a 5-s improvement.

d. TRAC Analysis of Bennett Heated Tube Experiment

(D. A. Mandell and R. K. Fujita, Q-9)

The data used for these TRAC comparisons were taken from steady-state experiments performed by A. W. Bennett.[12] The experiments consisted of circulating preheated water through a tubular test section that was heated by passing direct current through its walls. Data were obtained to determine the variation of wall temperature in the region beyond the dryout point for various coolant flow rates, wall heat fluxes, and coolant inlet subcoolings.

The test section was constructed from a 5.8 m length of Nimonic 80-A alloy tubing. The tubing had an i.d. of 12.6 mm and a wall thickness of 1.63 mm. Busbars attached to the test section provided heated lengths of 3.66 and 5.56 m. The wall temperatures were monitored by 27 thermocouples attached to the outer wall of the test section.

The TRAC model for these tests consists of a fill, a break, and a pipe with 24 axial nodes. To achieve a steady-state solution, TRAC was run in a transient mode for 25 s [critical heat flux (CHF) is not allowed to occur when the steady-state option is selected in TRAC].

Figure 4 shows the wall temperature results as a function of axial position for Bennett run number 5442. In addition to the data, Fig. 6 shows three TRAC calculations -- TRAC-P1A, a recent TRAC-PD2 internal version (denoted TRAC 23.0), and TRAC-PD2 using the Bowring CHF correlation (solid line), which is not a permanent part of TRAC-PD2. The mass flux is high in this case, so only the Biasi CHF correlation is used and not the low-flow Zuber correlation. Part of the tube is in nucleate boiling and part in film boiling, and therefore, the results are independent of the minimum stable film boiling temperature used.

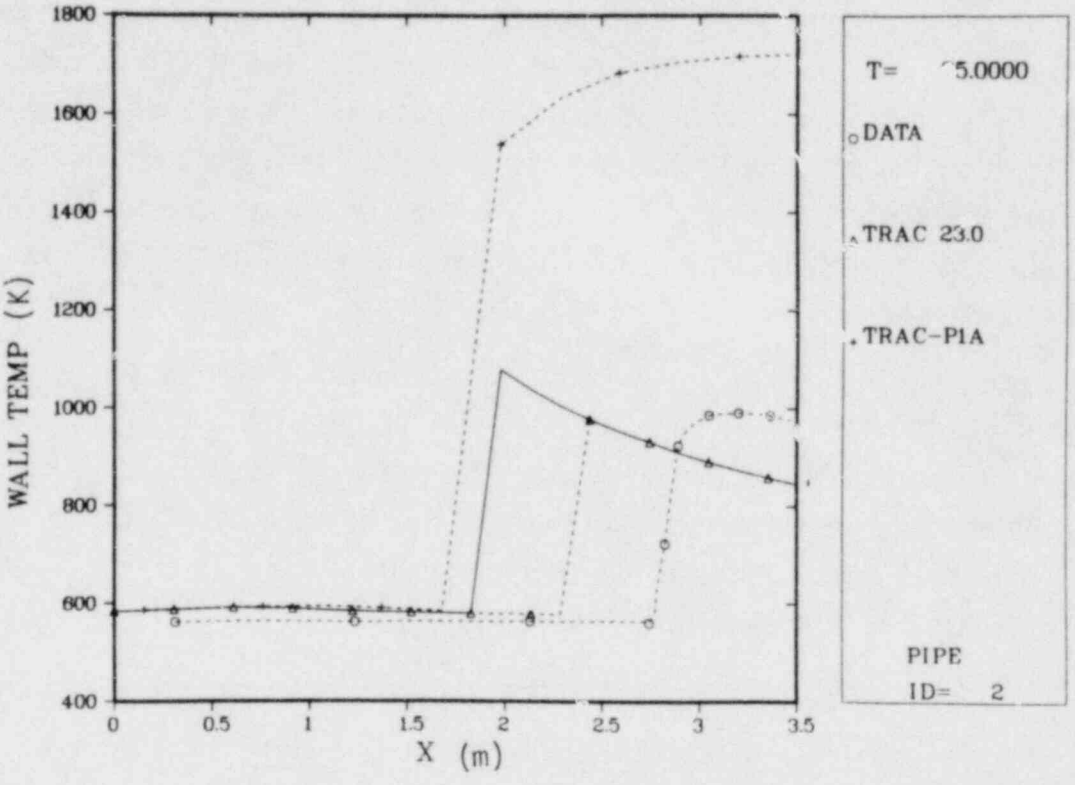

Fig. 6. TRAC comparisons to Bennett Experiment No. 5442.

The TRAC-PD2 results using the Biasi CHF correlation are in much better agreement with the data than the TRAC-P1A results, due to an interfacial area error in TRAC-P1A. The Biasi correlation gives better agreement with the data than the Bowring CHF correlation.

e. Addition of a Noncondensible Gas Field

(S. B. Woodruff and D. R. Liles, Q-9)

We are now verifying the noncondensible gas (air) field added for TRAC-PF1. All code structure changes have been made to account for the addition of air to the input, restart, dump, edit, and graphics routines; also we have implemented changes for the addition of air to the calling sequences of the thermodynamic and constitutive properties routines. In addition, the appropriate source terms and boundary data arrays have been modified.

A vessel test problem was modified to run as an all-air (void fraction of 1.0, steam pressure of 0.0) problem and was executed successfully. Further tests are being made on the new code version. A comparison is planned for results obtained using the original code version with the air-liquid water option. This testing stage will then be followed by an extensive assessment study.

f. Space-Time Neutronics Development

(J. M. Sicilian, Q-9)

The nodal space-time diffusion theory neutronics program, QUANDRY, has been converted to execute on the LASL CDC-7600 and CRAY-1 computers. Comparison of test problems with results from IBM calculations indicates that QUANDRY is executing correctly on both systems.

g. Improved Metal-Water Reaction Model

(S. B. Woodruff, Q-9)

The metal-water reaction model in TRAC has been updated to conform to the recommendation in MATPRO-11.[13] In addition, the time-integrated hydrogen production due to the metal-water reaction is calculated and printed.

2. Code Development

(J. M. Sicilian, Q-9)

The process of preparing TRAC-PD2 for release to the public began this quarter. Preparation also is being made for release of the graphics postprocessing programs EXCON and TRAP. These programs will be exported together with TRAC-PD2.

Plans are being formulated for a second TRAC workshop to be held February 4-7, 1980. Presentations will be made by the TRAC development team, primarily on TRAC-PD2, and by the users of TRAC-P1A. The workshop is designed to allow all those interested in TRAC to share their experiences.

a. New Test Problems

(J. M. Sicilian, Q-9)

The new test problems for use in code development have been completed this quarter. These are based on the following experiments.

- CISE (Tests R and 4). Both unheated and heated pipe blowdown results are utilized.
- Marviken (Test 4). Separate one- and three-dimensional models of this large tank blowdown test are included in the problem set.
- FLECHT (Test 1720). A portion of a single high-flooding rate test is included to test the reflood section of TRAC.
- LOFT Test L2-2. The test problems based on this experiment are

  steady state,

  pressurizer blowdown, and

  emergency core cooling (ECC) injection.
- Semiscale Test S-02-8. The operation of the steam generator and pump are studied during the blowdown phase of this experiment.

The test problems derived from Semiscale and LOFT are subsections of complete analyses of these experiments. These small problems execute much more cheaply than the full calculations, and therefore may be run for every new internal code version. Initial and boundary conditions for these problems are derived from full calculations, which are repeated as necessary.

As the goals of the TRAC development effort shift, additions and modifications to these problems will be made. In particular, as emphasis moves from the development of TRAC-PD2 to TRAC-PF1, analysis of small-break problems will be included.

b. Conversion of TRAC to CRAY

(R. P. Harper, Q-9)

The graphics section of TRAC is being converted to CRAY and fill processors are being developed to execute on the 7600. Upon completion, these processors will convert graphics files produced by TRAC running on the CRAY-1 to a format that can be read by the EXCON and TRAP postprocessors executing on the CDC machines. Moving files between machines is necessary until a complete graphics package becomes available on the CRAY-1 computers.

c. TRAP and EXCON Enhancements

(J. C. Ferguson and M. R. Turner, Q-9)

TRAP has been extended to handle the new fuel rod model implemented in TRAC-PD2. This required substantial revision of TRAP data management strategies. Detailed views of rod temperature profiles during reflood are now possible using TRAP.

The version of TRAP to be released with TRAC-PD2 is now complete. This program should be relatively easy for other sites to implement and will provide a flexible, interactive graphics ability to TRAC users. The package, as distributed, will use the commercial DISSPLA graphics package but could be converted to other high-level graphics systems.

EXCON is being modified to merge graphics files produced by separate executions of TRAC, edit specified components and time intervals, and control the data written to files to be processed by TRAP.

d. COMMON Block Reorganization

(J. R. Netuschil, Q-9)

Reorganization of COMMON information is being implemented in TRAC-PF1 to simplify conversion of TRAC to non-CDC systems and to improve the data structure of TRAC. Testing of the reorganized COMMON areas is now under way.

e. Documentation

(J. M. Sicilian, R. P. Harper, J. C. Ferguson, C. L. Trujillo, and M. R. Turner, Q-9)

Detailed documentation is being prepared for TRAC-PD2, EXCON, TRAP, HORSE, and the new test problems. These documents are generally divided into two sections: a user's guide and a programmer's manual.

f. New FILL Option

(S. B. Woodruff, Q-9)

Three new options have been added to the FILL component to allow specification of fixed mass flow, mass flow vs time, or mass flow vs pressure boundary conditions. This addition provides more accurate modeling of such experimental situations as pressurizer letdown.

3. TRAC Code Assessment

(J. K. Meier, Q-9)

During this quarter, we completed TRAC input descriptions of the FLECHT skewed power test, Semiscale Test S-06-3, and Oak Ridge National Laboratory (ORNL) Thermal Hydraulic Test Facility (THTF) Test 177. We also made a series of data comparisons of the improved TRAC reflood model in TRAC-PD2 with FLECHT and University of California (UC) Berkeley reflood tests. Initial data comparisons using the Semiscale S-06-3 input description indicate good agreement with experimental data. We had initial difficulties with the ORNL THTF input description because it used a velocity boundary condition at the top of the test section and pressure boundary condition at the bottom of the test section. We thus developed an improved input description that uses velocities at both locations. This model is in good agreement with test data.

a. UC Berkeley and FLECHT Reflood Tests

(R. K. Fujita and F. L. Addessio, Q-9)

The assessment effort of the improved TRAC reflood model[14] has been increased this past quarter. Additional UC Berkeley reflood tests[15] were analyzed along with two FLECHT Skewed Power[16] tests. The assessment of the TRAC reflood model will be progressing from the current analysis of reflooding of single tubes and small rod bundles to future calculations of complete reactor system test facilities, such as Semiscale and LOFT.

The UC Berkeley Reflood Tests consist of monitoring the quenching phenomena of a vertically oriented heated round tube cooled by the forced injection of subcooled liquid into the bottom of the tube. The test matrix, shown in Table I, was established to investigate the minimum and maximum range of experimental parameters given in Ref. 15. The test parameters of interest were the initial tube wall temperatures, inlet water velocity, and inlet water temperature.

The test conditions, shown in Table II, for the FLECHT Skewed Power[16] tests were chosen for this portion of the assessment effort to demonstrate the code's ability to predict the quench front propagation for low and high flooding rate cases in a rod bundle. The FLECHT Skewed Power tests are more recent tests that use a new rod bundle, better instrumentation, and a lower bundle housing mass than was used in the original FLECHT-SET tests.[17] These tests represent a more suitable assessment problem set for the TRAC code than the Berkeley reflood tests because most of the constitutive relations for the vessel component were derived from rod bundle data.

The results of the assessment calculations are shown in Figs. 7-12 and consist of wall temperature histories for specific axial locations along the test section. The calculations compare favorably with the data for nearly all the tests analyzed. The important reflooding phenomena such as quench front propagation, liquid entrainment, carryover fraction, and void fraction distribution have

TABLE I

EXPERIMENTAL TEST CONDITIONS FOR UC BERKELEY REFLOOD EXPERIMENTS

Run No.	V_{in} (cm/s)	T_{in} (K)	Q (kw)	T_w (K)
114	12.70	338	3.29	811
189	12.36	294	3.59	811
186	12.27	296	1.14	589
187	2.46	299	3.63	811

been adequately modeled by the TRAC code with the exception of the low flooding rate cases, UC-B Test 187, and FLECHT Test 15305.

TABLE II

EXPERIMENTAL TEST CONDITIONS OF FLECHT SKEWED POWER TESTS

	Test 17201	Test 15305
Upper Plenum Pressure, MPa	0.276	0.276
Flooding Rate, cm/s	15.2	2.20
Peak Rod Power, kW/m	2.297	2.297
Inlet Coolant Temperature, K	326.0	326.0
Initial Clad Temperature at Peak, K	1 161.0	1 146.0
Radial Power Profile	Uniform	Uniform
Power Decay	ANS + 20%	ANS + 20%

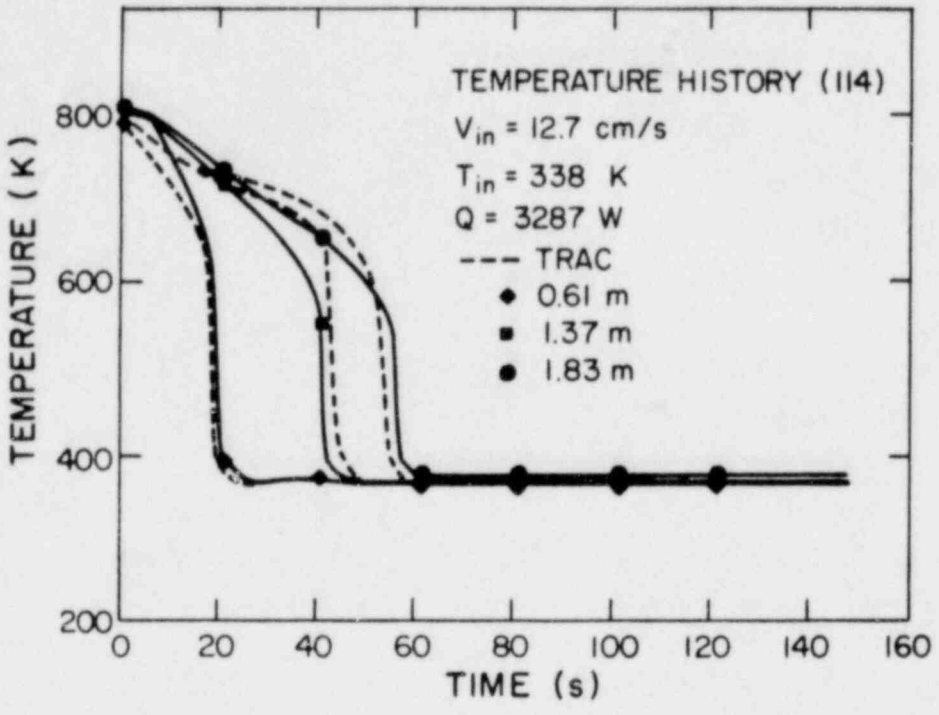

Fig. 7. Comparisons of wall temperature profiles for UC Berkeley test 114.

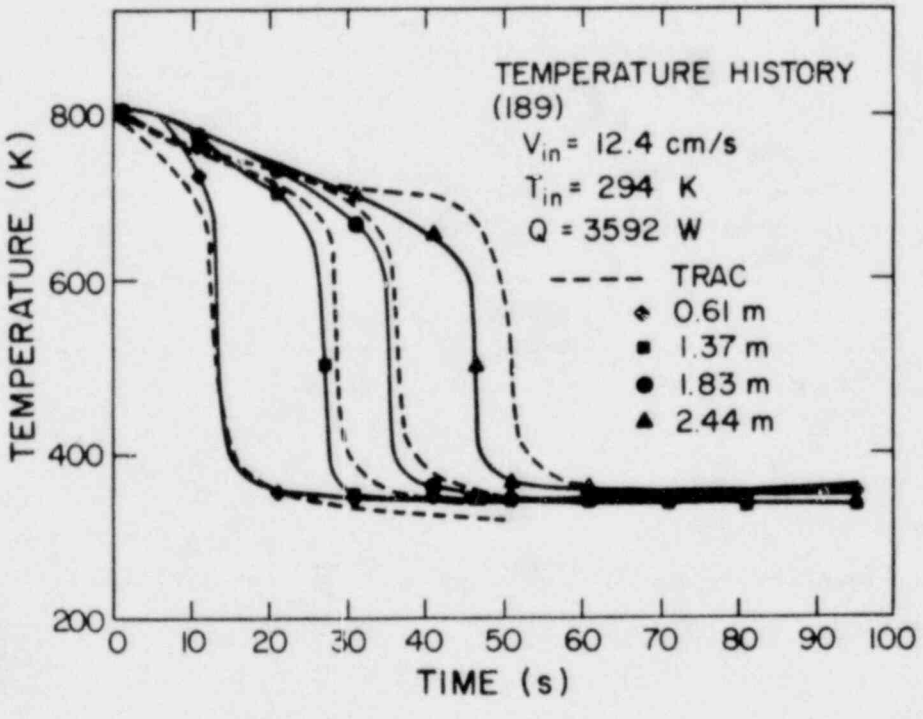

Fig. 8. Comparisons of wall temperature profiles for UC Berkeley test 189.

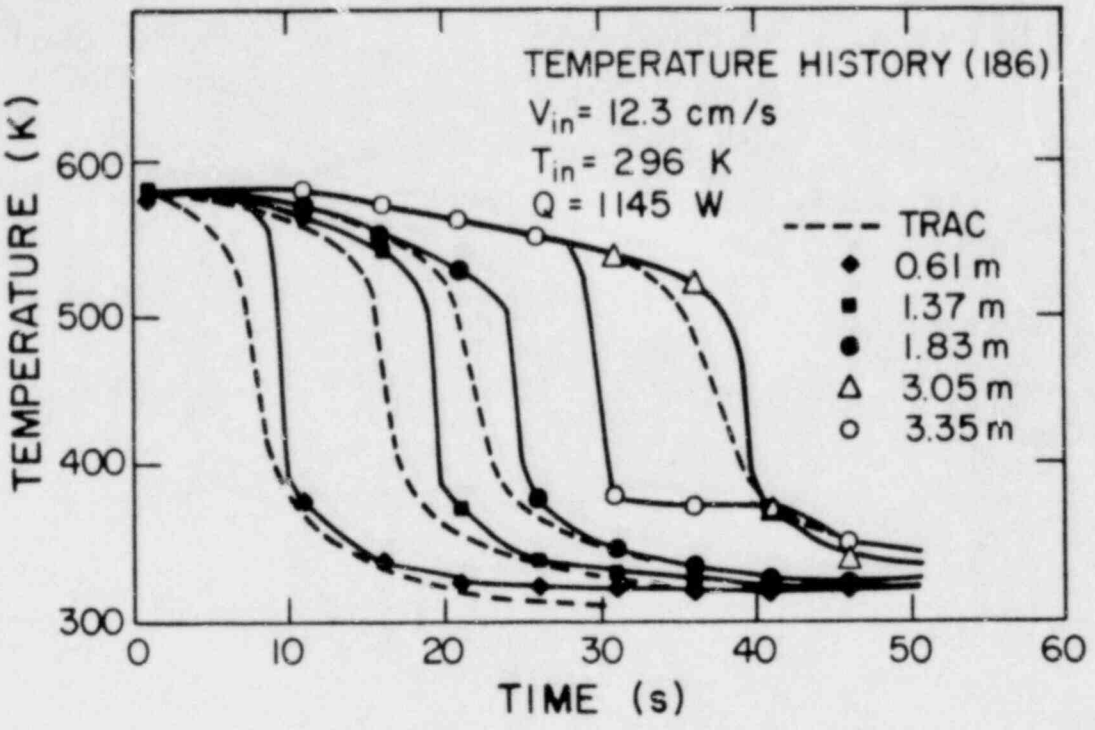

Fig. 9. Comparisons of wall temperature profiles for UC Berkeley test 186.

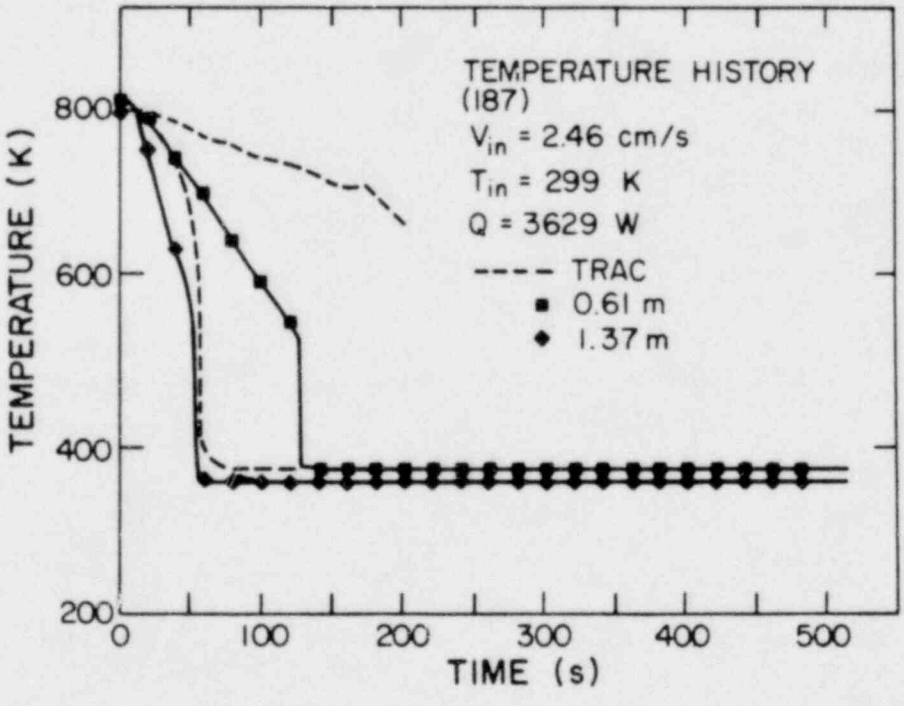

Fig. 10. Comparisons of wall temperature profiles for UC Berkeley test 187.

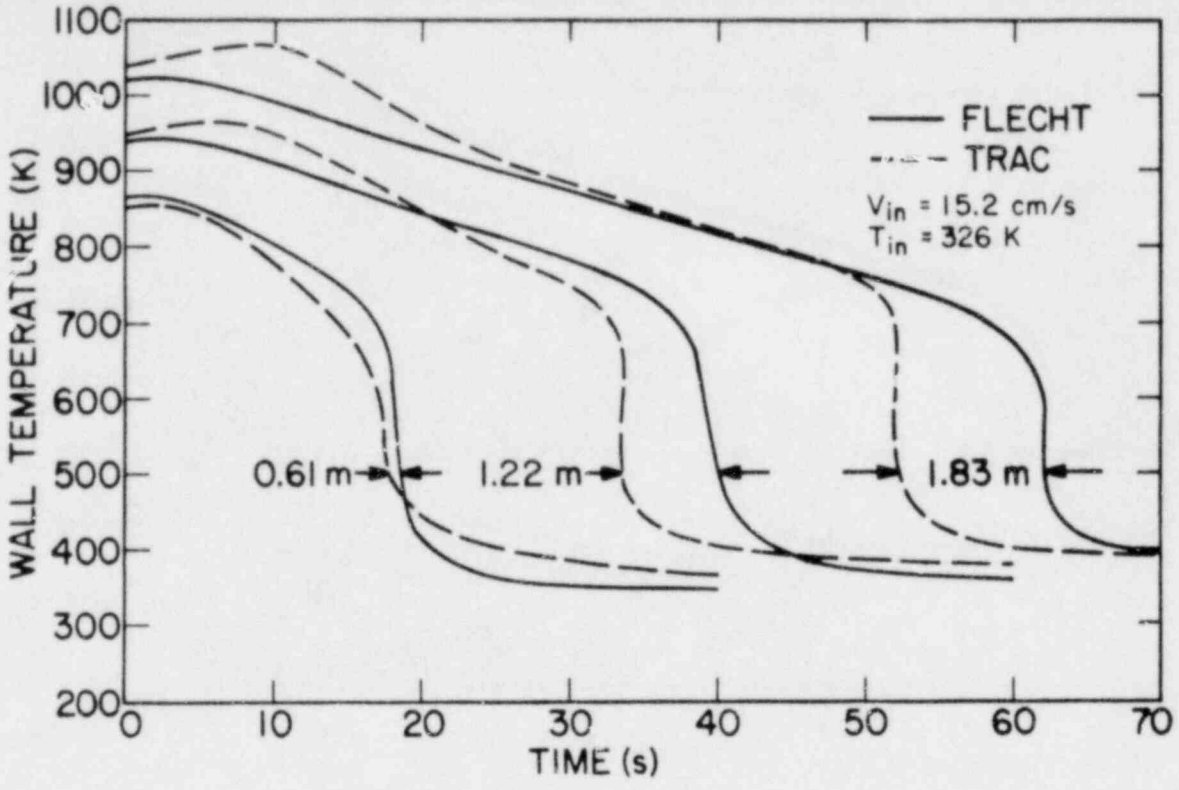

Fig. 11. Comparison of wall temperature profiles for FLECHT test 17201.

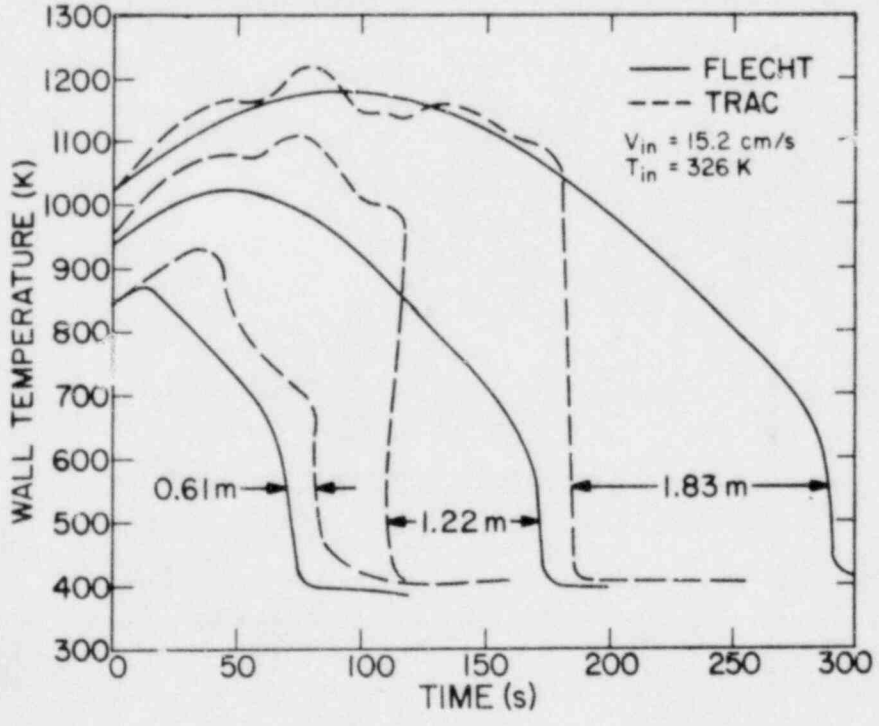

Fig. 12. Comparison of wall temperature profiles for FLECHT test 15305.

Top quenching occurred in most UC-B tests that initially had wall temperatures below 922 K.[15] This was due to a premature cooling of an unheated flange assembly located at the top of the test section. This upper tube precooling and quenching phenomena was evident in UC-B test 186 and is indicated (see Fig. 9) by the wall quenching at the 3.35-m elevation approximately 10 s before quenching at the 3.06-m level. Our models for these analyses did not consider test facility components other than the heated tube or rod bundle. Therefore, these predictions do not show the downward propagating quench front observed in these UC-B tests.

A comparison of the mass effluent from the test section for UC-B test 114 is presented in Fig. 13. A time lag of up to 30 s was detected and reported in Ref. 15 for the measured mass of liquid and steam flowing out of the test section for some test cases. This lag could account for the small discrepancy in the mass profiles observed in Fig. 13.

Figures 10 and 12 show the results for the two low flooding rate tests, UC-B test 187 and FLECHT test 15305, respectively. Dissimilar

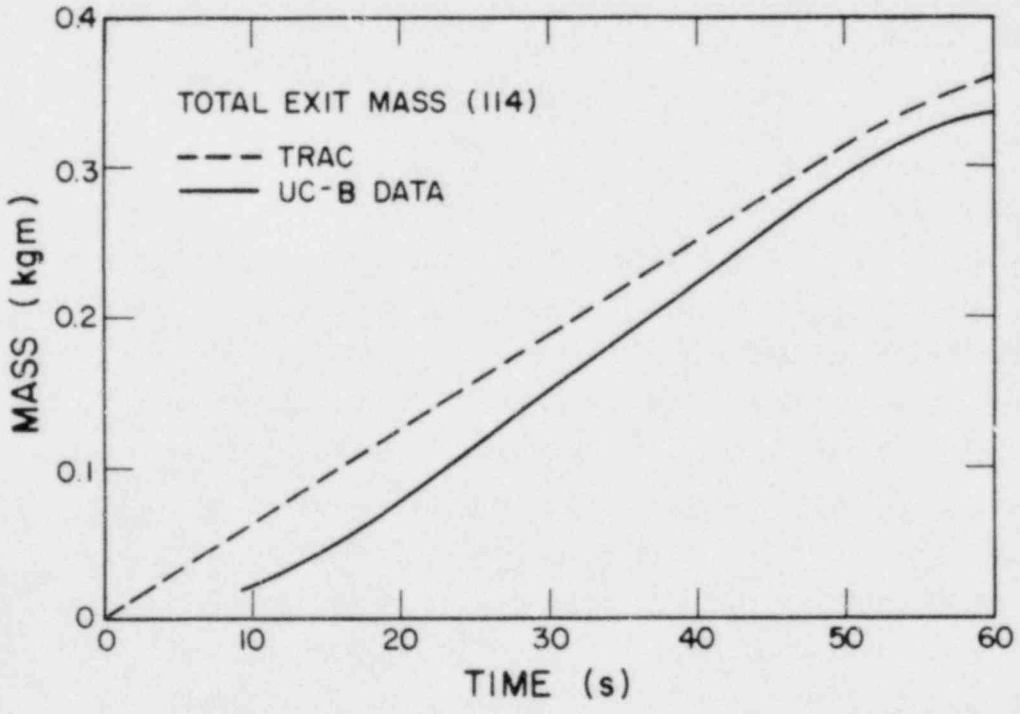

Fig. 13. Comparison of total mass effluent for UC Berkeley test 114.

quenching trends are noted for these two cases, one quenching very rapidly and the other very slowly. The FLECHT rod bundle quenched very early for all elevations above the 2-foot level. This was attributed to the calculated total steam-water carryover rate being much less than the measured carryover rate. As a consequence, the predicted quench front progressed at a rate approximately equal to the flooding rate and much faster than the measured quench front propagation.

A different phenomenon was predicted for the UC-B test 187. For this case, a significant amount of liquid was completely vaporized near the bottom of the test section resulting in a situation where very little liquid was entrained and large quantities of steam were ejected out of the test section. Consequently, the liquid level moved very slowly and precooling of the upper tube elevations was minimal because only steam flowed ahead of the quench front.

In general, these comparisons show that the TRAC reflood model gives good predictions for the high flooding rate cases with low or high initial wall temperatures and inlet fluid temperatures. The models to predict the liquid entrainment and total carryover rates must be improved to obtain better results for the low flooding rate tests.

b. Semiscale S-06-3

(J. K. Meier, Q-9)

An input description of Semiscale Test S-06-3 has been created and a calculation made for 30 s after pipe rupture. To minimize computing time, the vessel noding model was reduced to two theta segments as opposed to the four theta segments used in the Standard Problem 5 (S-02-8) model.

Reasonably accurate results for cladding temperatures and mass flow rate were obtained with the S-06-3 model. However, starting at 10 s after the rupture, the calculated system pressure tended to fall below experimental results. In the problem S-02-8, this same type of deviation was attributed to an underprediction of upper head superheating. Final analyses of problem S-06-3 is awaiting completion of TRAC-PD2 and will be included as part of the prerelease assessment effort.

c. ORNL THTF Experiments

(J. S. Gilbert, Q-9)

A TRAC input description of the ORNL THTF[18-20] test 177 has been developed as a part of the effort to assess the minimum film boiling correlation used by TRAC.

An isometric drawing of THTF is shown in Fig. 14. Figure 15 shows a simplified schematic of this same facility. The core in the test section is composed of a 7 x 7 array of electrically heated rods. In this test, 4 of the 49 rods were not powered. Each of the powered rods is 0.011 22 m in diameter, 3.66 m in length, and has a power input of 82 kW.

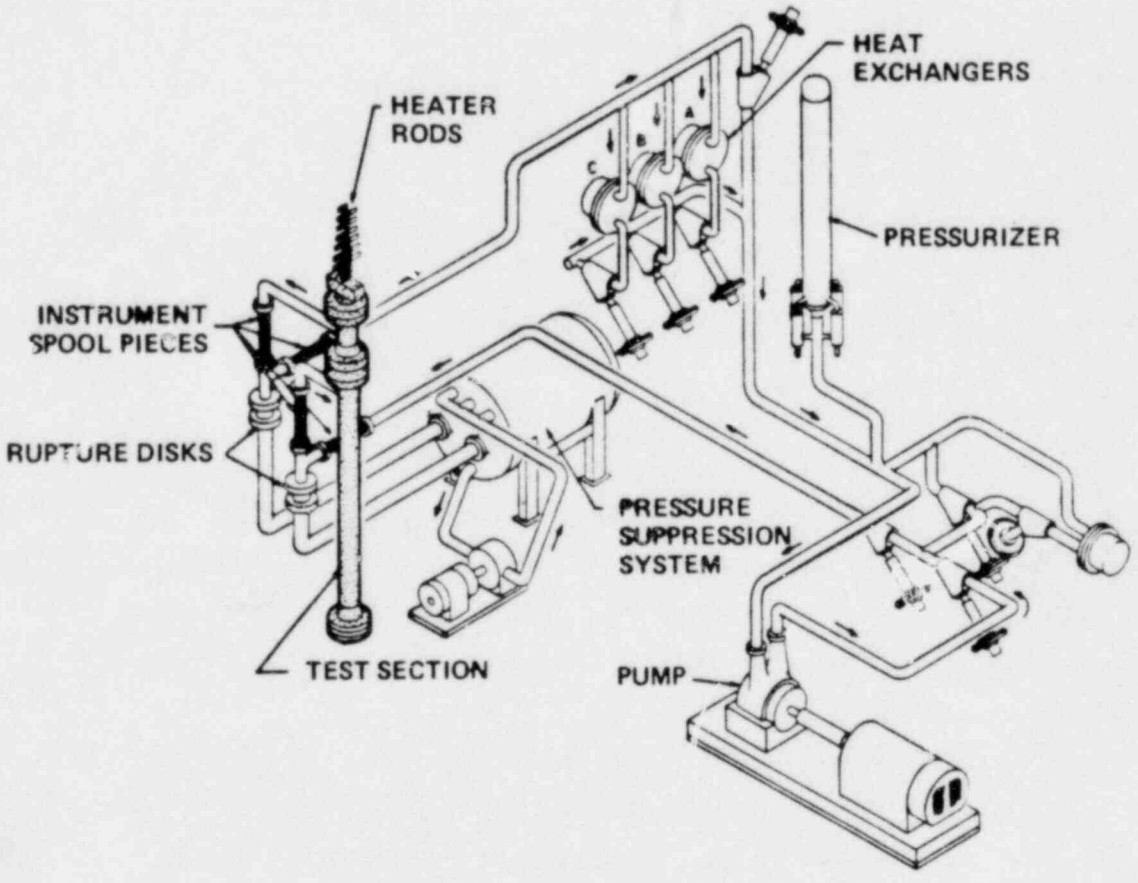

Fig. 14. ORNL thermal-hydraulic test facility.

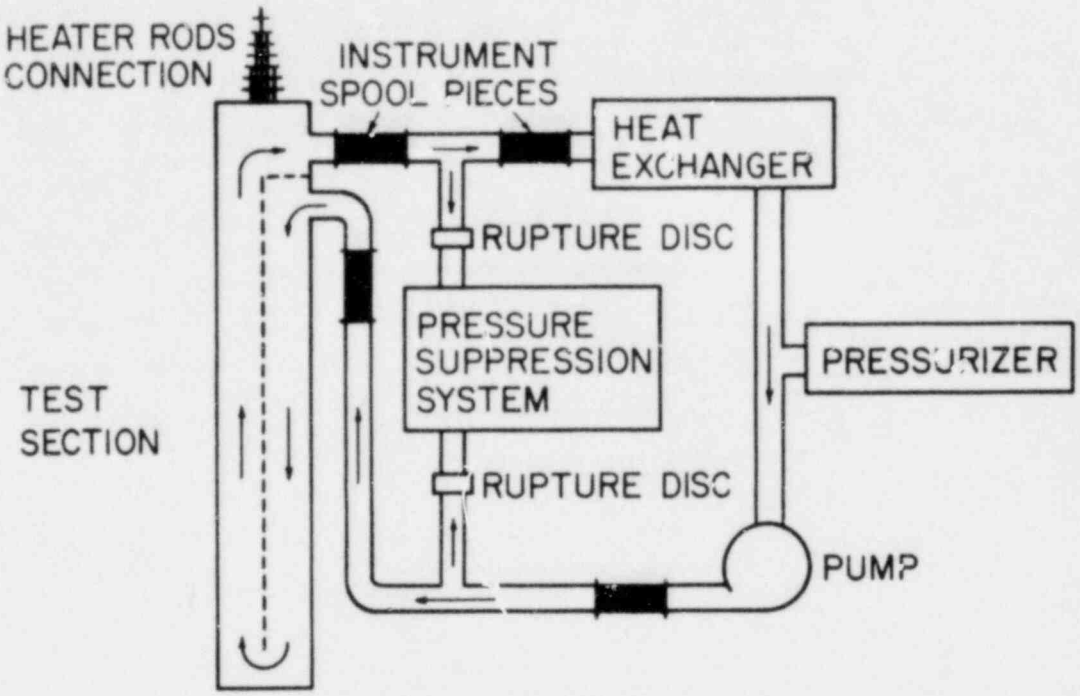

Fig. 15. ORNL thermal-hydraulic test facility schematic.

During steady-state operation, water is pumped through the system at a nominal rate of 23 kg/s and at an inlet pressure of 16 MPa. The coolant inlet and outlet temperatures are 550 and 581 K, respectively. The transient is initiated by the simultaneous opening of inlet and outlet blowdown rupture disks.

In the TRAC input description (see Fig. 16) only the test section and piping containing instrumentation immediately adjacent to the test section are modeled. A 32-volume one-dimensional vessel model was used with pipe components located at its inlet and outlet. Boundary conditions for the pipe components based on test data completed the input description of the facility.

For the steady-state calculation by TRAC, the power input to the rods was set to the experimental value and the inlet mass flow rate was adjusted so that the inlet and outlet temperatures of the coolant matched experimental values. This resulted in a mass flow rate 7% higher than the test data indicated. The calculated steady-state rod

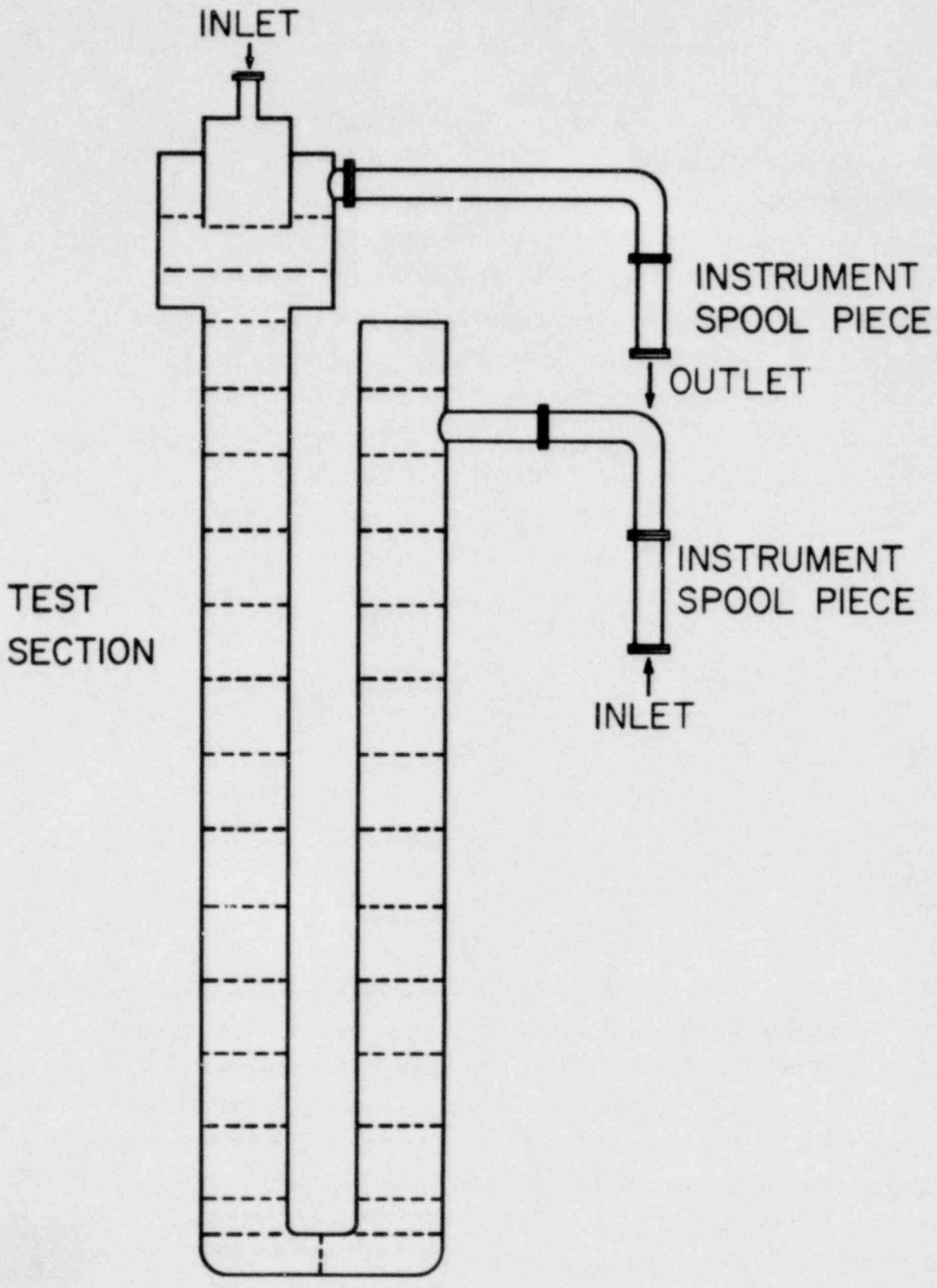

Fig. 16. Single-channel test section vessel model.

surface temperatures were generally a few degrees higher than the test data with a minimum difference of 1 K occurring at the midplane of the core.

The first 4 s of system transient behavior were analyzed using two different sets of boundary conditions. The first set (case 1) used an experimental pressure condition at the inlet and an experimental velocity condition at both the inlet and the outlet.

When the results of case 1 were compared to the test data the mass flow rate out the top of the test section (see Fig. 17) reasonably matched the test data, but the mass flow rate out the bottom of the test section was approximately twice the test data. For case 2, the calculated mass flow rate at the outlet of the test section was in better agreement than were the results from case 1 and the calculated mass flow rate at the bottom of the test section was in very good agreement with experimental data. The system pressure, as calculated by case 2 (see Fig. 18), was in good agreement. Cladding temperature comparisons are now being made. Based on our experience, these comparisons will be made with case 2 boundary conditions.

B. TRAC Applications

(J. C. Vigil and J. R. Ireland, Q-6)

The work described in this section includes the application of TRAC to full-scale LWR transients and to the planned large-scale German and Japanese 2D/3D experiments. TRAC is being used to analyze a variety of other tests and problems for NRC and for outside users.

Further parametric calculations were performed to investigate variations of the TMI-2 accident scenario. These calculations, which are described in detail below, investigate the effects of primary coolant pump heat addition on the time-to-core recovery and the consequences of tripping the coolant pumps at the beginning of the accident.

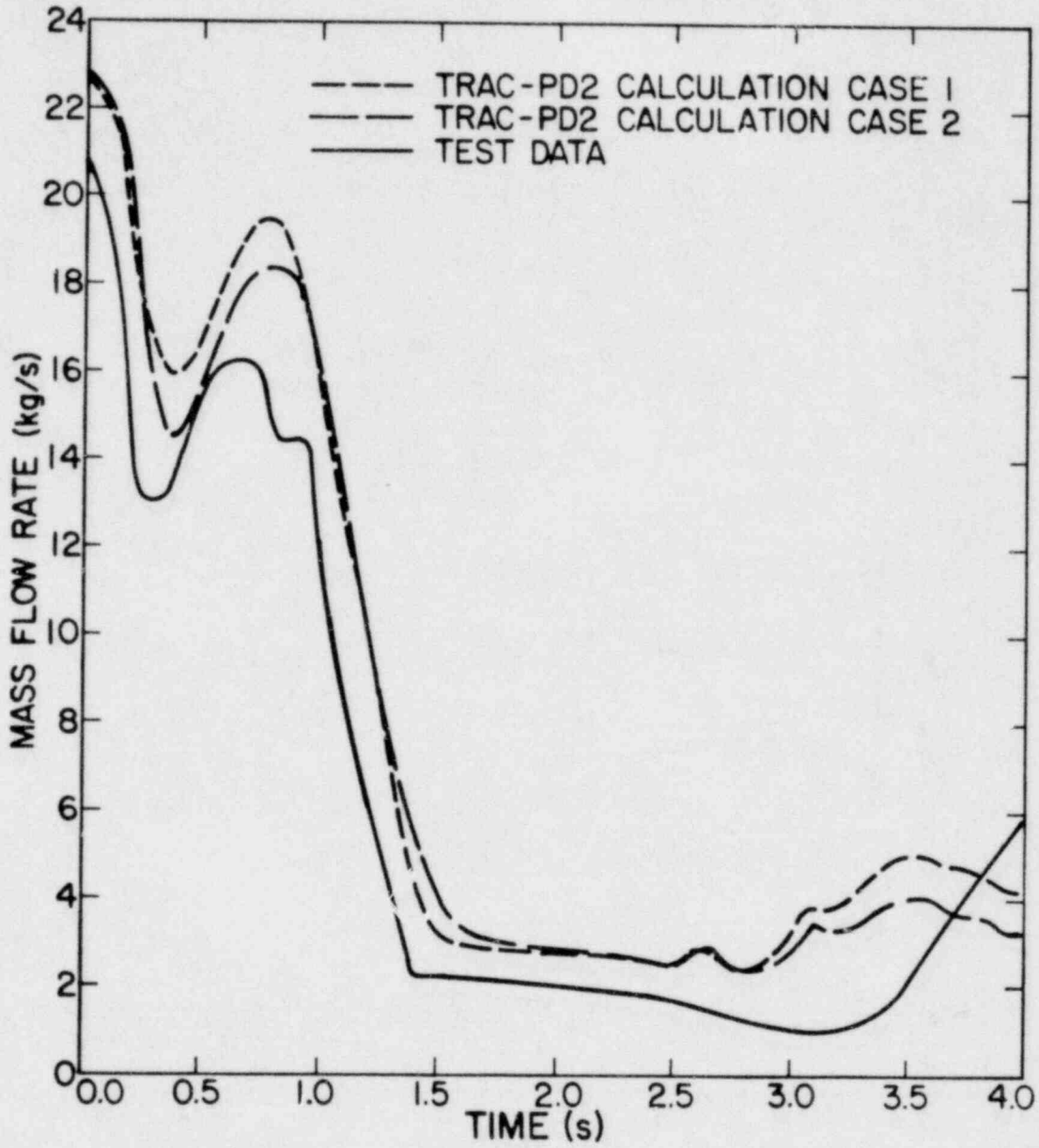

Fig. 17. A comparison of TRAC-PD2 results with the experimental outlet mass flow rate from the vessel.

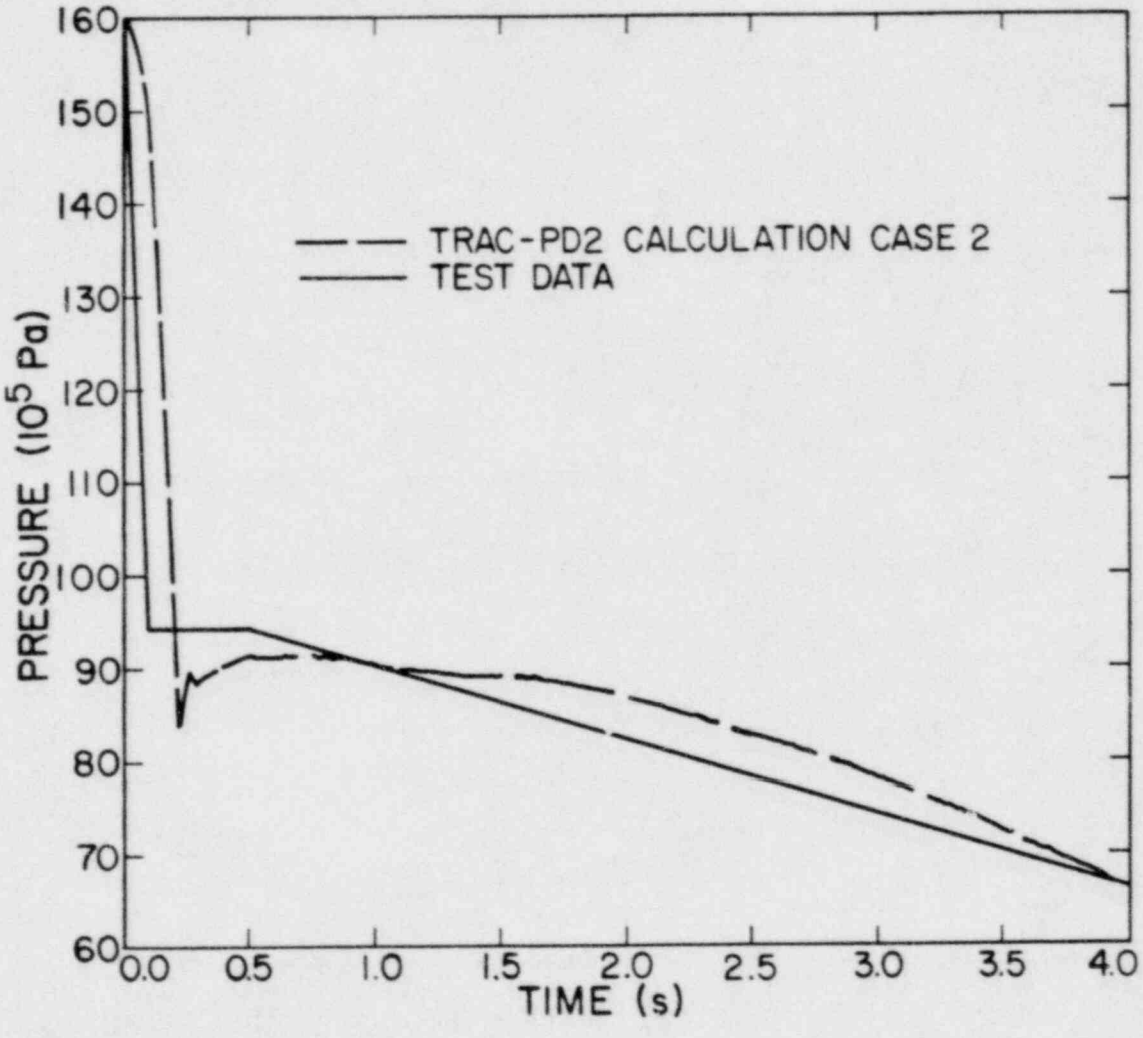

Fig. 18. A comparison of TRAC-PD2 results with the experimental inlet pressure to the vessel.

Several modifications were made to the German PWR reference reactor model based on additional information received from the Germans. The TRAC input model also was modified to obtain the correct pressure drops within the pressure vessel for the initial steady-state condition. Transient calculations using the modified model are in progress.

A posttest calculation of Cylindrical Core Test Facility (CCTF) test C1-1, using a modified entrainment model, the latest TRAC code version, and corrected input errors yielded improved results over previous calculations. Efforts are continuing to improve even further the code results to allow pretest predictions of other tests in CCTF. Parametric calculations requested by the Japanese for the Slab Core Test Facility (SCTF) were completed at the end of the quarter and will be reported in detail next quarter.

TMI Sensitivity Calculations -- The Effects of Pump Heat Addition and Early Primary Pump Trip

(J. R. Ireland, Q-6)

In response to a request from NRC, several parametric calculations were performed on the TMI base-case calculation reported in the previous quarterly report.[14] The purpose of these calculations was to determine the effects of pump heat addition on the time-to-core uncovery for the base case (since the pump heat was not modeled in the original base-case calculation) and to determine the consequences of tripping the primary coolant pumps at reactor scram (which eliminates the pump heat source) rather than as in the actual TMI accident. This latter calculation is referred to as Case D2 by the NRC.[21]

The results of four TRAC calculations will be reported.

- Base-case calculation (as reported in Ref. 22) -- No pump heat sources
- Base-case calculation with pump heat addition
- Primary pumps tripped at transient initiation (Case D2):

  Free-spinning pump rotors - effective pump resistance: K ~ 1.6

  Semilocked pump rotors - effective pump resistance: K ~ 10.0.

For all of the above calculations, the same initial and boundary conditions were used as those reported in Ref. 22. Also, all calculations were carried out to about 2 000 s, which appeared to be sufficient to make detailed thermal-hydraulic comparisons and to see general trends.

The important conclusions that can be drawn from these analyses are

1. For a TMI-2-type transient, the effects of adding the pump heat to the primary system fluid are negligible, and the time-to-core uncovery remains about the same as in the base-case calculation.

2. Tripping the primary system pumps at transient initiation results in earlier phase separation and core voiding; thus core uncovery will occur sooner than in the pump heat addition case. The time-to-core uncovery is strongly coupled to the pump resistance for these cases.

From these calculations the benefits obtained by leaving the pumps on (i.e., forced convection cooling capability) far outweigh the benefits of having the pumps off (i.e., no additional heat source to the fluid) for a TMI-2-type transient.

a. Base-Case Calculation with Pump Heat Addition

This calculation was identical to the base case except that a volumetric heat source was included in the pump energy equation to model the pump power that is dissipated to the fluid. Briefly, the model used degrades the steady-state pump power according to the pump head decay curve.

Graphical plots of key system parameters for the base case and the base case with pump heat addition can be found in Figs. 19-30. Figures 19 and 20 show that the upper head voids 300 s earlier in the pump heat source case when compared to the base case. This is due to the additional heat input by the pumps that causes earlier saturation conditions. Figures 21 and 22 show that the maximum hot-rod temperatures are slightly higher for the pump heat source case at about 500 s (592 K compared to 587 K). This is due to a higher

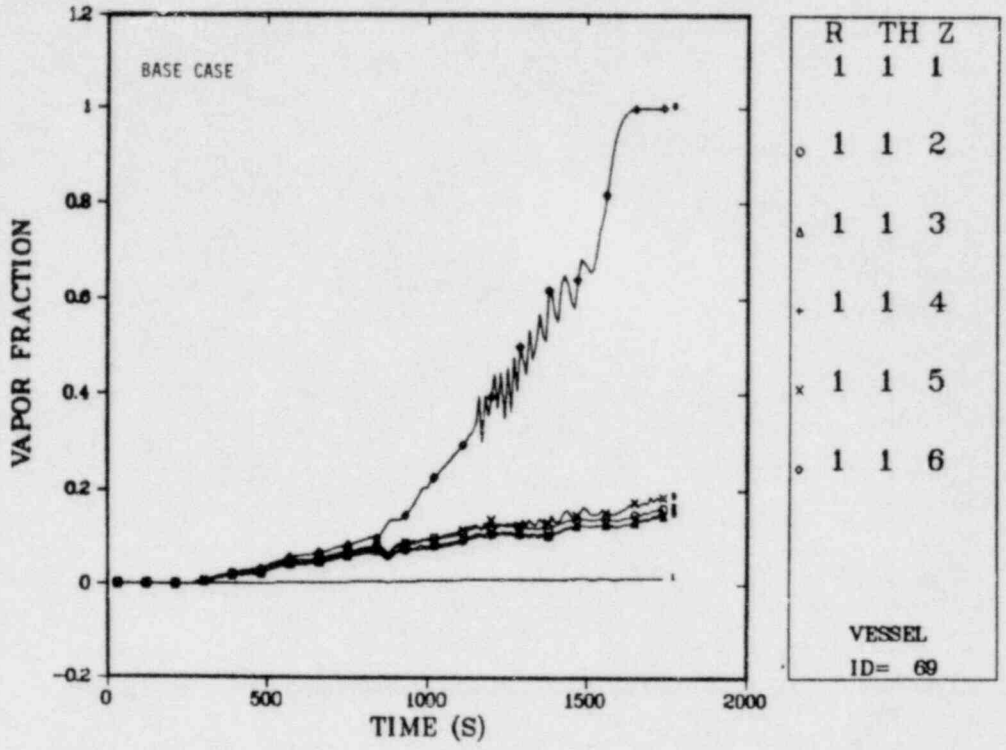

Fig. 19. TMI-2 vessel axial void fraction profile for base case.

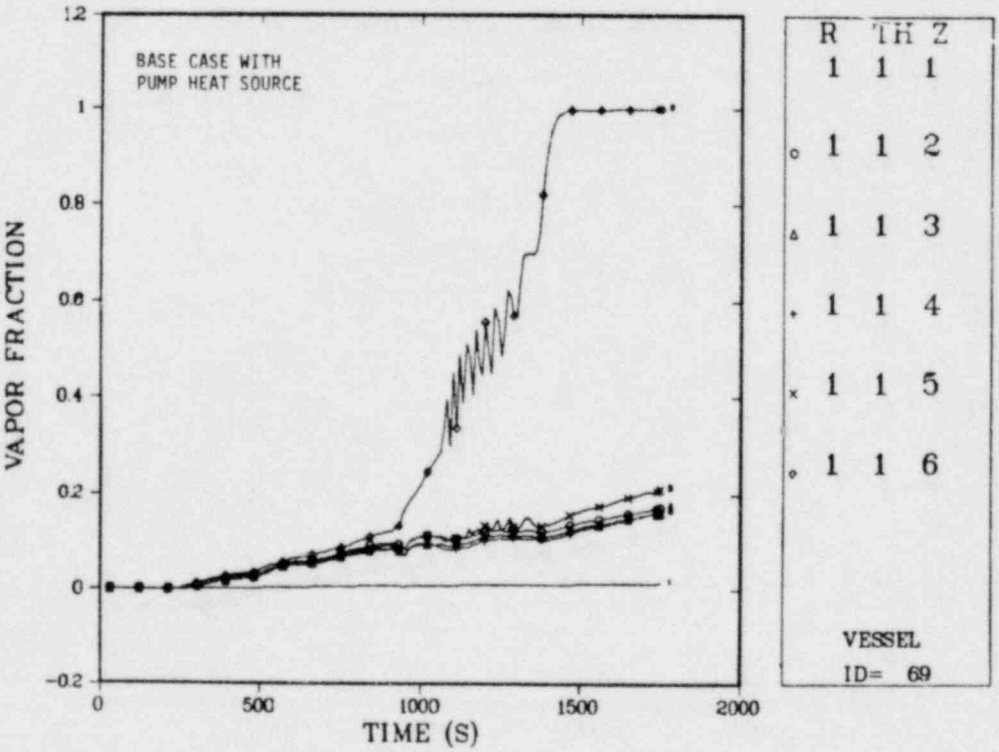

Fig. 20. TMI-2 vessel axial void fraction profile for base case with pump heat source.

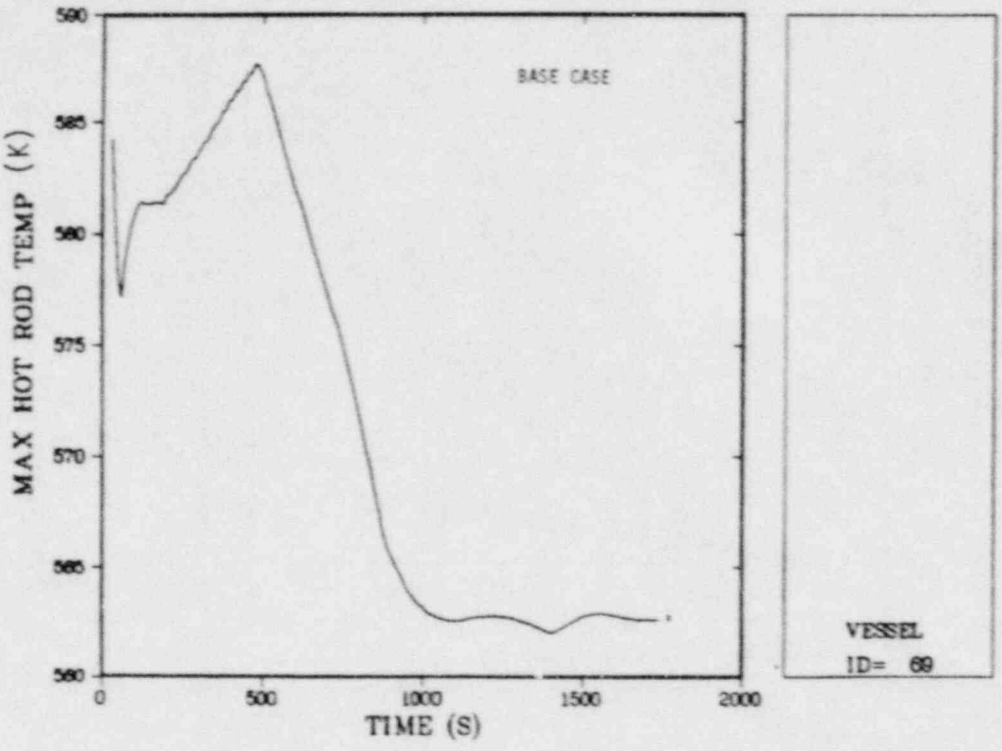

Fig. 21. TMI-2 hot-rod temperature history for base case.

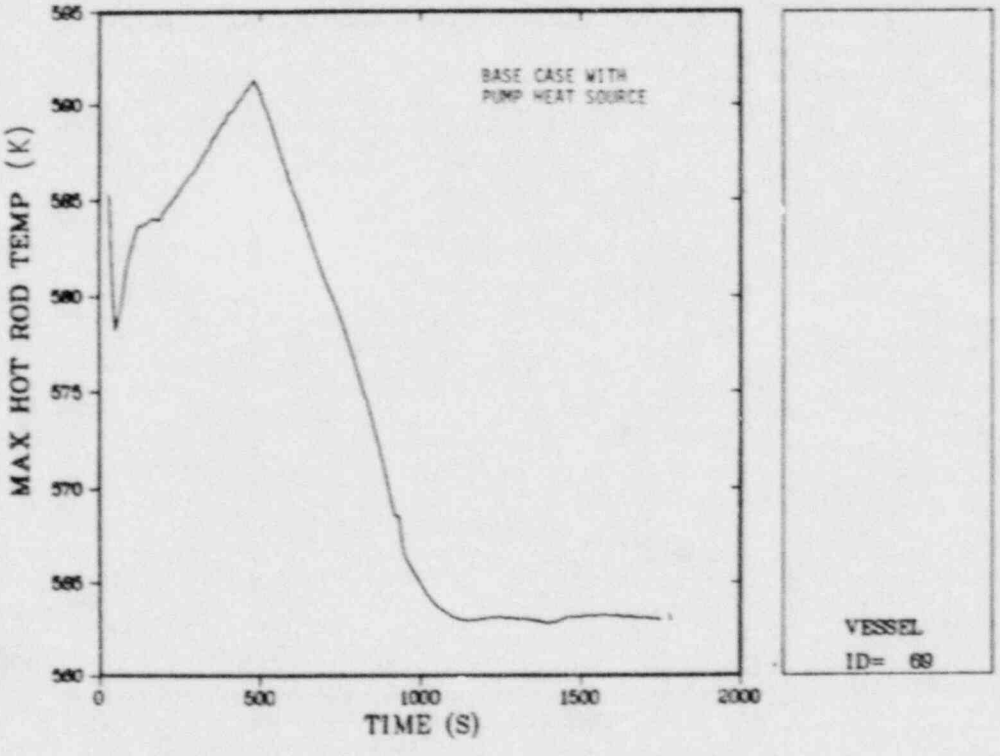

Fig. 22. TMI-2 hot-rod temperature history for base case with pump heat source.

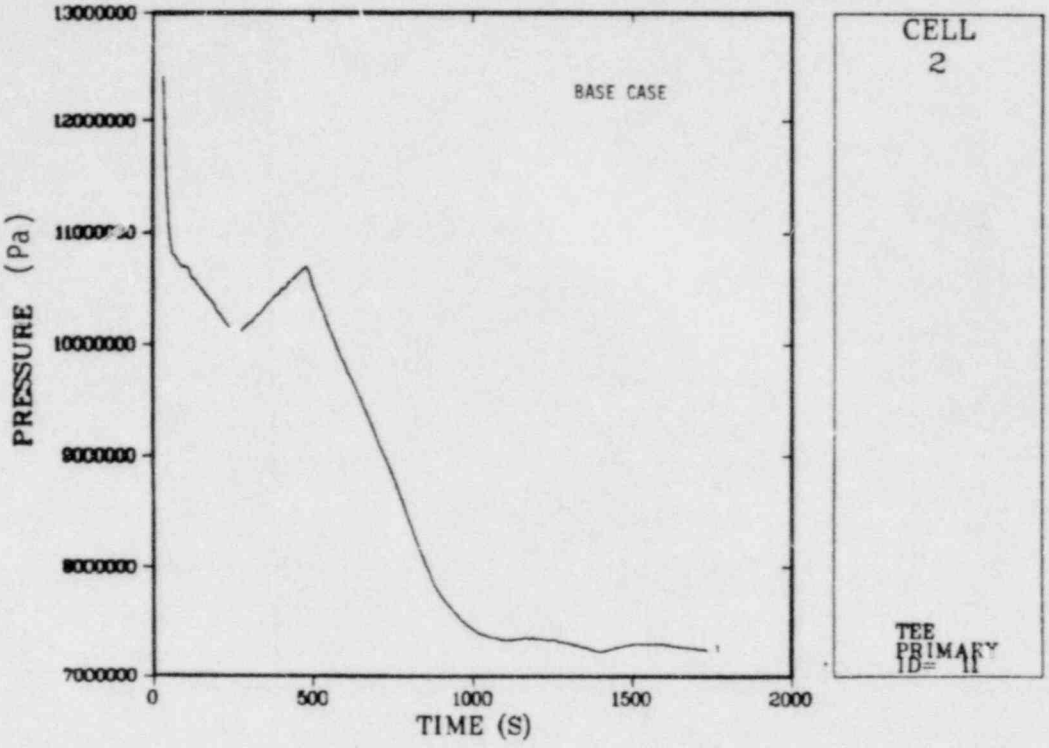

Fig. 23. TMI-2 system pressure for base case.

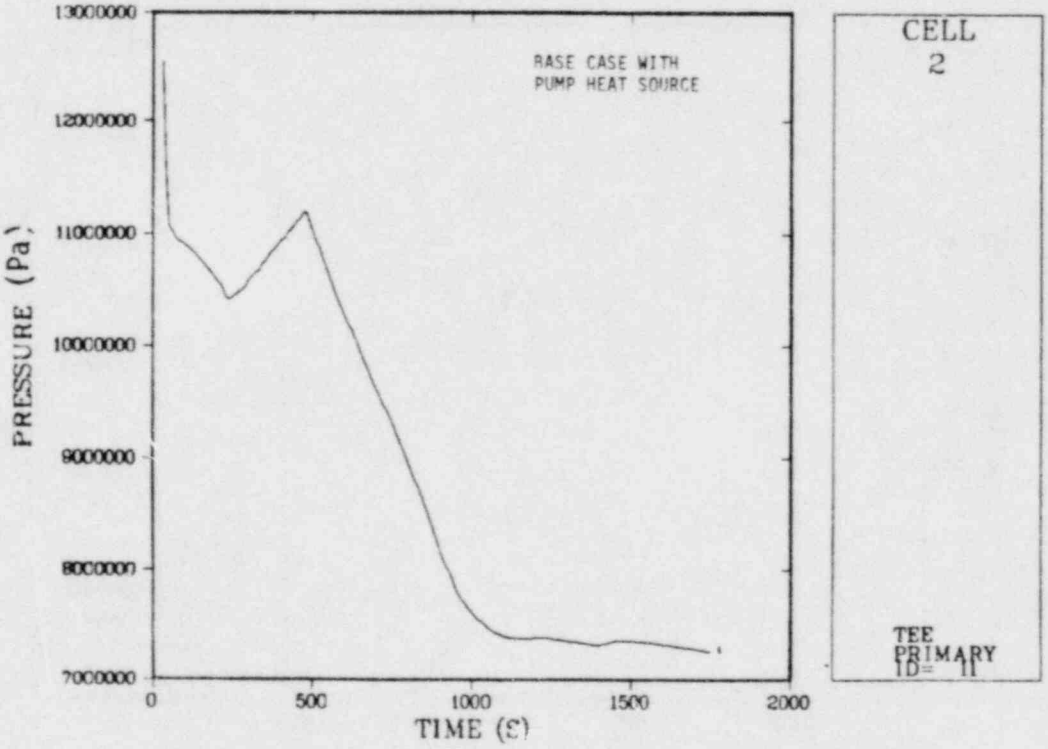

Fig. 24. TMI-2 system pressure for base case with pump heat source.

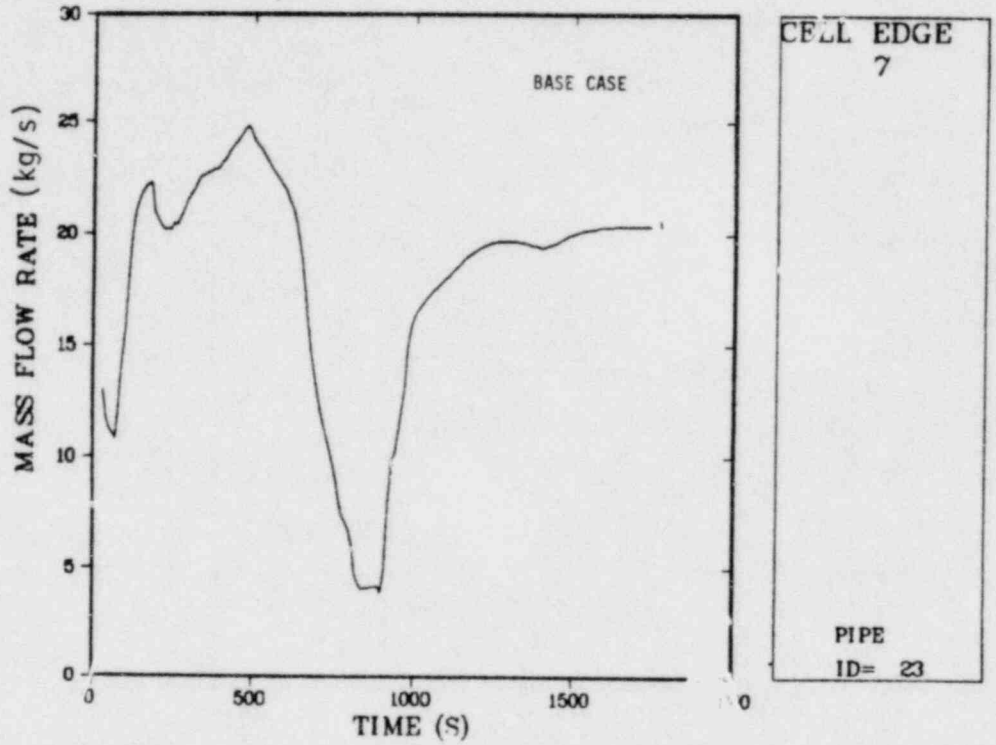

Fig. 25. TMI-2 PORV flow rate for base case.

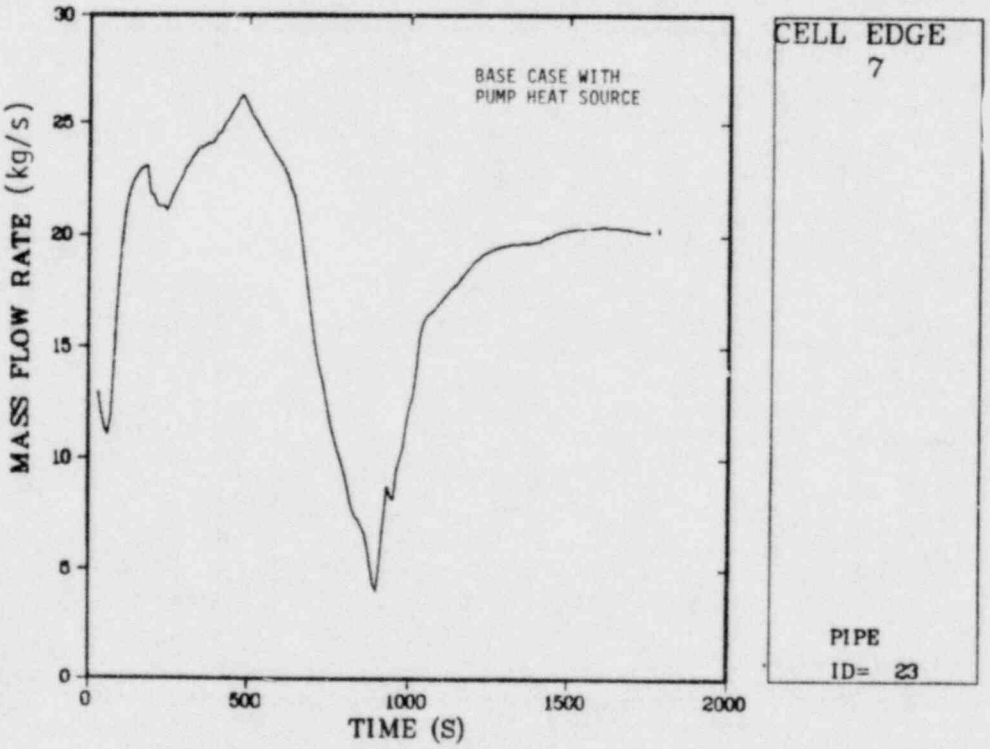

Fig. 26. TMI-2 PORV flow rate for base case with pump heat source.

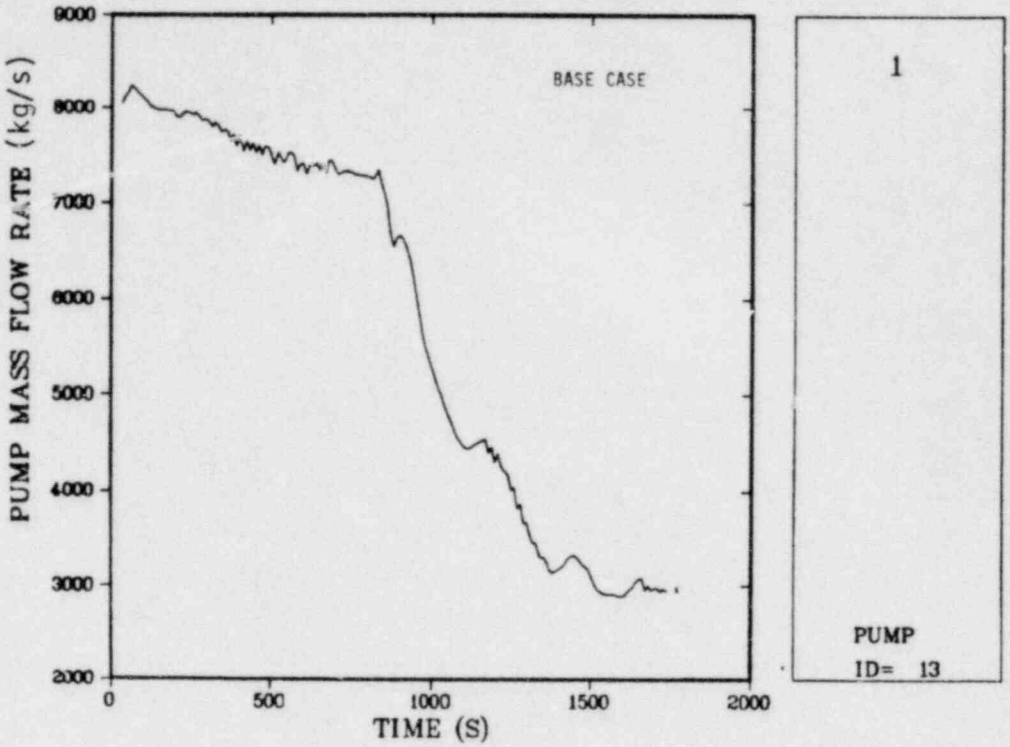

Fig. 27. TMI-2 Loop A pump mass flow rate for base case.

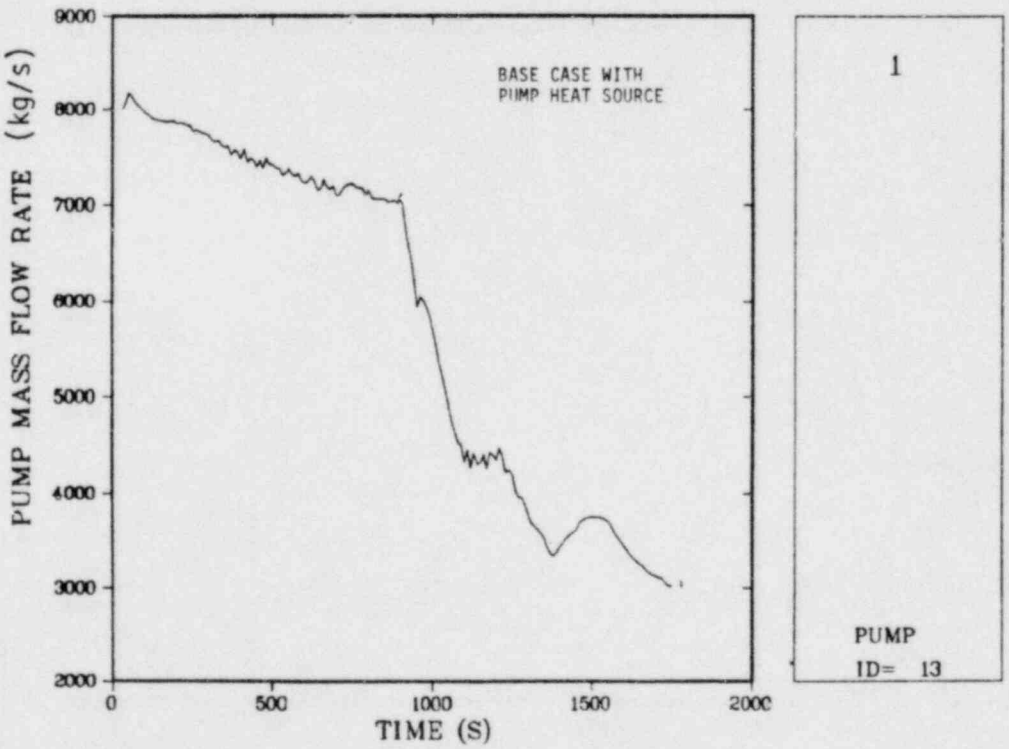

Fig. 28. TMI-2 Loop A pump mass flow rate for base case with pump heat source.

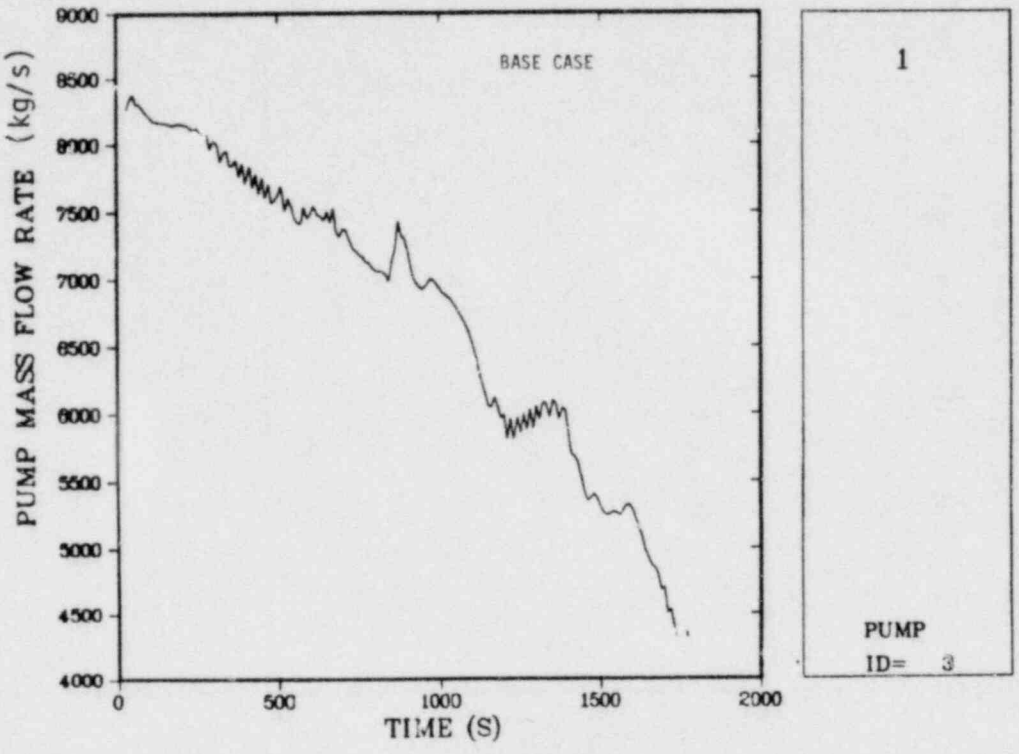

Fig. 29. TMI-2 Loop B pump mass flow rate for base case.

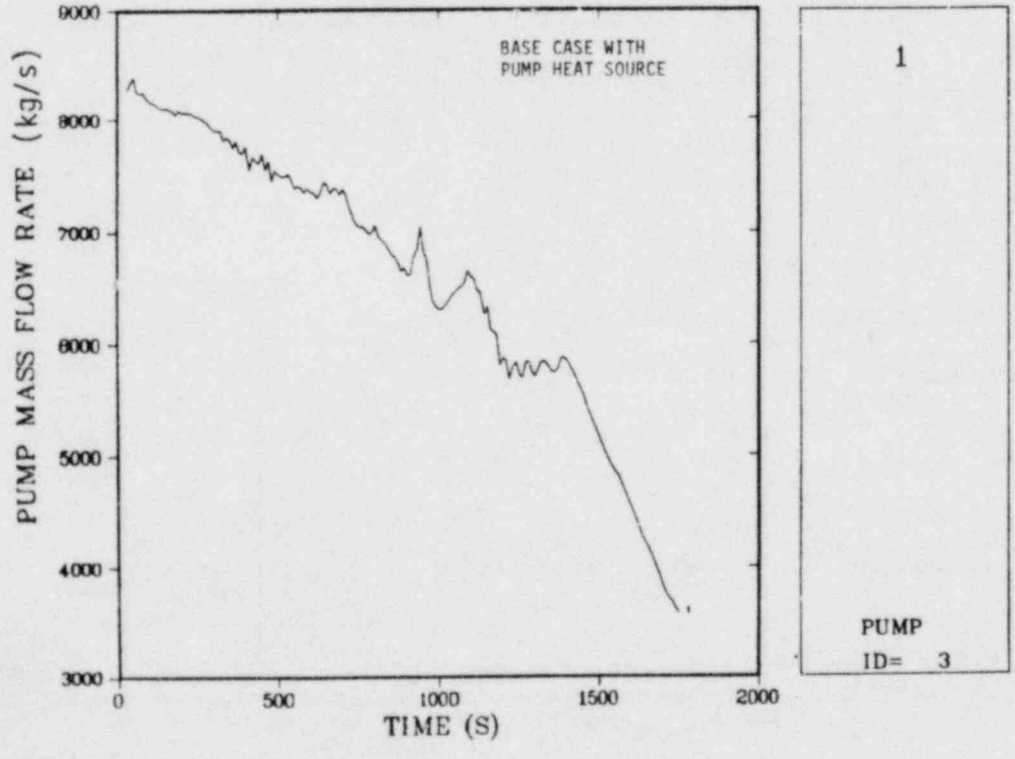

Fig. 30. TMI-2 Loop B pump mass flow rate for base case with pump heat source.

system pressure initially (Figs. 23 and 24), again caused by the additional pump heat input. However, when auxiliary feedwater flow is established after 500 s, the rod temperatures are about the same because the system pressure and saturation temperature essentially follow the steam generator back pressure.

The initial higher system pressure before auxiliary feedwater flow is established causes a slightly higher PORV flow (Figs. 25 and 26) for the pump heat source case; but again, after auxiliary feedwater flow is established, the PORV flows become about the same (~ 20 kg/s). The pressurizer water levels also are similar for both cases. Other key parameters [e.g., pump head, pump flow (Figs. 27-30), and loop temperatures] are also in good agreement with each other. In comparing the system water inventories for the two cases, after 2 000 s there is also not much difference (208 194 kg for the base case compared to 205 221 kg for the pump heat source case). The difference in inventories is due to the slightly higher initial PORV flow for the pump heat source case.

Thus, other than an initial higher system pressure and PORV flow and a slightly earlier time to upper head voiding, there is no significant difference between the base case and the base case with pump heat addition. For the pump model used in this calculation, the end result is that the time-to-core uncovery will not change by more than about 5 or 10 min.

b. Case D2 -- Free-Spinning Pump Rotor Resistance K ~ 1.6

This calculation assumes the primary coolant pumps are tripped at the time of reactor scram at TMI-2 (about 10.5 s). The pump resistance used for this case is the TRAC-calculated resistance typical of a free-spinning pump rotor. The TRAC pump model used for the TMI calculations was the Semiscale pump scaled up using the TMI pump-rated conditions.

Key system parameter plots for the free-spinning pump case are found in Figs. 31-38. Figures 20 and 31 show that the upper head voids at 1 500 s compared to 1 400 s (pump heat source case). Because the pumps are tripped at the beginning of the transient, there is no pump

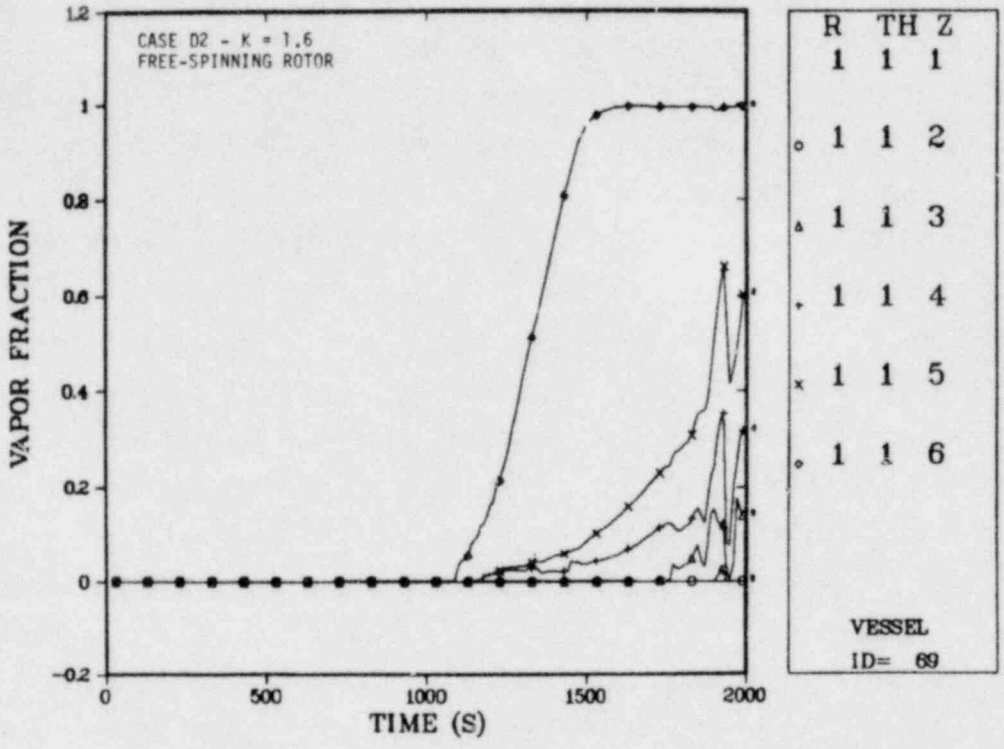

Fig. 31. TMI-2 vessel axial void fraction profile for case D2 with free-spinning rotor.

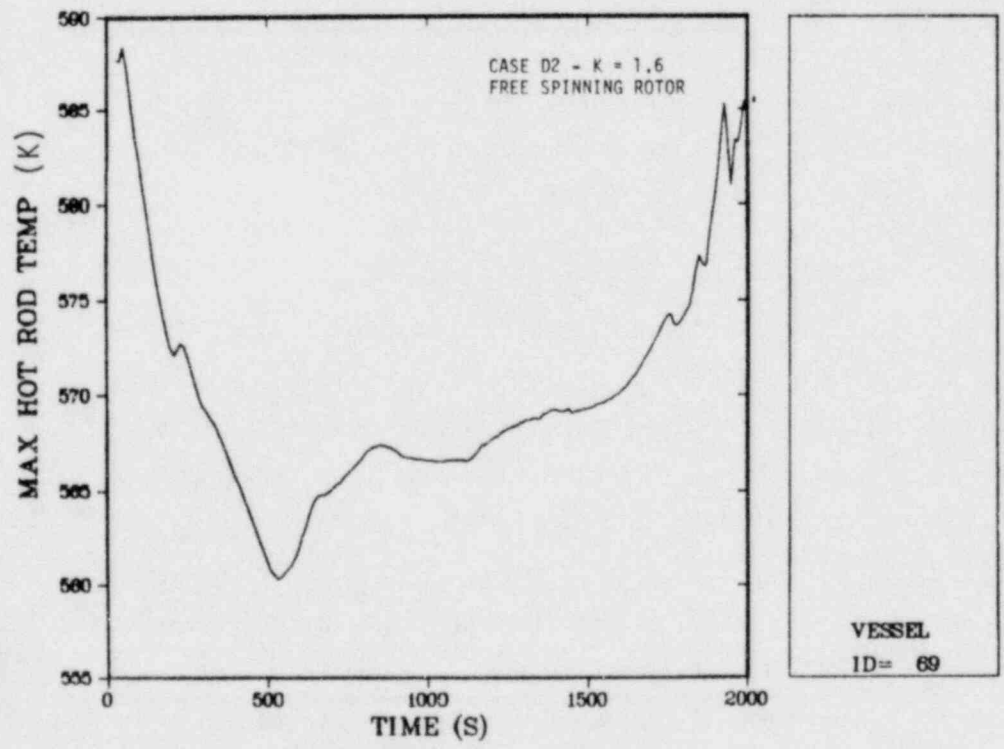

Fig. 32. TMI-2 hot-rod temperature history for case D2 with free-spinning rotor.

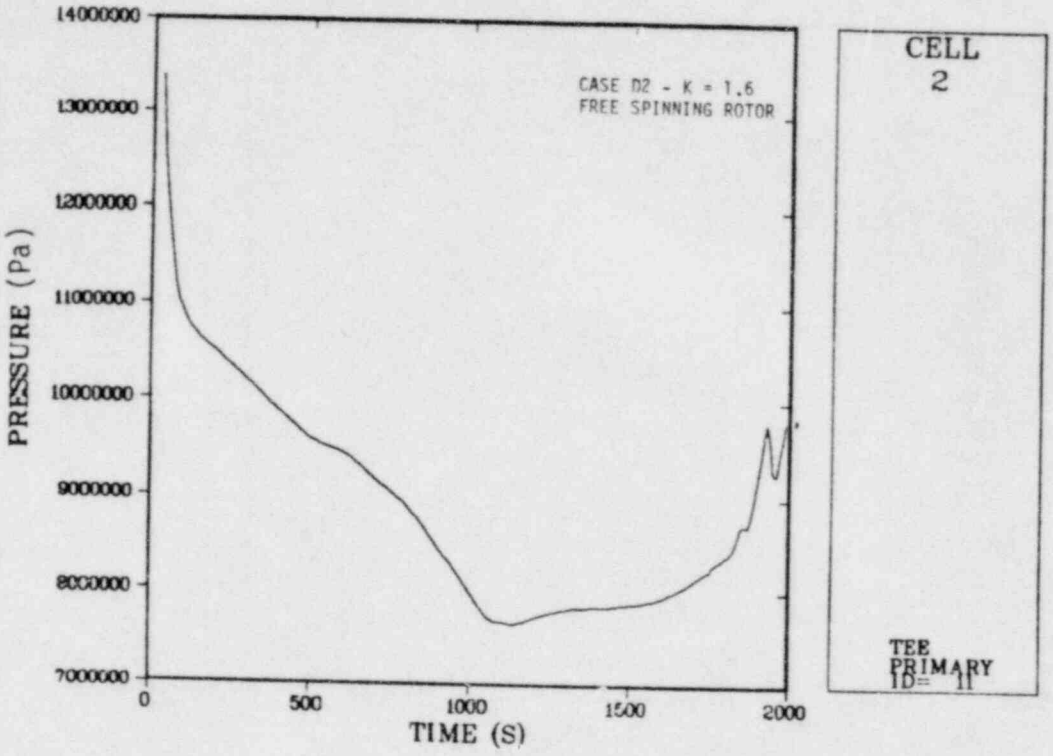

Fig. 33. TMI-2 system pressure for case D2 with free-spinning rotor.

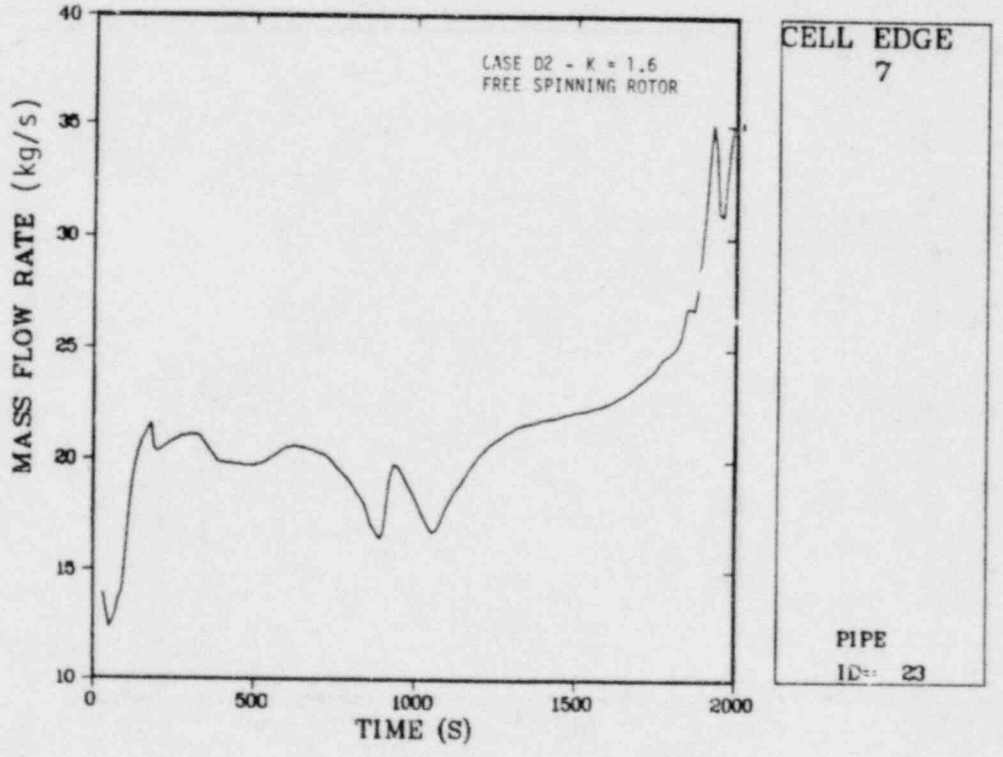

Fig. 34. TMI-2 PORV flow rate for case D2 with free-spinning rotor.

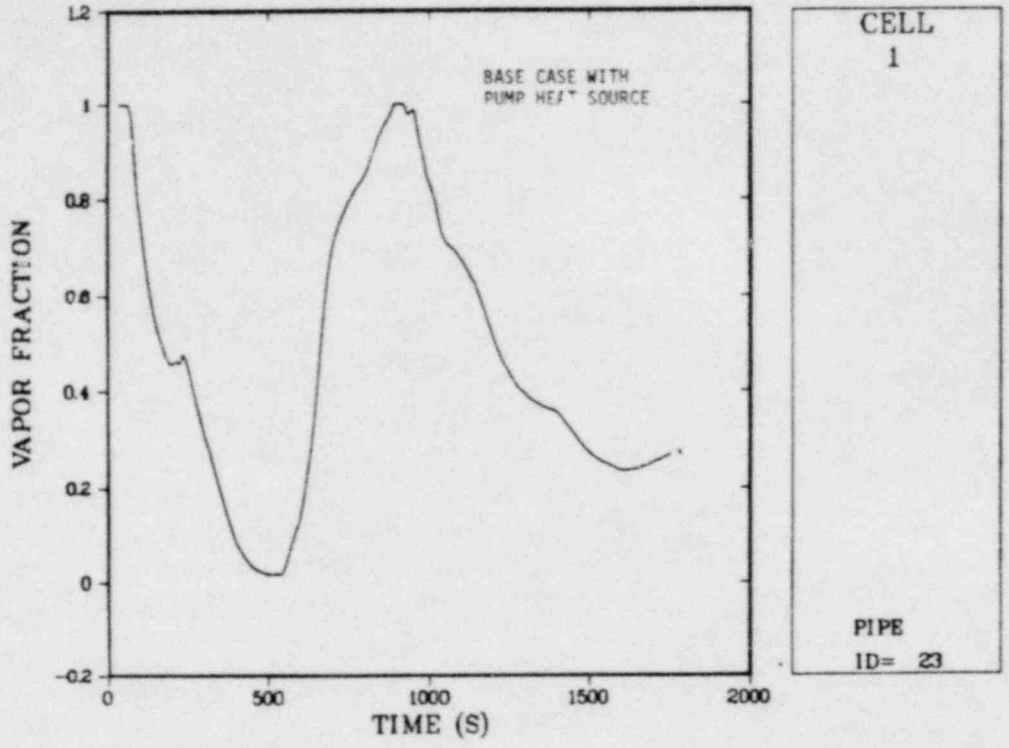

Fig. 35. TMI-2 pressurizer void fraction (top cell) for base case with pump heat source.

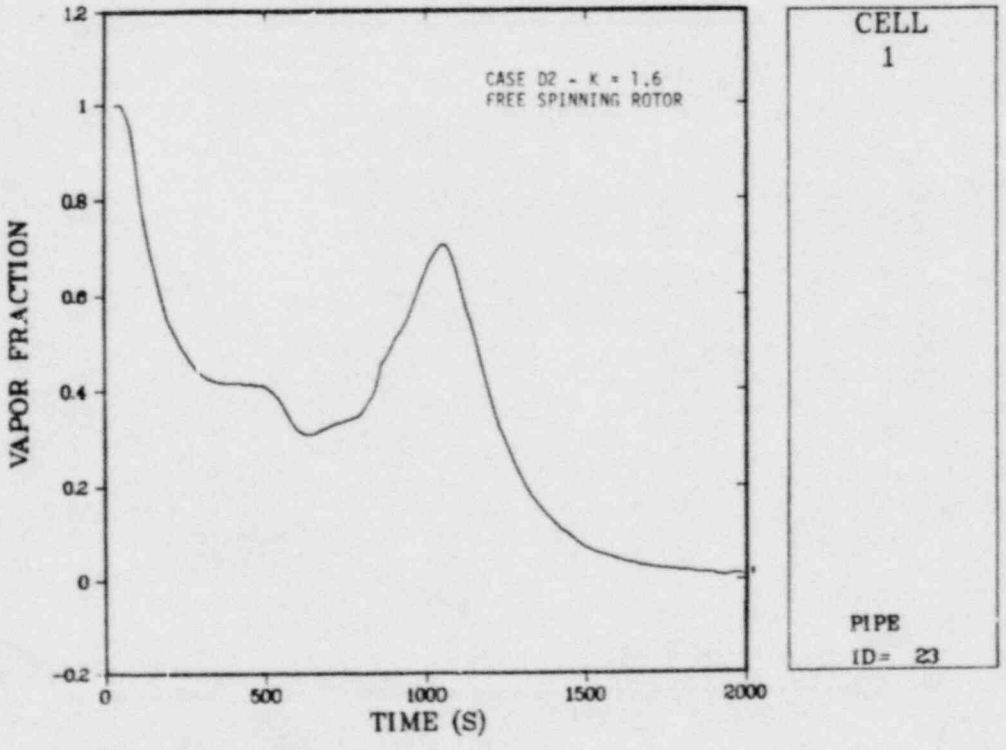

Fig. 36. TMI-2 pressurizer void fraction (top cell) for case D2 with free-spinning rotor.

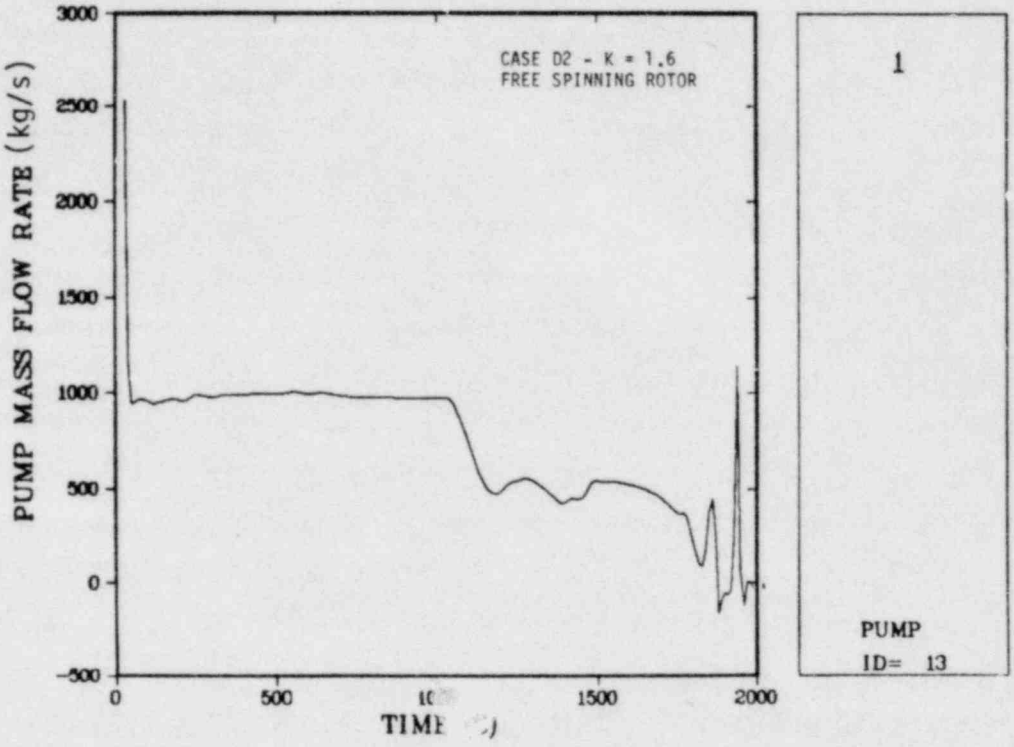

Fig. 37. TMI-2 Loop A pump mass flow rate for case D2 with free-spinning rotor.

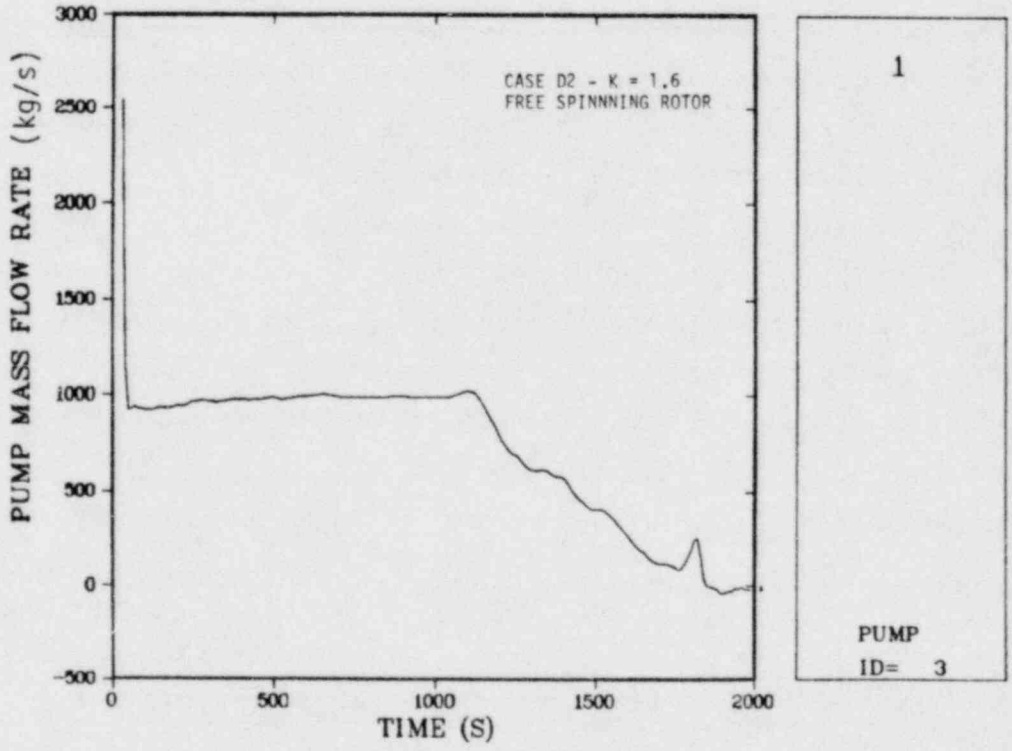

Fig. 38. TMI-2 Loop B pump mass flow rate for case D2 with free-spinning rotor.

heat source to add to the fluid so the system remains below saturation for a slightly longer time. However, the core void fraction at the top core level for the free-spinning pump case is significantly higher after 2 000 s for the free-spinning pump case when compared to the pump heat source case (0.6 compared to 0.2). This is due to increased phase separation after the pumps are tripped. In comparing the rod temperatures (Figs. 22 and 32) the temperature initially drops lower than the pump heat source case, but then begins to rise after about 500 s. This is due to a lower system pressure initially (Figs. 24 and 33) and then a pressurization period after about 1 000 s. The rod temperatures follow the saturation temperature after about 1 000 s.

The system pressure response and comparisons with the pump heat source case can be explained by the PORV flow, pressurizer water level, and pump flow rates (Figs. 26 and 34, 35 and 36, 28 and 37, and 30 and 38, respectively). At about 500 s, the pressurizer fills in the pump heat source case, which decreases the PORV volumetric flow causing a pressure increase. In the free-spinning pump case, the pressurizer does not fill so there is no pressure rise at about 500 s and the PORV mass flow rate thus remains lower during this period. However, after about 1 250 s, the pressurizer does fill and the system pressure begins to increase because of decreased volumetric flow. The PORV mass flow, however, increases because of the low-quality fluid being expelled through the valve. Another contributor to the pressure rise after about 1 000 s is a loss of steam generator heat transfer caused by a loss of natural circulation. Figures 37 and 38 show that the pump mass flows immediately drop to natural circulation values (~ 900 kg/s) after an initial pump coastdown of 60 s, and remain constant until the pump void fraction begins to increase at about 1 000 s. Then the flow rates drop and approach zero. Once the flows approach zero the natural circulation of the system is lost and steam generator heat transfer also is lost.

The total system water inventories at 2 000 s are almost identical (198 349 kg vs 202 510 kg for the pump heat source case). However, because the PORV flow rate is beginning to increase rapidly for the free-spinning pump case (Fig. 34), the inventories are expected to begin

diverging. Core uncovery for this case probably will occur earlier (at approximately an hour) because of

1. Earlier phase separation,
2. Core void fraction increasing at a much faster rate than the pump heat source case, and
3. Increasing PORV flow rate.

c. Case D2 -- Semilocked Pump Rotor Resistance K ~ 10.0

This calculation is identical to the previous one except that a higher pump resistance was used typical of a semilocked rotor (K = 10.0). It is a bounding type of calculation because the Semiscale pump model used is probably not representative of the full-scale TMI-type pumps; particularly the pump performance (resistance) after the pumps are tripped.

Key system parameter plots for the semilocked pump case can be found in Figs. 39-45. The time to upper head voiding is substantially less for this case compared to the pump heat source case (1 000 s vs 1 400 s -- Figs. 39 and 20, respectively). This is because the high pump resistance decreases the loop flow rates, causing lower flow velocities in the core and hence faster fluid heatup rates. The time at which saturation conditions are reached in the loops is 500 s compared to about 1 000 s for the pump heat source case. The rod temperatures initially are about the same as the pump heat source case (Figs. 22 and 40), but after significant core voiding occurs, which causes the pressure to rise, the temperatures begin to rise as they follow saturation.

Figures 41 and 24 show the system pressure comparisons. Initially, the pressure response is similar to the free-spinning pump case (Fig. 33), but then the pressu begins to rise rapidly after about 1 000 s. The pressure rise after 1 000 s is due to

1. Increased core voiding rate (Fig. 39) -- the pressure oscillations are a result of the void fraction oscillations in the core caused by "burping" of water into the core from the downcomer,

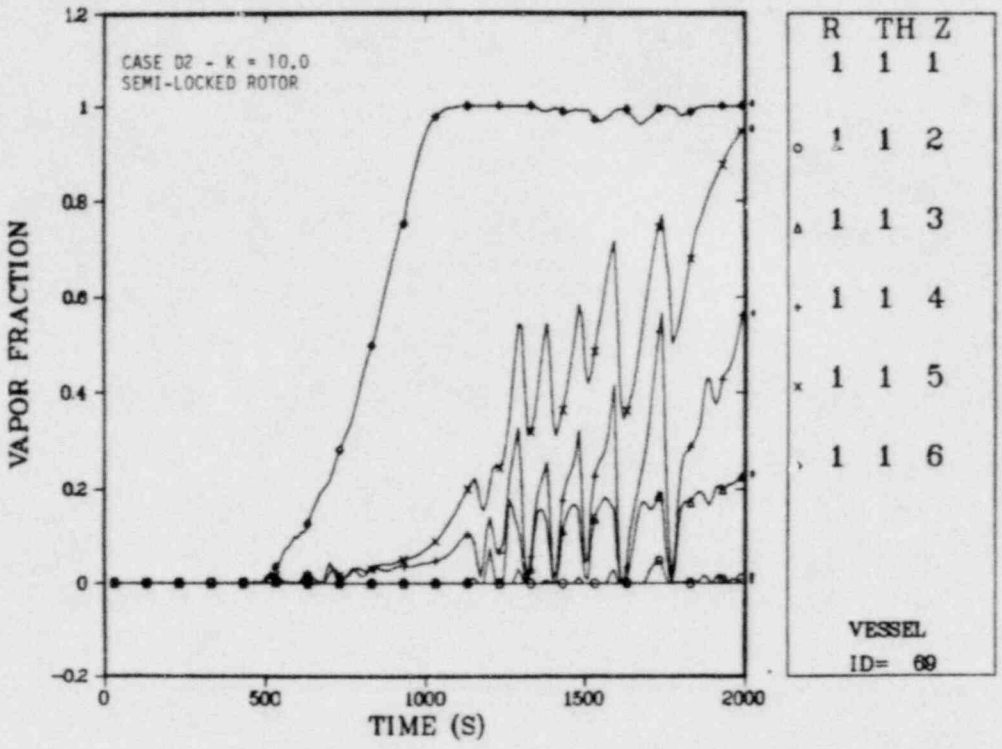

Fig. 39. TMI-2 vessel axial void fraction profile for case D2 with semilocked rotor.

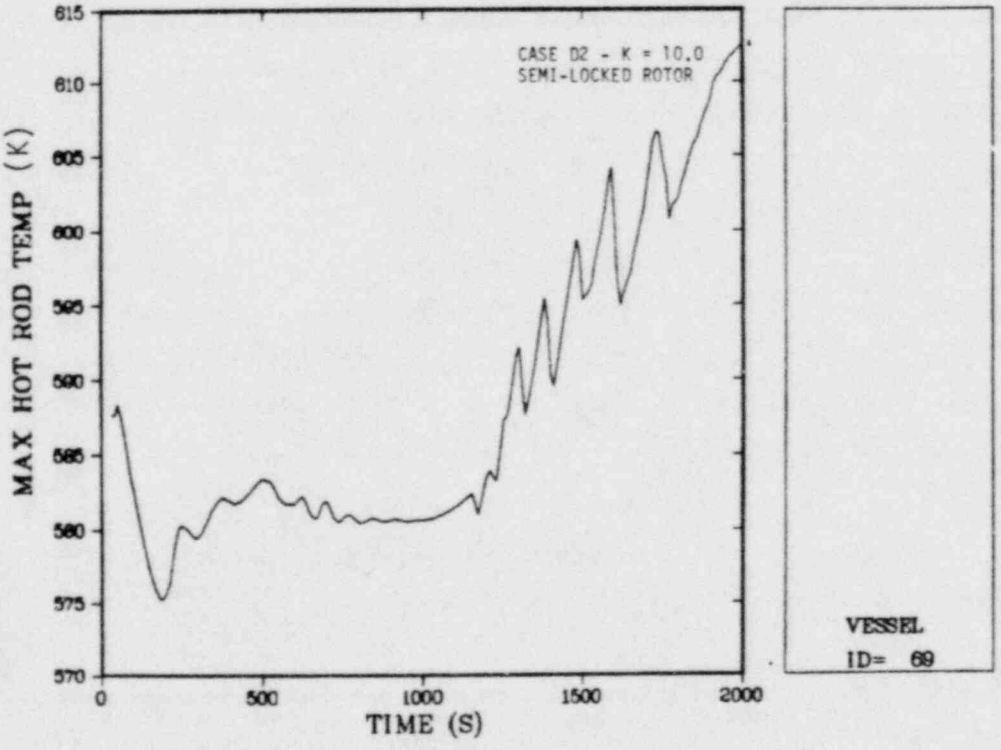

Fig. 40. TMI-2 hot-rod temperature history for case D2 with semi-locked rotor.

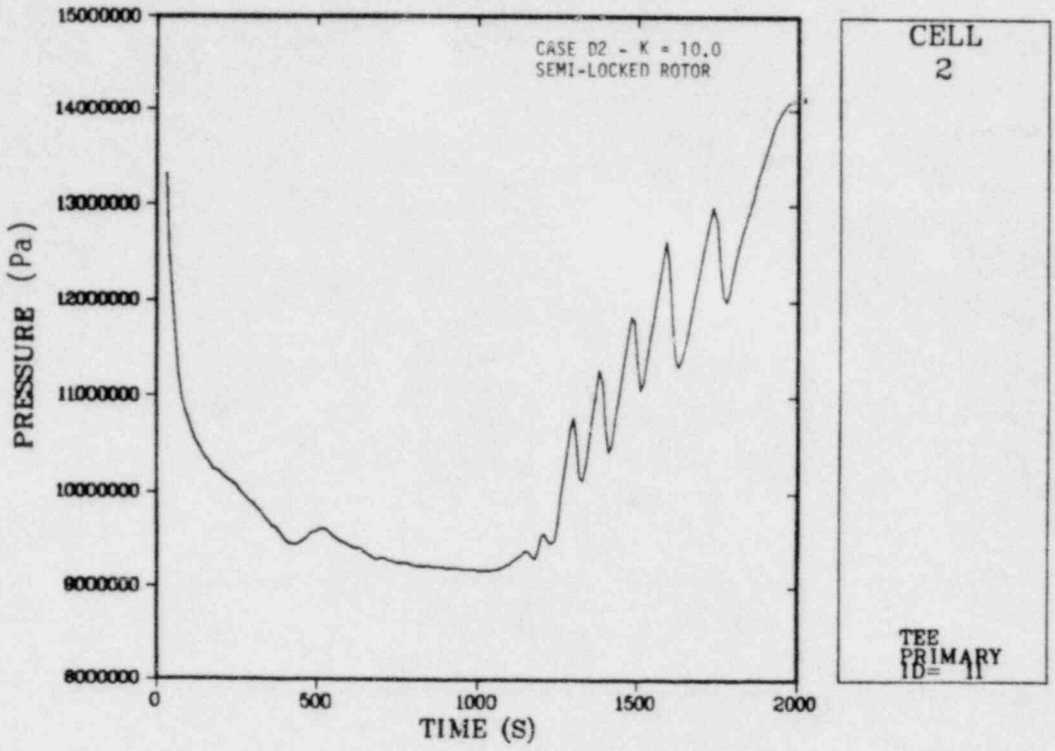

Fig. 41. TMI-2 system pressure for case D2 with semilocked rotor.

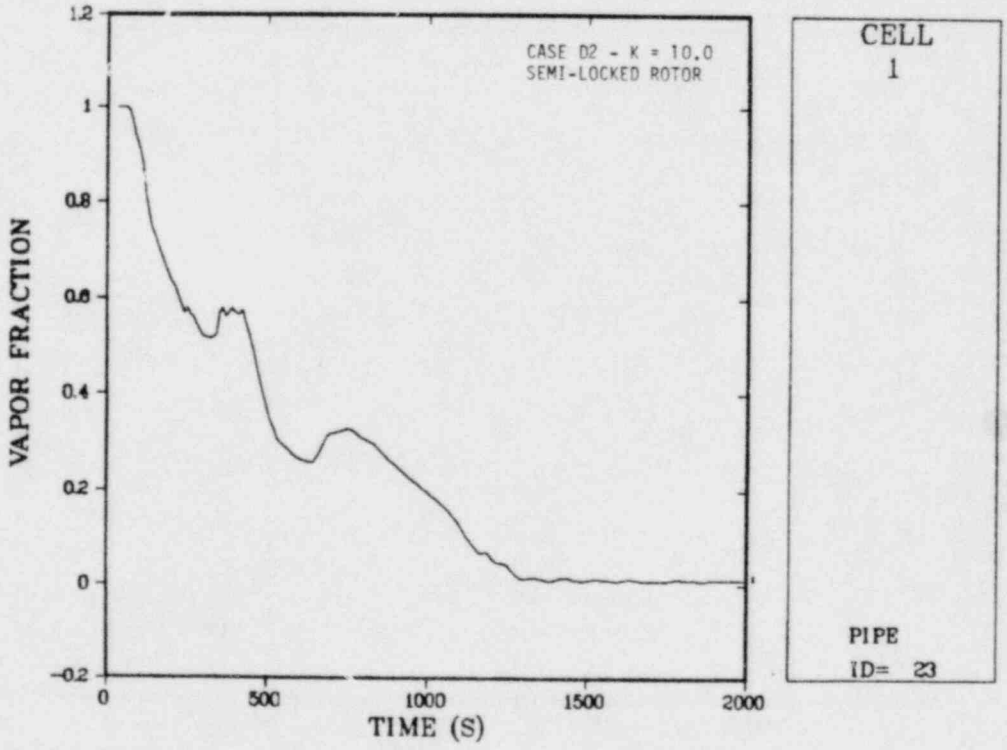

Fig. 42. TMI-2 pressurizer void fraction (top cell) for case D2 with semilocked rotor.

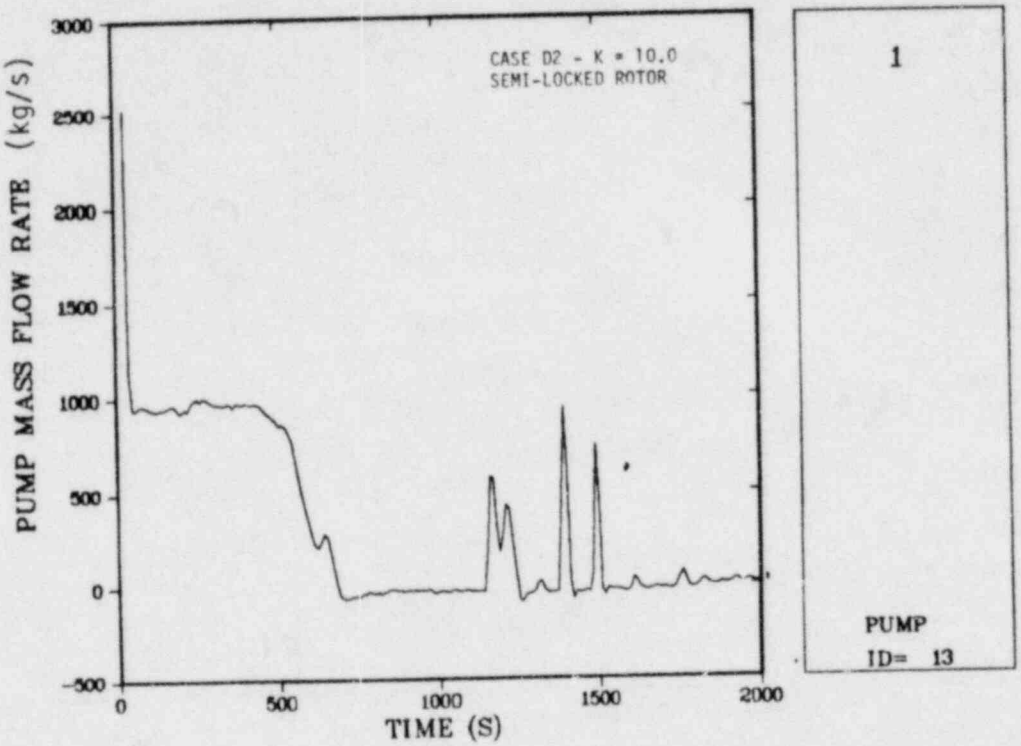

Fig. 43. TMI-2 Loop A pump mass flow rate for case D2 with semilocked rotor.

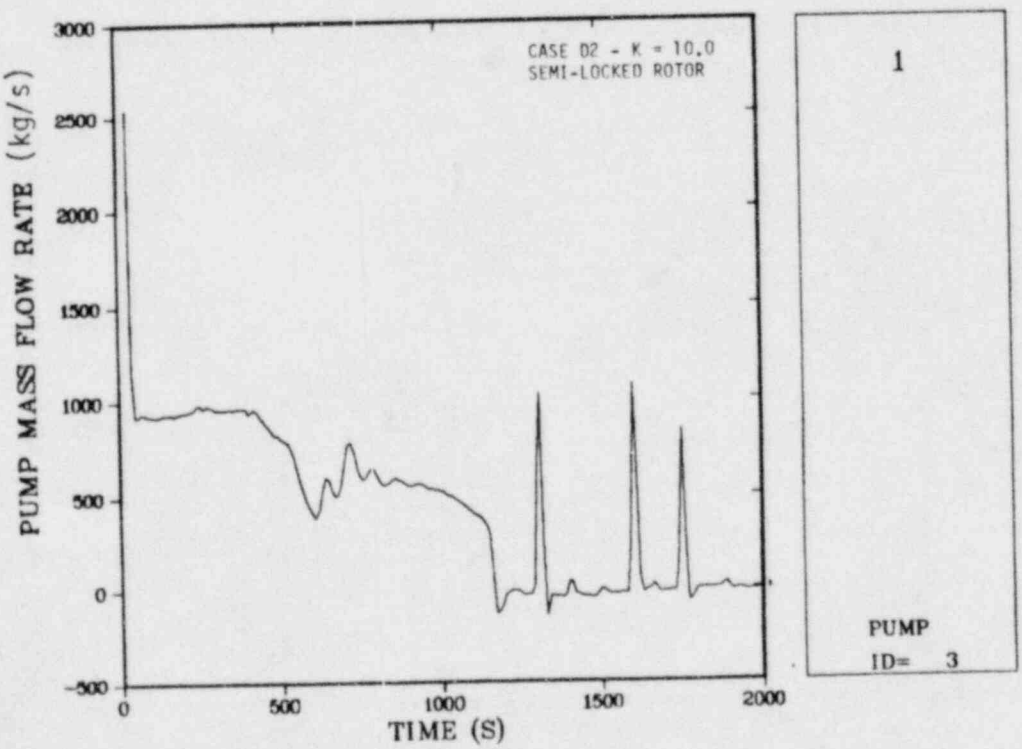

Fig. 44. TMI-2 Loop B pump mass flow rate for case D2 with semilocked rotor.

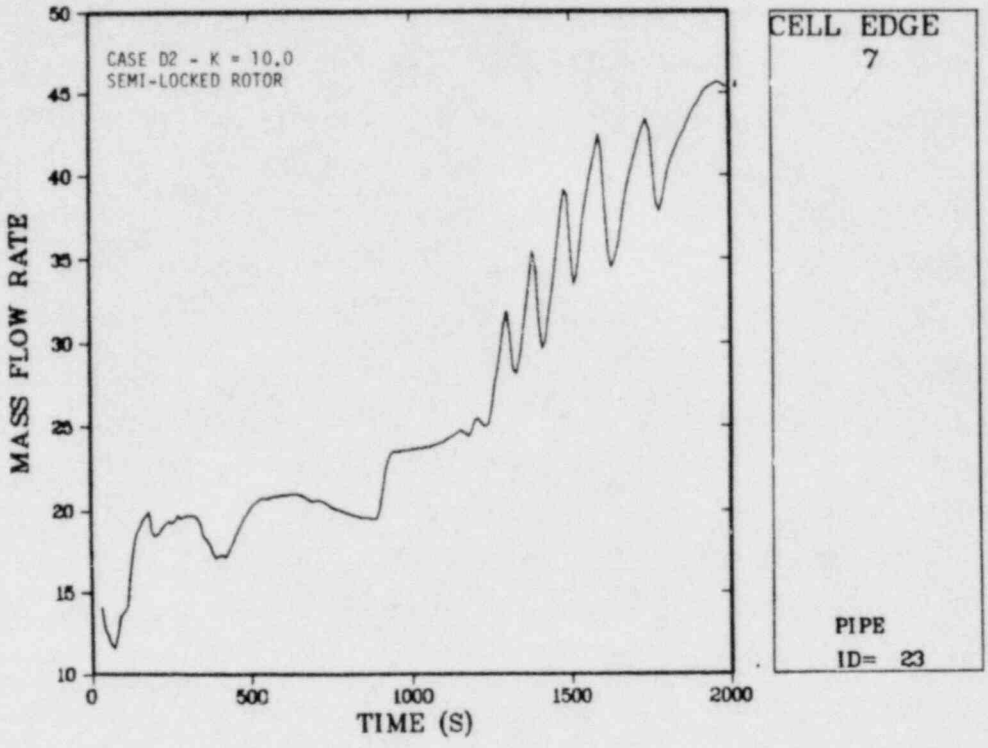

Fig. 45. TMI-2 PORV flow rate for case D2 with semilocked rotor.

2. Pressurizer fills reducing the volumetric flow out of the PORV (Fig. 42), and

3. Loss of steam generator heat transfer due to loss of natural circulation (Figs. 43 and 44).

The pump flows initially drop to natural circulation values (~ 900 kg/s) similar to the free-spinning pump case, but natural circulation is not sustained nearly as long because of increased system voiding. Natural circulation is lost at about 500 s compared to about 1 000 s for the free-spinning pump case. The increased core voiding rate after 1000 s (Fig. 39) is responsible for not only the loss of natural circulation, but also the filling of the pressurizer (Fig. 42). Thus, as the system pressure increases (Fig. 41) due to the increased core voiding rate, the system bulk temperature increases as does the fluid specific volume (fluid "swell"). As can be seen from Figs. 41 and 42, the pressurizer void fraction basically follows the trends in the system pressure and fluid temperature. The pressurizer void fraction

(Fig. 42) in the top pressurizer node thus decreases (level rise) as the system bulk liquid specific volume increases because of the rise in fluid temperature. Because the PORV is expelling low quality liquid when the pressurizer fills, the mass flow rate increases (Fig. 45). The PORV mass flow rate after 2 000 s is much higher than the pump heat source case (Fig. 26) and the free-spinning pump case (Fig. 34), so the system inventory is much less (185 430 kg compared to 202 510 kg for the pump heat source case and 198 349 kg for the free-spinning pump case).

Core uncovery for this case will probably occur much earlier when compared to the base case or pump heat source case for the same reasons discussed in the preceding section (free-spinning pump case) plus the fact that the PORV mass flow rate is significantly higher for this case. Finally, it is apparent that the results obtained for Case D2 are highly dependent on the pump resistance.

Thus, for the assumptions used, it is more beneficial to leave the pumps running as long as possible for a TMI-2-type transient because the benefits obtained by forced convection heat transfer far outweigh the benefits of removing a small, additional heat source supplied to the fluid by the pumps.

C. Independent TRAC Assessment

(J. C. Vigil and T. D. Knight, Q-6)

Independent assessment of TRAC mainly involves pretest and posttest predictions of tests in designated facilities using the publicly released and documented versions of TRAC. The primary objective of this activity is to determine the predictive capability of TRAC when applied to new tests involving different scales and experimental configurations. Independent assessment also includes posttest analyses as necessary to resolve discrepancies between the code predictions and the test results. Recommendations for future code development or experiments and participation in the NRC standard problem exercises are also part of this activity.

During this quarter the independent assessment of TRAC continued and the LOFT test L2-3 pretest prediction was compared to data. Pretest predictions for LOFT small-break test L3-1 and LOBI test A1-01 were completed. Preliminary comparisons of the L3-1 prediction to data are under way and input model changes necessary for the LOFT small-break test L3-2 pretest prediction are being made.

1. LOFT Test L2-3 Data Comparisons

(T. D. Knight, Q-6)

In addition to the difficulty in calculating rewets observed in the L2-2 comparisons,[1,23] the calculated broken loop cold-leg mass flow for L2-3 underpredicts the data during the first 5 s.[14] This underprediction of the broken cold-leg flow results in an apparent overprediction of core inlet flow. The ultimate effect is that the dryout behavior in the core is not well calculated (separate from the rewet behavior).

The problem of the calculated flow in the broken loop cold-leg nozzle has been investigated. Briefly stated, when the fluid cells in the nozzle depressurized to saturation ($T_{sat} = T_{liquid}$), immediate vapor generation occurred. The critical flow characteristics changed from those of subcooled and nonequilibrium to saturation and near equilibrium and resulted in the underprediction of critical flow. The problem was not as severe in the broken loop hot leg because of the higher flow resistance and higher temperature.

The vapor generation model did not account for the effect of delayed nucleation, and at low void fractions forced near equilibrium conditions between the phases. Only small levels of superheat were observed for low void fractions. This problem was more apparent in the LOFT small-break test L3-1 calculation described below.

2. LOFT Test L3-1 Pretest Prediction

A pretest prediction for LOFT small-break test L3-1 was completed. Test L3-1 was to be conducted from steady-state conditions of 50 MW(t) initial power and primary coolant loop flow of 478.8 kg/s. ECC consisted of the high-pressure injection system (HPIS), the accumulator, and the low-pressure injection system (LPIS) injecting into the intact loop cold leg. The broken loop hot-leg isolation valve was closed. The break simulator orifice installed in the broken loop cold leg had a 1.6-cm i.d.

The test was initiated by manually tripping the reactor. When the control rods reached bottom, the pumps were tripped and the quick opening blowdown valve in the broken loop cold leg was opened.

The TRAC input model was developed by combining the ECC system and fuel specifications from the LOFT L2-3 input deck with the L3-0 input deck. Some additional nodalization changes were made, and the elevation terms were corrected in the piping components. Additional consistency changes were made. The nodalization for test L3-1 is shown in Fig. 46; the input model consisted of 24 separate components involving 124 fluid cells. The vessel consisted of two radial rings, two azimuthal segments, and nine axial levels. The core was located in ring 1, levels 3 through 6. As requested, the pretest prediction was terminated at 1 500 s. The calculation was made with TRAC-P1A[5] with certain coding updates.[24]

Since the completion of the pretest prediction, data have been obtained from the quick-look report.[25] Figure 47 shows the comparison of the calculated hot-leg pressure and the data. The pressure was overpredicted for the first 1 200 s. The calculated pressure rise from 150-250 s was related to the loss of natural circulation cooling, and the core, while not drying out, began to heat slowly. The pressure rise was terminated by clearing the intact loop seal and venting steam from the hot-leg side to the break. The overprediction of pressure was the direct result of underpredicting the cold-leg break flow (Fig. 48). (The first five data points were shown as discrete points in the quick-look report.) Clearly, the subcooled critical flow was significantly underpredicted, and then from 50-400 s, the calculated flow leveled out on a plateau of much longer duration than can be inferred from the data. The calculated and measured cladding temperatures essentially followed saturation with no sustained dryouts.

The calculated flow in the broken loop cold leg has been investigated. Three problems were apparent.

1. Upstream of the orifice, voids appeared by 7 s. These voids had been convected from the intact loop hot leg. Void fractions between 1 and 2% existed in liquid subcooled as much as 30 K.

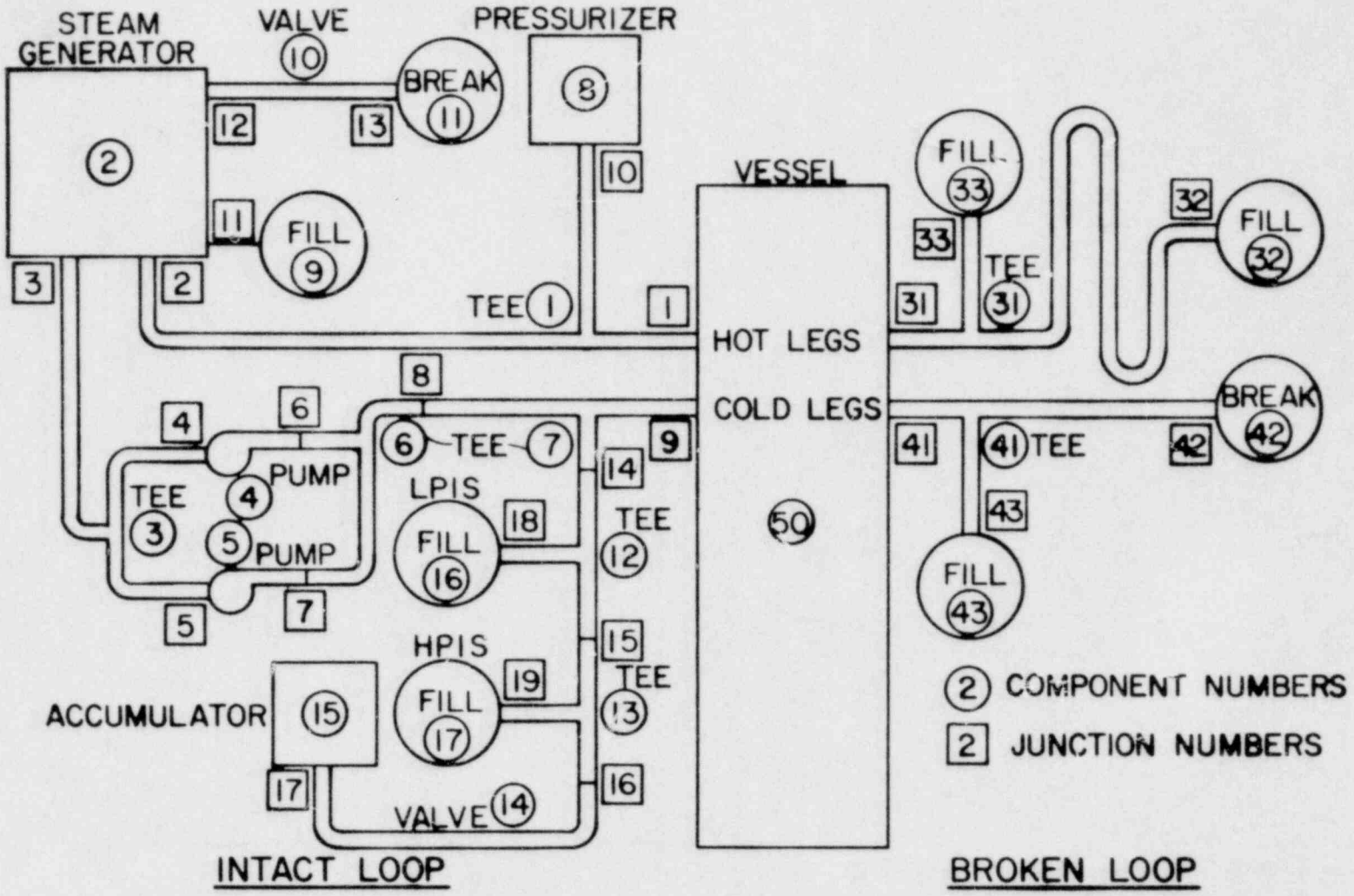

Fig. 46. TRAC model for LOFT test L3-1.

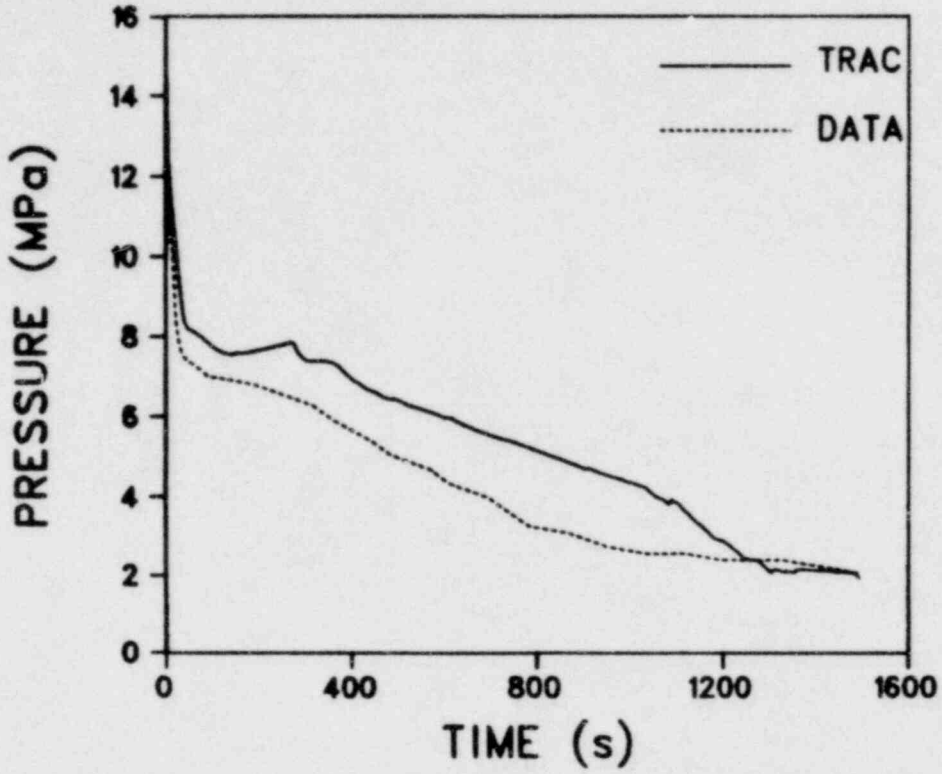

Fig. 47. Comparison of the pretest prediction of hot-leg pressure to the data (PE-PC-5) for LOFT test L3-1.

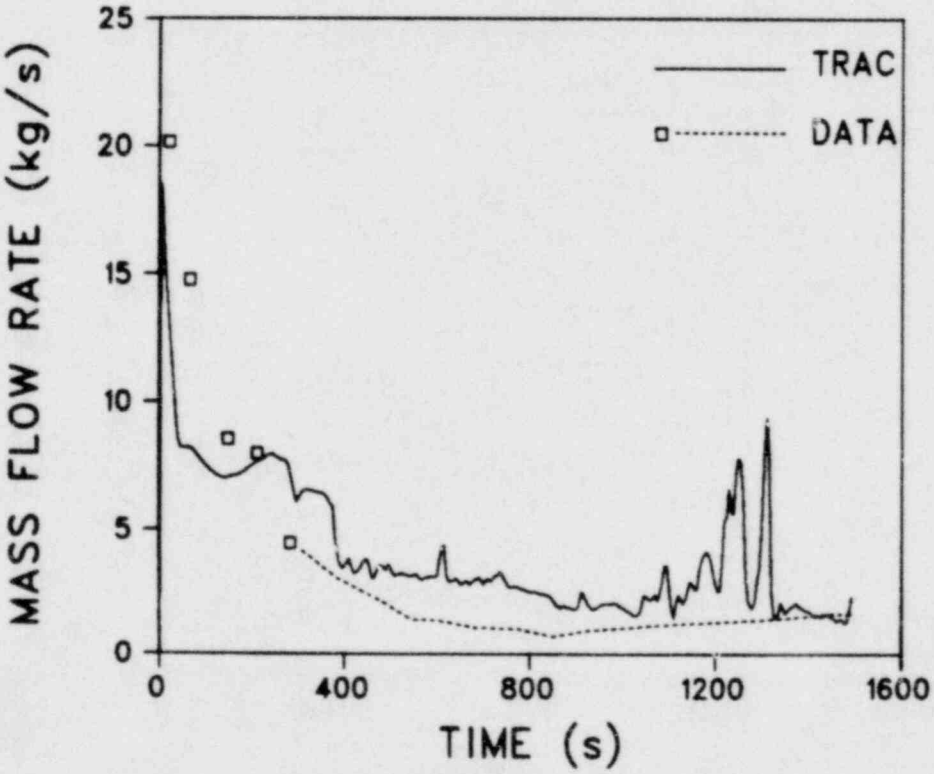

Fig. 48. Comparison of the pretest prediction of the broken loop break flow with the data for LOFT test L3-1.

2. Voids were being generated within the orifice (total length of 5.4 cm) as soon as the local conditions reached saturation. The calculated residence time of fluid within the orifice was less than 0.4 ms.

3. On the plateau between 50 and 400 s, the void fraction leveled off between 0.7 and 0.8 with the residual liquid carrying 30 K superheat.

Problems 1 and 2 have been addressed. For problem 1, we removed the code logic that limited interphase heat transfer for void fractions less than 10% when the liquid was subcooled. The second problem was resolved for the current case by updating the code to prohibit vapor generation within the orifice cells when the local void fraction was less than 5%.

A posttest calculation has been performed to test the code changes. Figure 49 shows the comparison of the posttest calculated break flow and the data (discrete points). The pretest calculated break flow also is included. At 150 s in the posttest calculation, voids were convected into the orifice, and the local void fraction increased rapidly to 0.75. The posttest break flow calculation is more typical of subcooled critical flow and transition to saturated critical flow than is the pretest calculation. The comparison to the limited number of data points is improved also. Comparisons of the posttest and pretest calculated intact loop cold-leg pressures to the data are shown in Fig. 50. While the pretest prediction overpredicted the pressure throughout the 200 s shown, the posttest calculation agrees well with the data and yields the correct trends. The posttest calculation pressure comparison further supports the conclusions drawn relative to the break mass flow comparisons.

3. Pretest Prediction of LOBI Test A1-01

(C. E. Watson, Q-6)

We completed a final pretest prediction of the thermal-hydraulic response of the first LOBI test (A1-01)[26,27] at the Joint Research Center (ISPRA Establishment) of the Commission of the European Communities. This test simulates a double-ended, 200% break in the cold leg, initiated from nominal steady-state conditions. Emergency

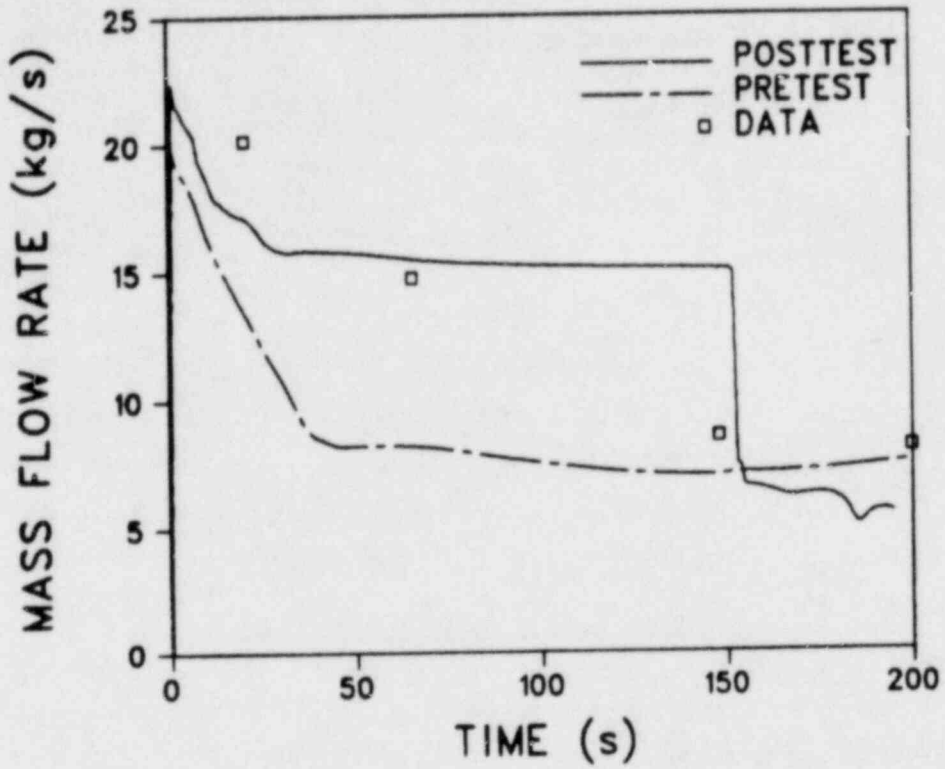

Fig. 49. Comparison of posttest and pretest calculated break flows to LOFT test L3-1 data.

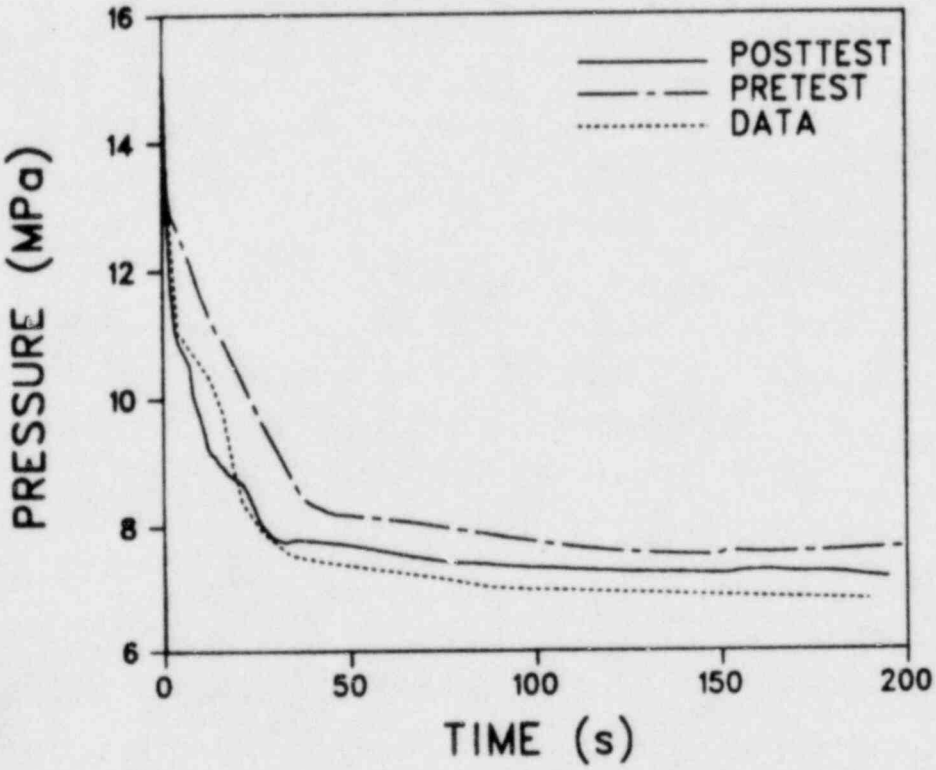

Fig. 50. Comparison of posttest and pretest calculated intact loop cold-leg pressure to LOFT test L3-1 data (PE-PC-1).

core cooling water from the accumulator is injected into the intact loop cold leg only.

The version of the TRAC code used for the pretest prediction was TRAC-P1A with the coding error corrections given in the first TRAC newsletter.[24] The input model incorporates the most recent information available from ISPRA including single-phase pump performance data. A schematic diagram of the TRAC model is shown in Fig. 51. The vessel components modeled are the inlet annulus, downcomer, upper and lower plena, and the core. The core bypass was not modeled because the bypass flow is small in comparison to the core flow. The power distribution is cosine-shaped in the axial direction and uniform in the radial and angular directions, as given in Ref. 26. The pumps were modeled using the single-phase head curves of Ref. 28 and adjusted Semiscale two-phase head curves. The nozzle used to simulate the break is a convergent-divergent type. We determined that 10 nodes were adequate to obtain numerical convergence for the mass flow rate.

The steady-state initial conditions were obtained in two stages. First, each component was calculated separately using anticipated inlet conditions. Then, the coupled system was run to make the final (small) adjustments to obtain the best match to the anticipated conditions. The system response to the depressurization was then calculated for the period 0 to 70 s.

Figures 52 and 53 show the calculated flow rates from the vessel and pump side breaks, respectively. The flows start from zero and attain their maximum values of 66.5 and 33.8 kg/s at 0.021 and 0.15 s. The flow then falls off in a manner typical of subcooled and saturated blowdown.

The average rod clad temperature goes through a maximum (611.6 K at 0.51 s) during the first core flow reversal as in Fig. 54. The peak temperature occurs so early in the transient partly because the core power is turned off at 1.0 s. The broken loop pump is stopped at 2.0 s while the intact loop pump is ramped to 70% of initial speed at 5.0 s.

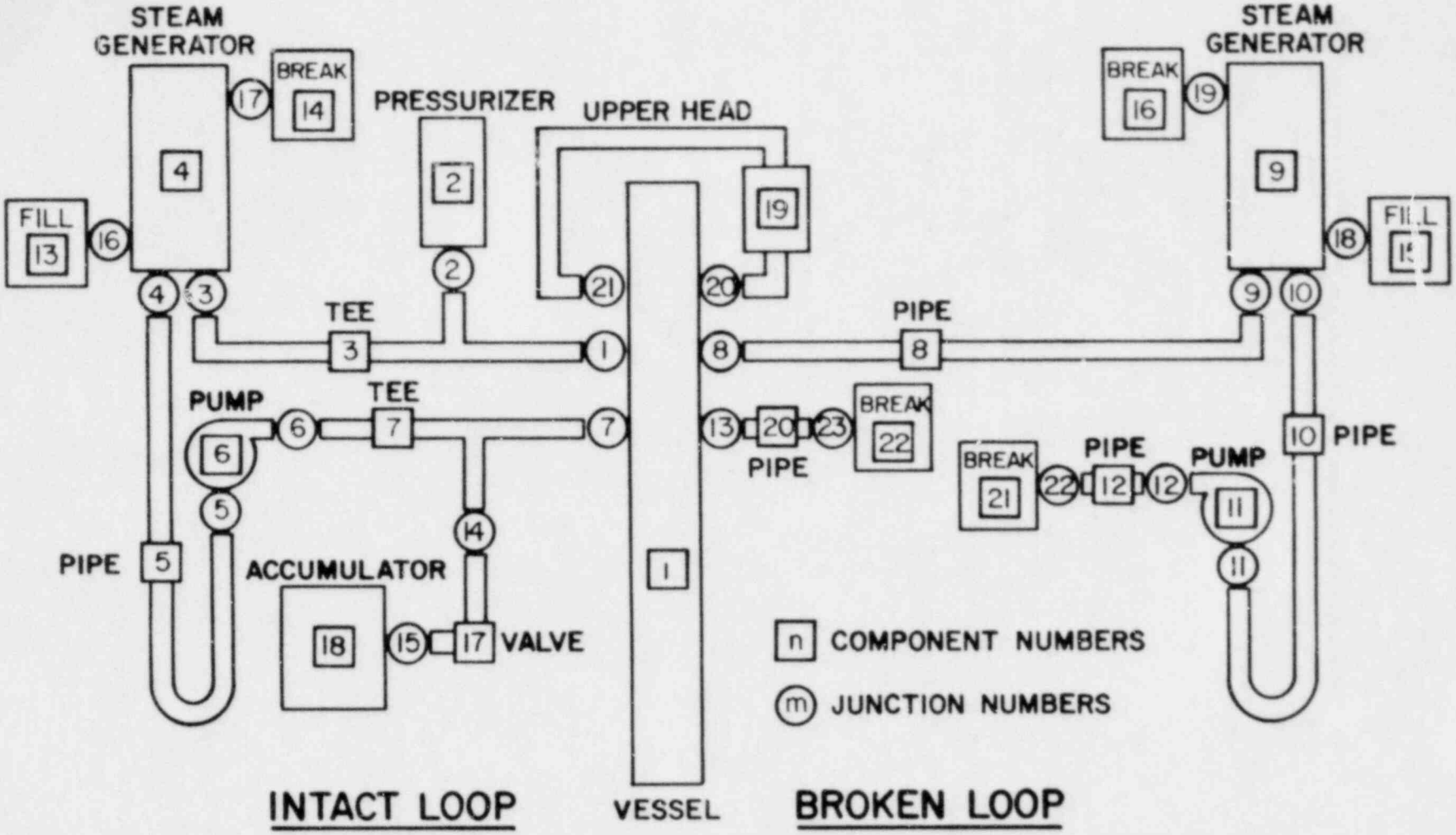

Fig. 51. TRAC model schematic of LOBI facility.

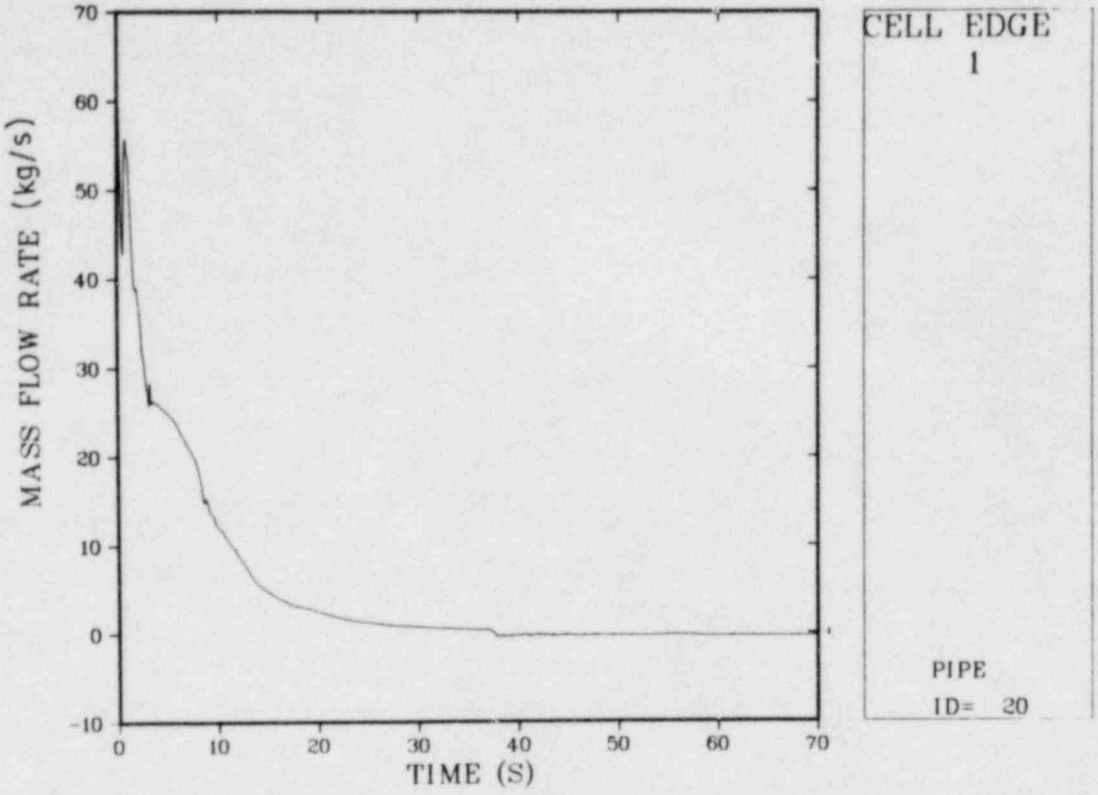

Fig. 52. Mass flow rate at vessel side break in LOBI experiment A1-01.

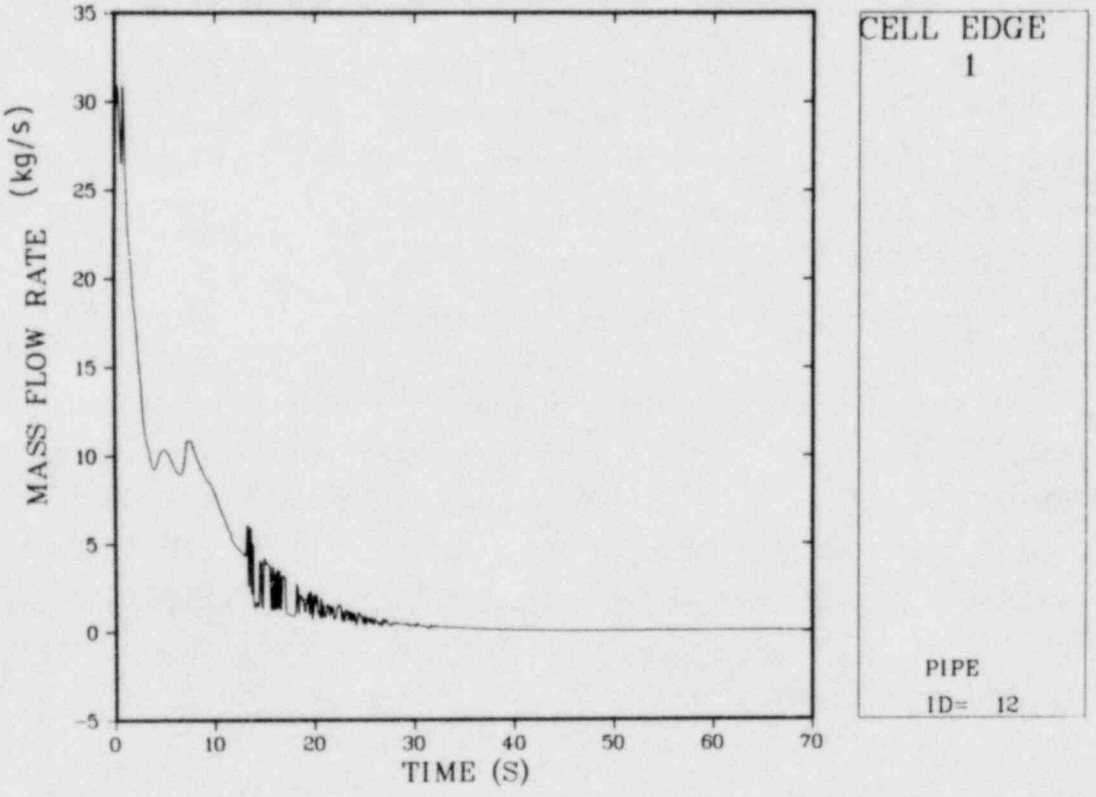

Fig. 53. Mass flow rate at pump side break in LOBI experiment A1-01.

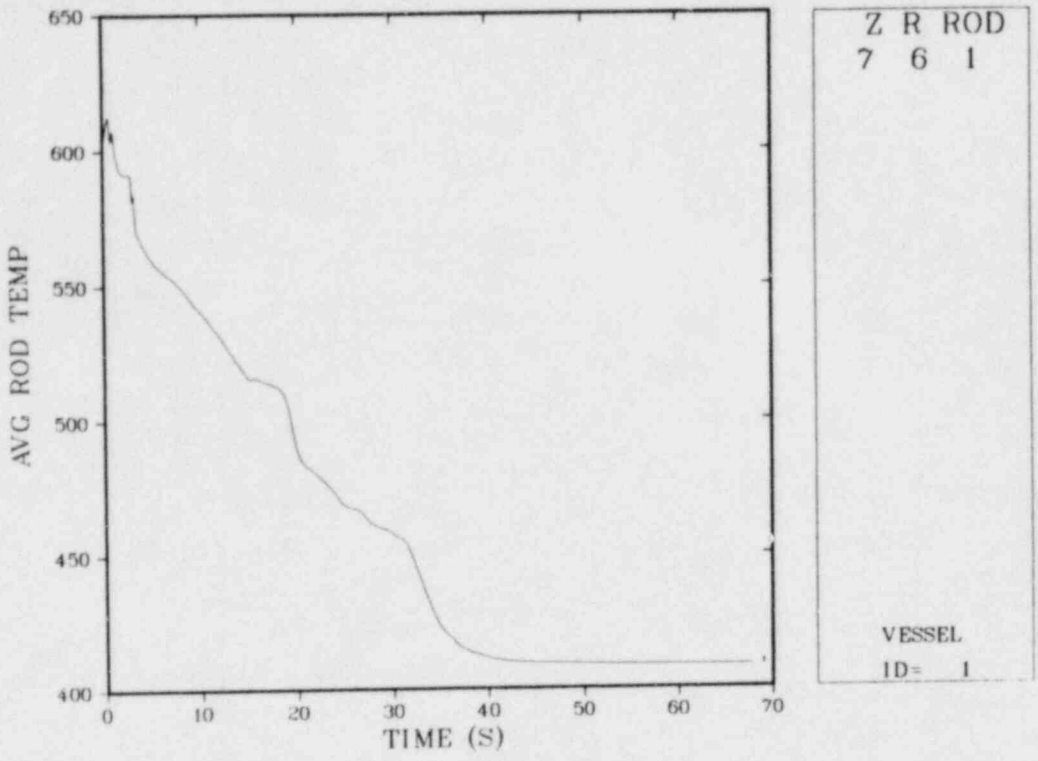

Fig. 54. Average rod temperature (clad surface) in LOBI experiment A1-01.

The pressurizer almost empties during the first 12 s and is 5% full at that time. Accumulator injection is tripped on at 17.7 s, when the pressure in the intact cold leg reaches 2.7 MPa. The accumulator flow rapidly reaches a maximum of 2.1 kg/s and decays slowly to a value of 1.5 kg/s at 70 s as shown in Fig. 55.

Injected liquid begins to pass downward in the downcomer at 24.2 s with the minimum in the vessel liquid mass inventory occurring at 28 s as shown in Fig. 56. The system pressure reaches the assumed back pressure of 0.3 MPa at 40 s and bypass completely ends at the same time. At the end of the calculational period, the accumulator is 43% full.

A list of the sequence of events is given in Table III. Overall, these results are strongly dependent on the calculated break flow and energy release that largely determine both the system pressure and its response to the depressurization.

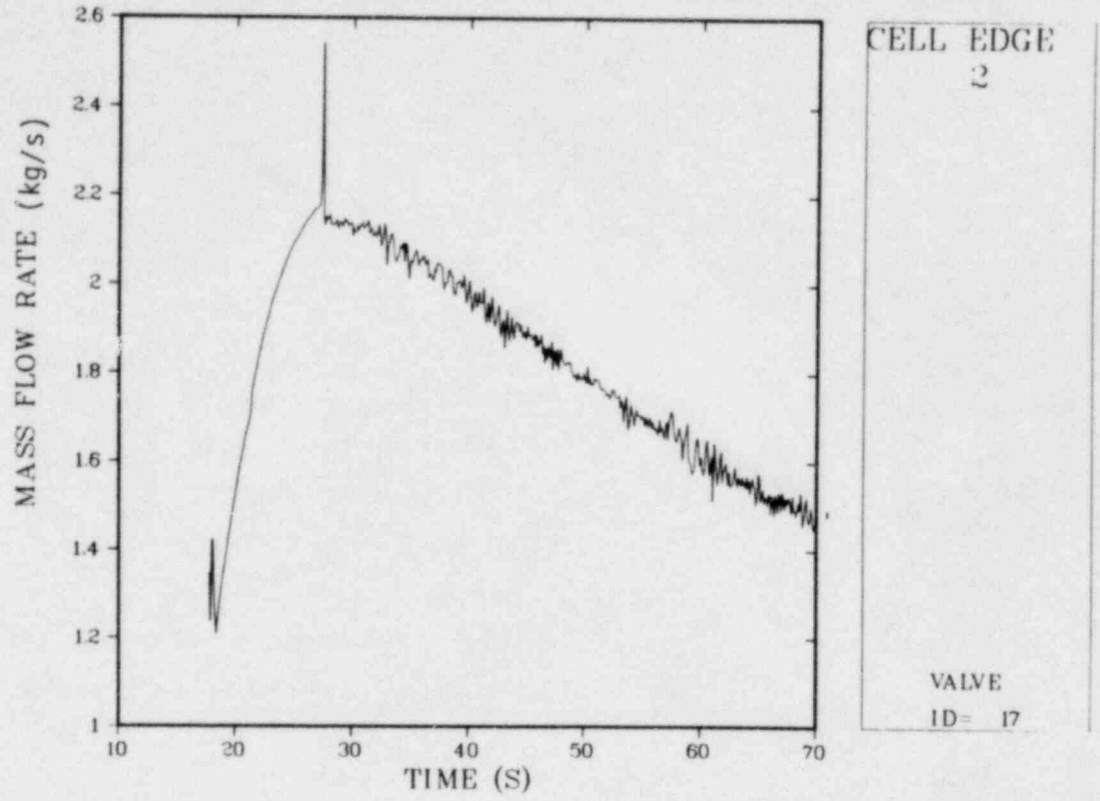

Fig. 55. Accumulator mass flow rate in LOBI experiment A1-01.

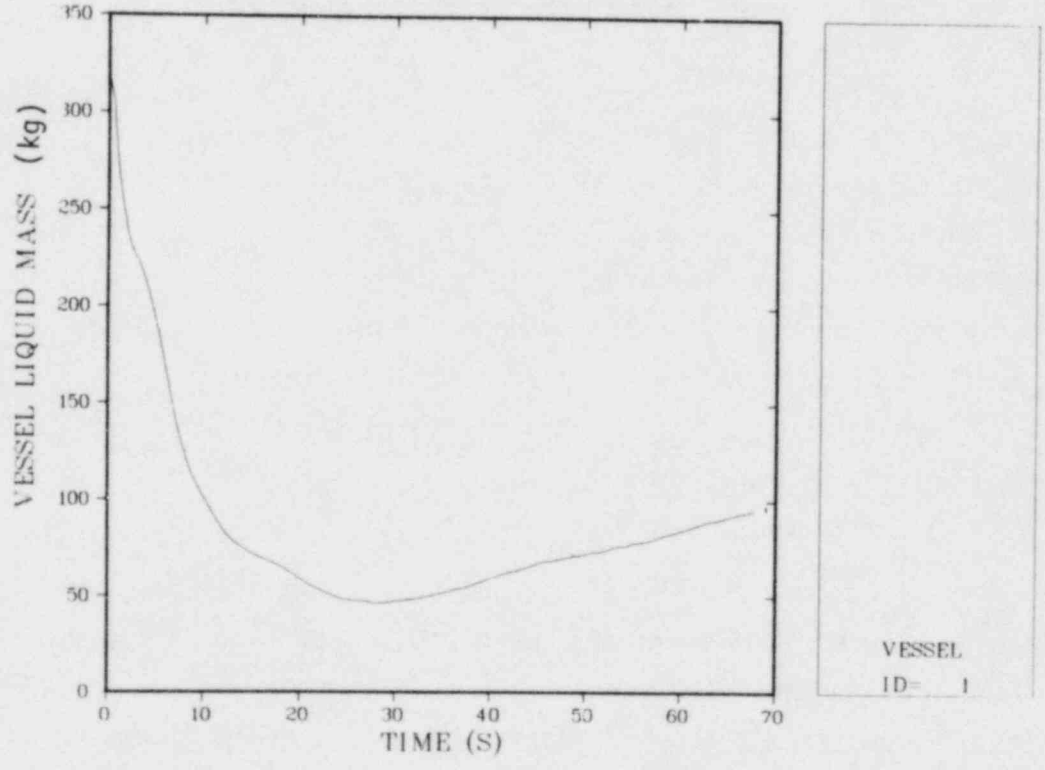

Fig. 56. Vessel liquid mass in LOBI experiment A1-01.

TABLE III

CALCULATED SEQUENCE OF EVENTS

Time (s)	Event
0.0	Break Opens
0.2	Core Flow Reversal
0.51	Maximum Average Rod Temperature at Surface
1.0	Core Power Turned Off
2.0	Broken Loop Pump Stopped
5.0	Intact Loop Pump Ramped to 70%
17.7	Accumulator Valve Opens
28.0	Vessel Liquid Mass Turnover
40.0	System Pressure Reaches Back Pressure and Bypass Completely Ends
70.0	End of Calculation

D. Thermal-Hydraulic Research for Reactor Safety Analysis

(W. C. Rivard, T-3)

The nonequilibrium flashing model for critical two-phase flow that has successfully described the Semiscale and Marviken experiments was further tested against low-pressure data from the MOBY DICK and Brookhaven National Laboratory (BNL) experiments. The results show quite good agreement with the measured flow rates and steady-state profiles of pressure and void fraction.

Critical Flow Studies

(J. R. Travis and W. C. Rivard, T-3)

An important part of LWR safety analyses is the prediction of critical flow rates or maximum discharge flow rates through a pipe break. Nonequilibrium effects are often important during the initial phase of blowdown when subcooled water undergoes a rapid depressurization. To calculate the discharge flow rate, we have developed a

macroscopic model of flashing[1] that is based on a description of turbulence-enhanced heat transfer and a Weber number criterion for bubble size. In a quiescent environment, the model reduces to the well-known conduction controlled rate. The model has been tested against data obtained from the Semiscale Mod-1 apparatus at the Idaho National Engineering Laboratory (INEL) and the full-scale Critical Flow Test (CFT) project at the Marviken Test Station in Sweden.[1,29] These tests involve fluid pressures and temperatures typical of actual PWR operating conditions (5-9 MPa and 530-575 K). Pipe sizes range from the large 75-cm-diam pipes typical of present reactor systems to diameters of a few centimeters. Excellent agreement was obtained between calculations and data for these tests.[14]

As a further check of the flashing model, the low-pressure MOBY DICK Loop[30] at the Nuclear Studies Center in Grenoble, France and the BNL Loop[31] were analyzed. These tests involve fluid pressures between 0.1 and 0.4 MPa and temperatures around 373 K. Extension of the nonequilibrium model to these low pressures has been achieved by extending the functional relationships for the turbulence intensity and the nucleation sites per unit volume to the lower pressure range. The calculational results obtained at the higher pressures remain unchanged. Inlet pipe sizes to the test sections are 2 and 5 cm, for the MOBY DICK and BNL experiments, respectively. The test section geometries are shown in the figures discussed below. Detailed axial profiles of pressure and void fraction were measured in both facilities. It is interesting to note[31] that BNL constructed both diameter-averaged and area-averaged void fraction profiles from their five beam γ densitometer measurements. The differences between these suggest the presence of a liquid core surrounded by steam. Because the one-dimensional equations in K-FIX are area-averaged, the calculated results should be compared with the area-averaged data.

Figure 57 shows the K-FIX steady-state calculated results compared with data for MOBY DICK test 403. Inlet conditions 139 cm upstream of the divergent test section are subcooled water at 0.183 MPa and 390 K. In the BNL experiments, considerable effort was made to calibrate their test section. In Fig. 58 the results of a classical Bernoulli

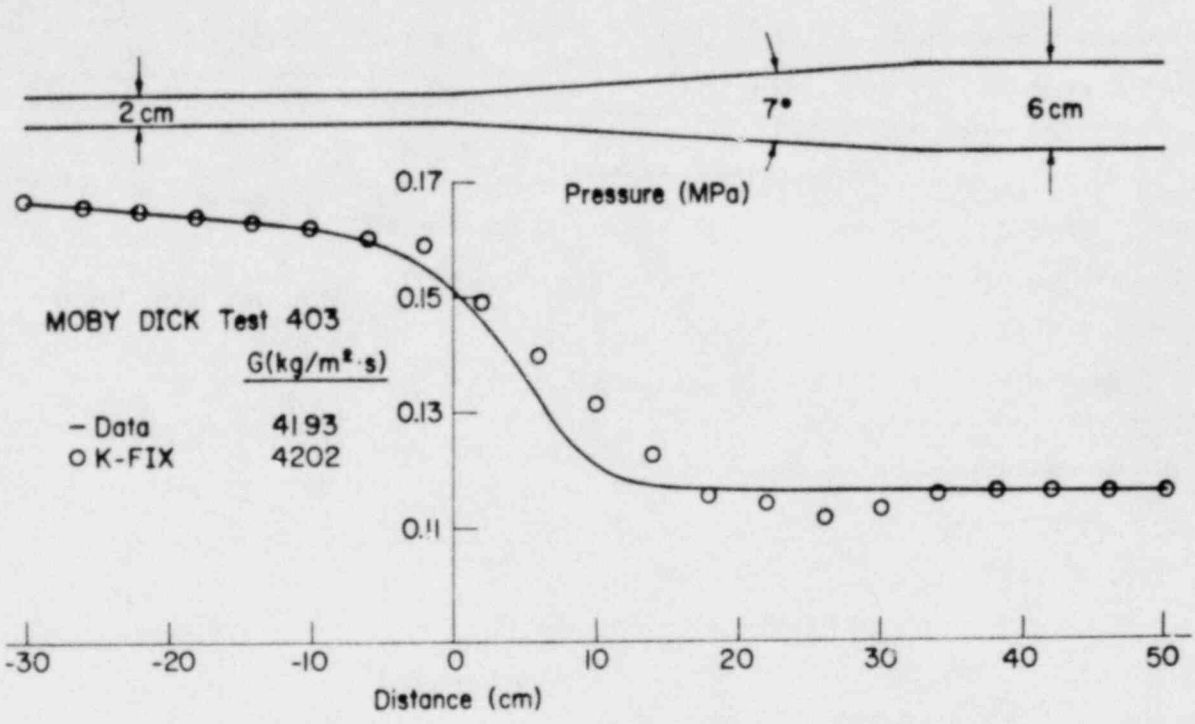

Fig. 57. MOBY DICK nozzle geometry and measured axial pressure profile for test 403. The calculated values were obtained for non-equilibrium (0) vapor production.

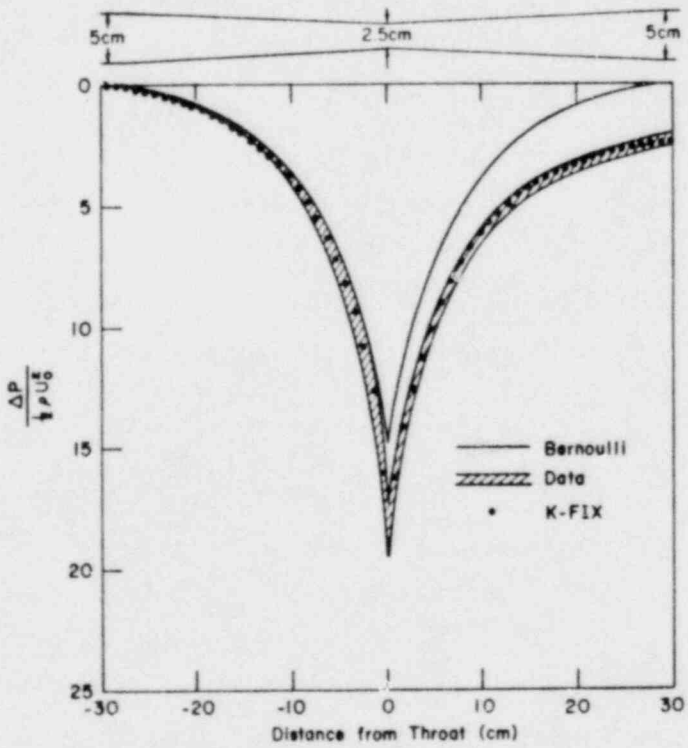

Fig. 58. BNL nozzle geometry and pressure profiles for single-phase liquid flow.

solution and a K-FIX calculation are compared with the measured pressure profile for single-phase liquid flow. In Figs. 59 and 60, the nonequilibrium and equilibrium calculated results are compared with the measured pressure profiles for BNL tests 130 and 77, respectively. For test 130 (Fig. 59), calculated results also are compared with the measured area-averaged void fraction profile. These data are not available for test 77. The calculated vapor production rates are shown for both tests to display the flashing location and magnitude. The success of these calculations adds further support to the predictive ability of the nonequilibrium vapor production model. No difficulties arose in going from small- to full-scale geometries or extending the pressure range to low pressures, because the model is based on local flow and thermodynamic conditions.

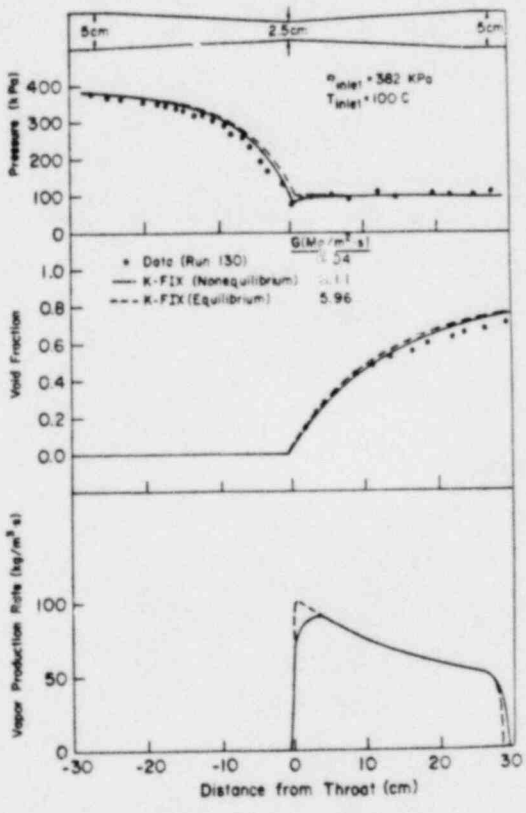

Fig. 59. BNL nozzle geometry and pressure distributions, void fraction profiles, and vapor production rates for test 130.

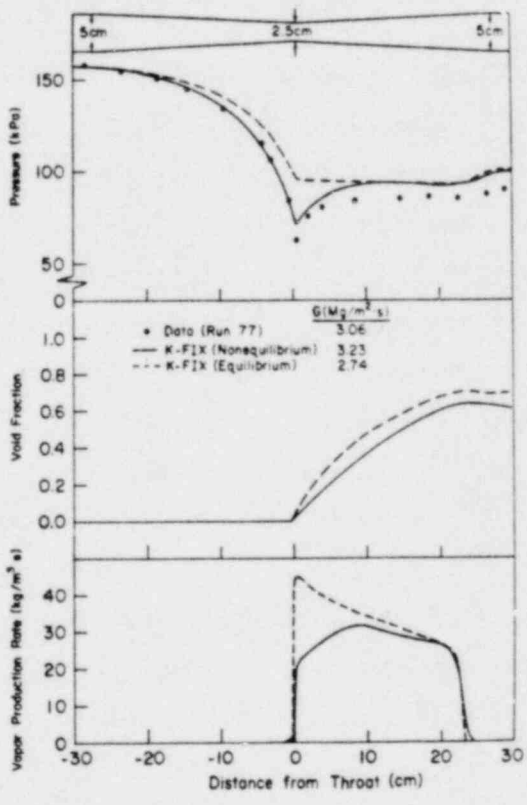

Fig. 60. BNL nozzle geometry and pressure distributions, void fraction profiles, and vapor production rates for test 77.

E. LWR Experiments

(W. L. Kirchner, Q-8)

The LWR Safety Experiments Program is conducted in support of model development, applications, and code assessment activities of the TRAC program. Current projects include investigating de-entrainment phenomena in the upper plena of PWRs during LOCA conditions and developing video-optical systems for viewing within the test vessels of large LOCA experiment facilities (part of a multinational refill/reflood research program). Tests are being conducted on multirod simulations of a PWR upper plenum to extrapolate single internal results to more prototypical configurations.

1. Video-Optical Systems

(J. F. Spalding and C. R. Mansfield, Q-8)

A new probe design is in the prototype construction stage for eventual installation in the Japanese SCTF. Shown in Fig. 61, this probe design is based on a miniature TV camera, housed in a water-cooled annulus and positioned such that it is physically within the test vessel. Several features from earlier designs have been retained, most notably the xenon gas-filled annulus to reduce the heat loading from the facility to the probe. Where in past designs fiber optics light guides were used for lighting in the viewing region, the new design will use miniature lights mounted within the probe tip. The reduced lighting requirements are a direct result of eliminating the relay lens of the old design, which had poor light transmission characteristics. The new probe design also allows removal of the internals without affecting the pressure boundary. The current design will be a monocular unit, with the possibility of future probes reverting to the previous stereo design concept, depending on the feasibility of the data reduction methodology.

2. Upper Plenum De-entrainment Experiment

(J. C. Dallman, Q-8)

Measurements of the de-entrainment efficiency for a staggered multirow array of 101.6-mm-diam cylinders (with pitch-to-diameter

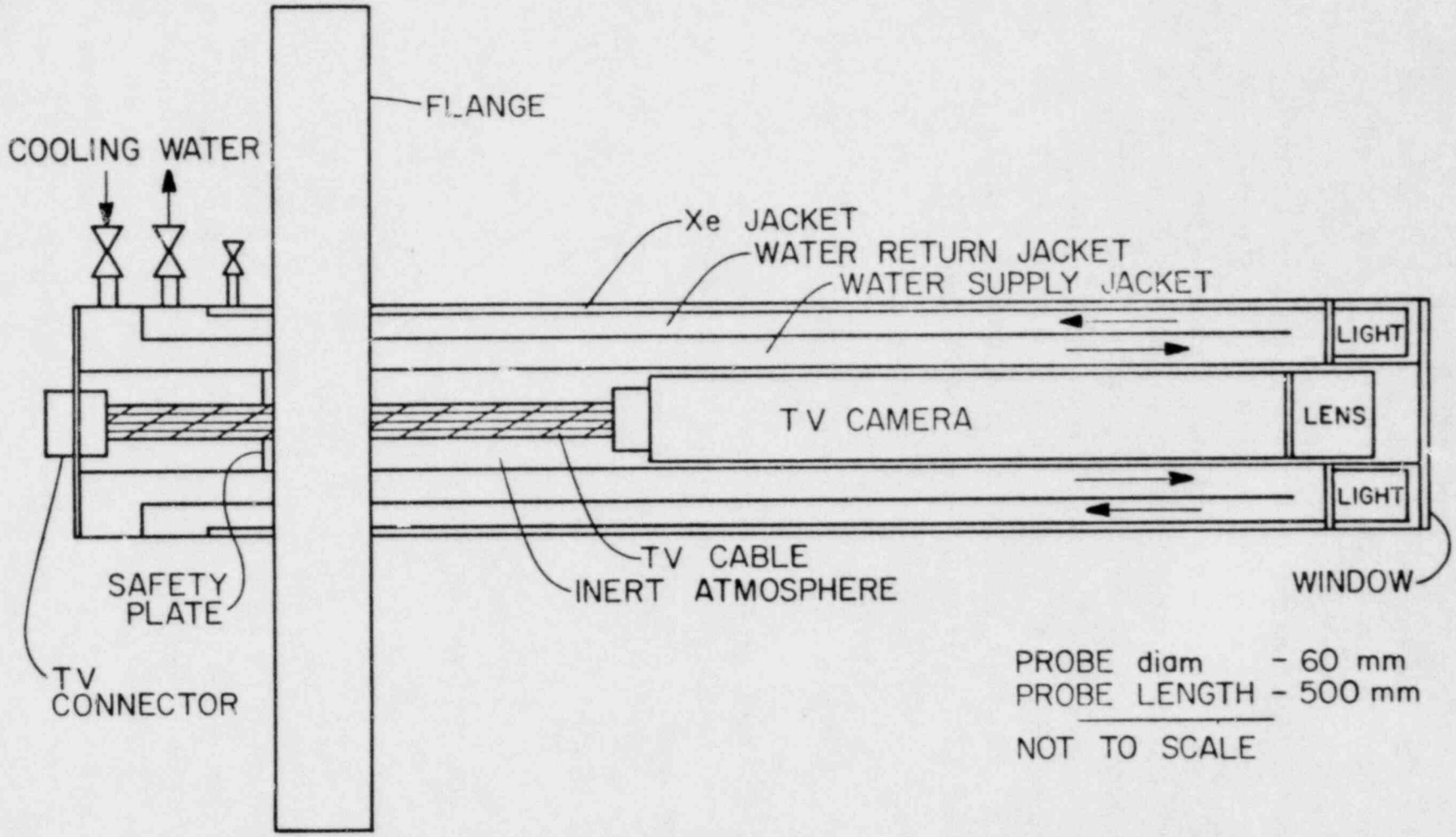

Fig. 61. SCTF video pro'e.

ratio of 1.25) have been completed for superficial air velocities of 7 and 14 m/s and average droplet mass flux rates from about 4 to 10 kg/m^2 s. These flow conditions are similar to those for which isolated structure de-entrainment measurements were made.[32]

In Fig. 62 droplet mass flux profiles at the same flow conditions are presented for three different arrays (all with the same cylinder size and pitch-to-diameter ratios but with differing numbers of rows intercepting the air-droplet cross flow). As the number of rows in the array is increased, the shape of the droplet profile changes from one peaked at the centerline to one that gradually increases from top to bottom.

Using the isolated cylinder de-entrainment measurements, a predictive equation for multirow arrays has been developed.[23] This equation has the form

$$\eta_{MR} = 1 - A(1-\eta_{R1})(1-\eta_{R2}) \ldots (1-\eta_{RN}) , \qquad (5)$$

where η_{RN} is the de-entrainment efficiency of a single cylinder in an array of cylinders. Chen[14] has developed a relationship for η_{RN} that has the form

$$\eta_{RN} = \eta_I(1 + 4.5\ \beta^2) . \qquad (6)$$

Here η_I is the isolated structure de-entrainment efficiency, which for the droplet mass flux rates of this study[32] is

$$\eta_I = 0.19 , \qquad (7)$$

and β is the pitch-to-diameter ratio of the array.

A comparison of the measured multirow array de-entrainment efficiency with the predictive Eqs. (5-7) is shown in Figs. 63 and 64. There is excellent agreement between the prediction and the measurements of multirow de-entrainment efficiency at the superficial air velocity of 14 m/s. However, at 7 m/s the predictive relation underpredicts the de-entrainment efficiency after the second row. This is probably because Eq. (5) ignores

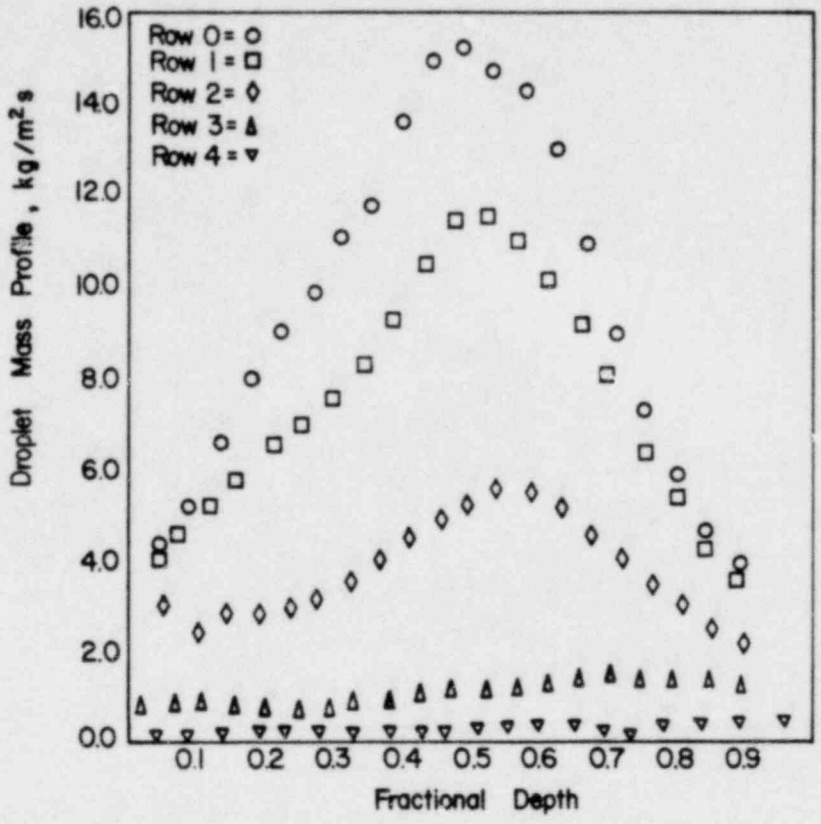

Fig. 62. Comparison of droplet mass flux profiles as additional rows of cylinders are added to the array for a 158 kg/min droplet flow rate and 7 m/s air velocity.

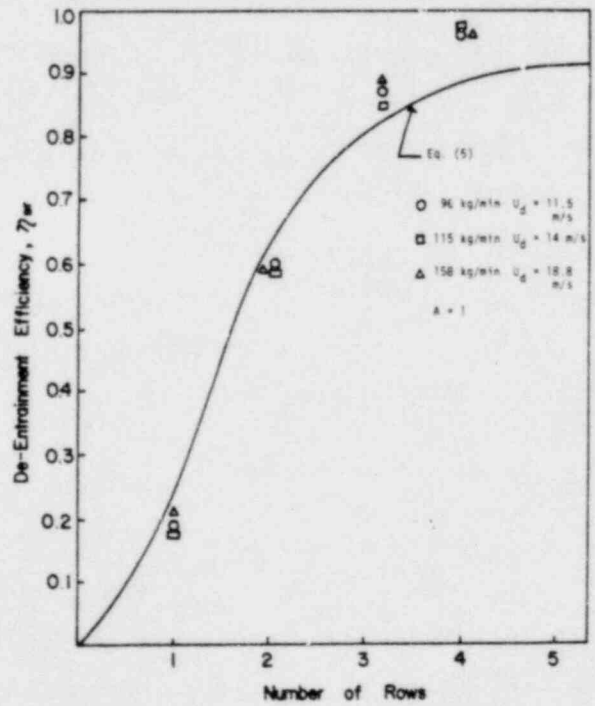

Fig. 63. Comparison of de-entrainment efficiency measurements at an air velocity of 14 m/s in a multirow array with Eq. (5).

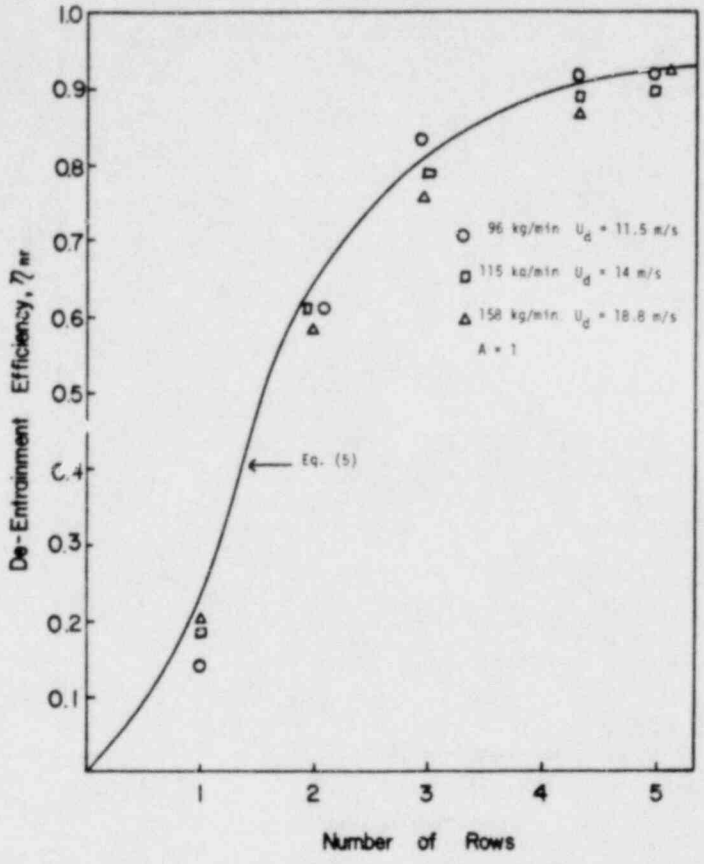

Fig. 64. Comparison of de-entrainment efficiency measurements at an air velocity of 7 m/s in a multirow array with Eq. (5).

both the free steam velocity and gravitational settling of the water droplets as they pass through the array. That gravity would more strongly affect the lower velocity measurements is to be expected and this remains a minor flaw in Eq. (5).

Designs are being prepared to upgrade the wind tunnel test area. This upgrading will include improvements for more accurate measurement at high air velocities (> 20 m/s) and the accommodation of different pitch-to-diameter ratios and smaller diameter cylinders.

F. LWR Multifault Accident Studies

(J. H. Scott and L. L. Smith, Q-7)

This section reports preliminary investigations of "multifault accidents" in LWRs; that is, those accidents that go beyond those normally analyzed, on a single failure criterion basis, in plant safety analysis

reports. Initial work to analyze damage to the TMI-2 reactor core is also reported in this section.

1. Delineation of Multifault Accidents in LWRs

(R. D. Burns, III, Q-7)

A catalog of types of multifault accidents in LWRs was developed to provide a structure for multifault accident analyses using TRAC and other methods as appropriate. Nine categories of anticipated accidents are included in the catalog based on WASH-1400,[33] Reports to Congress on Abnormal Occurrences,[34] the ACRS study of licensee event reports (LERs),[35] and ongoing LER studies.

Each category of multifault accidents will be studied for existing US reactors. Where the likelihood of a given accident is sufficiently low, that accident will not be studied in detail. The catalog includes

1. Station Blackout
2. Loss of Feedwater
3. Relief Valve LOCA
4. Spontaneous LOCA
5. Interfacing Systems LOCA
6. Decay Heat Removal Failure
7. Power Transient
8. Automatic Control System Failure
9. Sabotage.

The categories encompass a variety of possible operator responses, plant conditions, and additional equipment feailures. However, only high probability scenarios will be studied in detail. General descriptions of the multifault accident categories are included below.

Station blackout involves unavailability of off-site and on-site ac electrical power to the reactor plant. Loss of off-site ac power has occurred at many plants for numerous reasons. Normally, emergency diesel generators automatically supply emergency on-site ac power in

these situations. This is required for operation of ECC systems. Actual experience with diesel generators at nuclear power plants indicates that the diesels are not highly reliable, although redundancy has assured availability of emergency ac power in every case of loss of offsite power to date.

The scenario to be studied is the anticipated unavailability of emergency diesels. Should this occur, it is important that operators use relief and safety valves to cool the scrammed reactor while they attempt to restore emergency power. Possible complications include unavailability of dc battery power for operation of valves and instruments.

The issues involved in station blackout are

1. how should the relief valves be operated to maximize the time margin for recovering power,
2. how much time is available for power recovery, and
3. how is water inventory recovered after power recovery.

The probability of station blackout depends primarily on the redundancy of diesel generators, a factor that varies among plants. However, because of common-mode failures that have been observed for redundant diesel generator systems, the probability must be considered sufficiently high that this accident should be anticipated for most plants.

Loss of feedwater involves sudden loss of main feedwater and unavailability of auxiliary feedwater. Main-feedwater loss occurs about three times per year per reactor and normally requires operation of auxiliary feedwater to cool the scrammed reactor core. The accident at TMI-2 indicates that auxiliary feedwater may not always be available following main-feedwater loss.

A feedwater transient with auxiliary feedwater unavailability constitutes loss of secondary-side cooling in a PWR. The operators must recognize the situation and manually operate relief valves and regulate make-up flow while attempts are made to recover secondary-

side cooling. Possible complications include unavailability of ECC systems.

The issues involved in loss of feedwater include

1. how should the relief valves and make-up flow be regulated to remove decay heat and avoid a saturation condition in the primary system,

2. what is the margin of time for recovery of secondary-side cooling, and

3. how is stable shutdown reached after recovery.

While auxiliary feedwater was not available immediately during the TMI-2 accident, it was recovered soon enough to be of no significance in the accident sequence. However, this accident and the fact that WASH-1400 lists loss of feedwater as a dominant risk-contributing accident show that the likelihood is high enough that this should be anticipated in PWRs of current designs.

Relief Valve LOCA involves loss of primary coolant through stuck-open relief or safety valves. The TMI-2 accident and the Davis-Besse and Oconee-3 transients are examples of relief valve LOCAs. These valves are required to operate in feedwater transients if system pressure rises rapidly because of delayed auxiliary feedwater, delayed scram, or low setpoint. Normally, the loss of coolant can be controlled by block valves manually operated in series with the failed valves. Make-up flow or high-pressure safety injection is required to accommodate coolant loss through the open valves.

Scenarios to be studied are those where relief valves normally are required to operate in feedwater transients and those where they are not normally required but are forced open because of delayed auxiliary feedwater. The relief valve LOCA occurs when any relief or safety valve fails to close. Possible complications include inoperability of block valves in series with stuck-open valves and unavailability of high-pressure safety injection. A variation of the relief valve LOCA is inadvertent opening of a valve.

Issues involved in relief valve LOCAs are

1. can operators recognize relief valve LOCAs,
2. how should block valves be regulated,
3. how should make-up and high-pressure injection be regulated, and
4. how should the system be returned to a stable condition.

The TMI-2 accident and the Davis-Besse transient may have appeared to the operators as cases of inadvertent activation of high-pressure injection. This event has occurred at least 40 times in US reactors in the three-year period of 1976-1978 and requires manual throttling. At TMI-2, loss of coolant through the relief valve was not recognized for over 2 h.

Spontaneous LOCAs have been the subject of reactor accident research for many years. LOCAs involve spontaneous ruptures in the primary system pressure boundary. Unlike relief valve LOCAs, the loss of coolant is uncontrollable in spontaneous LOCAs. ECC systems are designed to respond automatically to spontaneous LOCAs.

Scenarios to be studied involve sudden pipe or valve rupture followed by reactor scram. Complications involve possible unavailability of various combinations of ECC systems.

Issues involved in spontaneous LOCAs are

1. the size and location of the break,
2. which safety equipment is required, and
3. what operator action is required.

WASH-1400 estimates that the probability of a spontaneous LOCA is greater than one per 1000 years per reactor for PWRs and BWRs. This probability is dominated by small-break LOCAs. Recently, a valve rupture on a Westinghouse PWR in Switzerland caused a small-break spontaneous LOCA. This type of accident must be anticipated in all US water reactors.

Interfacing systems LOCAs involve failure of closed valves separating the high-pressure primary vessel of a PWR from appended low-pressure systems such as the low-pressure safety injection system. This accident was found in WASH-1400 to dominate the accident risk in the Surry PWRs before a subsequent change in maintenance procedures decreased its probability. The result of failure of the closed valves is that the low-pressure system ruptures, providing a LOCA path for the primary system.

Possible scenarios involve any of several appended low-pressure systems in PWRs. Anticipated complications do not involve emergency system unavailability, unless directly associated with the failed low-pressure system.

Issues involved in interfacing systems LOCAs are

1. can the failed system be valved out to stop the loss of coolant,
2. is the failed system outside the containment building, and
3. which emergency functions are unavailable.

A combination of valve failures normally is required to cause an interfacing systems LOCA. However, common-mode failures caused by operator action, computer malfunction, or water hammer effects may be of sufficiently high probability that the accident must be anticipated in PWRs.

Decay heat removal failure involves unavailability of decay heat removal systems in the event of a reactor shutdown. This accident was found to dominate accident risk in the Peach Bottom BWRs studied in WASH-1[illegible] is accident can lead directly to overpressurization failure or containment. Decay heat removal failure can also happen in PWRs.

The scenarios to be analyzed involve transient-caused reactor scram followed by either pump or valve failure in the decay heat removal system. Operator action may be required to operate valves or recover pumps manually before the primary system overpressurizes,

forces open safety valves, and causes containment failure. Complications include possible failure of containment cooling functions, which can accelerate the containment overpressurization.

Issues involved in decay heat removal failure are

1. what is the likely cause of failure,
2. can operators recover the system,
3. how much time is available for operators to react, and
4. what alternate means of decay heat removal are available to the operators.

Decay heat removal systems are required for each shutdown of a reactor. Common-mode failures of valves or pumps because of human error or sensor malfunctions can render these systems unavailable when needed. The fact that cases of inadvertent valve and pump isolation have been observed in reactor systems indicates that decay heat removal failures must be anticipated for all reactors.

Power transients can result from improper control rod operation, poison oscillations, or improper boron concentration in the primary coolant. This can cause short-period power increases and possibly can lead to overheating of the core and subsequent primary system overpressurization.

Scenarios to be studied involve programmed rod withdrawal during startup, undetected separation of control rods from their drives, or malfunction of the primary water chemistry control system. Complications involve possible delays in reactor scram.

Issues involved in power transients are

1. what periods are likely to occur,
2. how much time is available for operators to terminate the transient, and
3. what is the nature of possible fuel damage.

At least 13 power transients resulting in periods shorter than 5 s occurred in US commercial reactors during the three-year period from 1976-1978. While none of these events led to significant fuel damage, they demonstrated that periods shorter than 5 s can occur. Power transients must be anticipated for all reactors.

Automatic control system failure can result from failure of electrical components and can cause numerous improper control actions. This type of failure can involve inadvertent isolation or activation of valves and pumps in the primary and power conversion systems of PWRs and BWRs. In automatic control system failures, positive operator action is required to control the reactor.

There are too many possible scenarios involving control systems failure to be enumerated here. For each reactor, the capability of the control system is unique. Considerations of these failures must be based on the possible actions of the particular system.

Issues in automatic control system failure involve

1. what does the system control,
2. what instruments and controls are available to operators for overriding the control system, and
3. what are the likely causes of control system failure.

Two cases of automatic control system failure have resulted from minor incidents involving personnel. The Browns Ferry fire was caused by a lit candle being used by a maintenance man. The Rancho Seco transient was caused by a small light bulb dropped by a maintenance man into an open control panel. The role of computers and automatic control is large in reactor control rooms and is expanding. Failure of these systems must be anticipated in all reactors because of their susceptibility to human-caused interruption.

Sabotage involves possible intentional actions by reactor personnel to cause various transient situations. This problem is similar to automatic control systems failure, except that different valves and pumps may be involved. Positive operator action may be required to control the reactor in the event of sabotage.

There are too many possible sabotage scenarios to enumerate here. Considerations of likely situations must be based on possible actions of a saboteur. Issues to be considered in sabotage include

1. what is a saboteur likely to be able to do and
2. what instruments and controls are ultimately available to the operator to secure the reactor.

The recent case of vandalism by two trainees at the Surry plant demonstrates the possibility of deliberate human acts which can damage plant systems. Such events must be anticipated for all reactors.

2. Analysis of Early Core Damage at Three Mile Island

(P. K. Mast and T. R. Wehner, Q-7; and J. R. Ireland, Q-6)

Core damage calculations have been performed for the first 3.5 h (the time including the first core uncovering) of the March 28, 1979 accident at the TMI-2. The specific phenomena considered include

1. cladding ballooning before rupture,
2. cladding rupture,
3. cladding oxidation including the effects of hydrogen evolution, cladding swelling, and cladding embrittlement,
4. possible cladding and fuel fragmentation, and
5. possible cladding and fuel melting.

The core response damage calculations for the first 11 050 s (3:04 h) of the accident were based on the primary system thermal-hydraulic response[36] obtained using TRAC.[5] Calculations of core response to 3.5 h, the time of the first reflood, were based on extrapolations[37] of these TRAC results, taking into account possible molten cladding relocation and hence, oxidation-heat-source relocation. The temperatures and system pressure used for the core-response damage calculations are shown in Figs. 65 and 66, respectively.

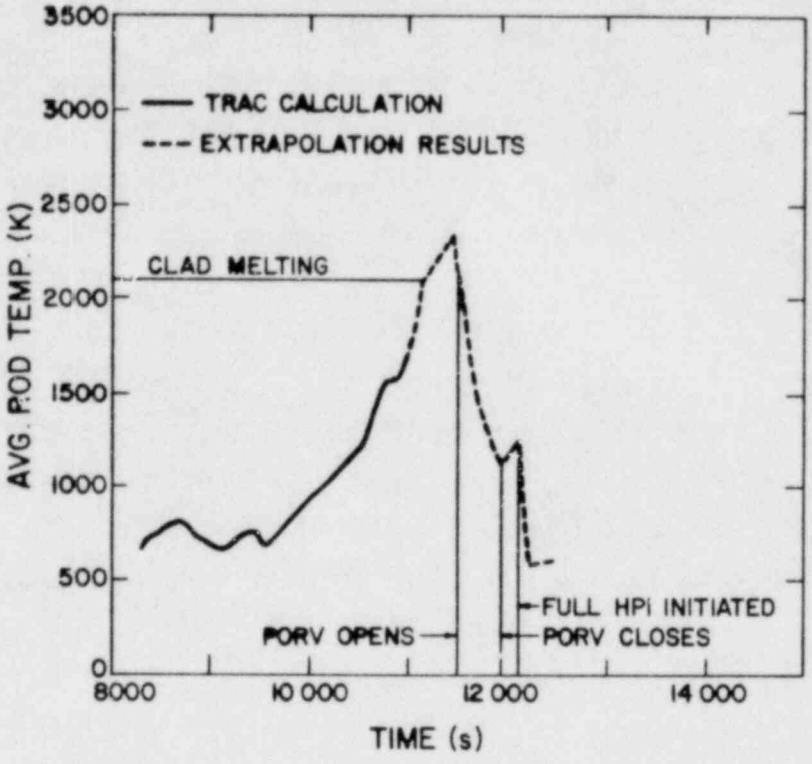

Fig. 65. Cladding temperatures used in TMI-2 core-damage calculations.

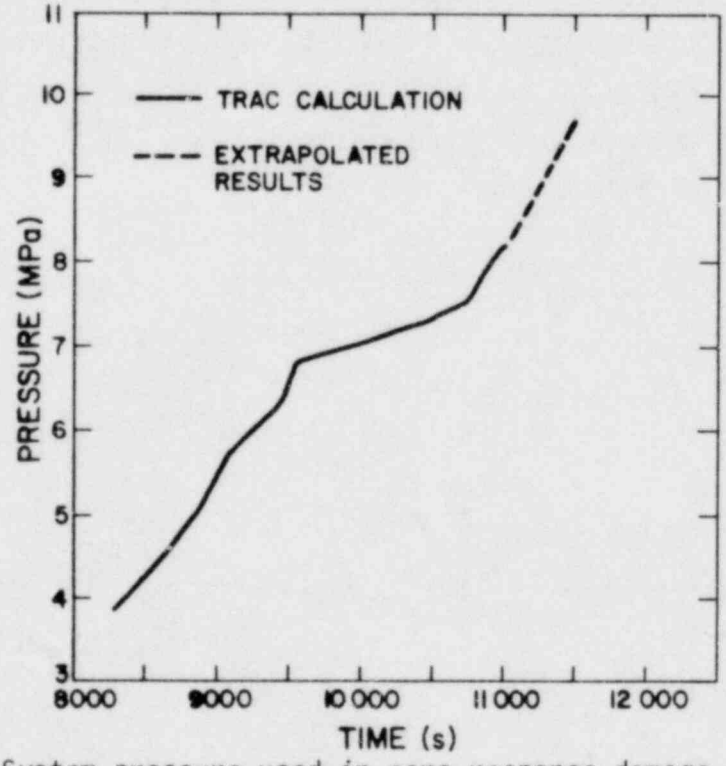

Fig. 66. System pressure used in core-response damage calculations.

a. Cladding Ballooning and Rupture

TMI-2 instrumentation data[38,39] and the TRAC analysis[36] both indicate excessive pin temperatures (Fig. 65) and below-normal operating system pressure (Fig. 66) during the accident. These conditions are likely to have led to cladding ballooning and rupture of the prepressurized fuel pins.

The time of fuel pin rupture during the TMI-2 accident was estimated from the calculated cladding hoop stress and the TRAC-calculated cladding temperature. Two independent failure criteria were used; the first was based on the failure-stress correlation given in MATPRO-11[13] and the other on a linear life-fraction-rule criterion[40] derived from an analysis of Chalk River Zircaloy stress-rupture data.[41]

The thin-cylindrical-shell stress equations were used to determine the cladding hoop stress as a function of the pin gas pressure (calculated using the ideal gas law) and the system pressure (obtained from TRAC analysis[36]). Because of uncertainties in the initial (steady state) gas pressure and in the pin internal void volume during the transient, the analysis was performed for initial (room temperature) pressures ranging from 2.5-4.2 MPa (3.0 MPa is the room temperature fill-gas pressure).[42]

The results of these analyses are shown in Table IV. Failure is calculated to occur at a fractional axial height of 0.85-1.00 at about 9 500 s (2:40 h). The uncertainty in the initial pressure leads to an uncertainty of ± 750 s (0:13 h) in the calculated failure time. Because of the coarse core nodalization used in the TRAC analysis, the radial variation in cladding failure time was calculated to be small. The calculated failure time is consistent with the observed sharp increase in radiation-monitor readings in the containment building dome at 9 300 s (2:35 h).[38,39]

The strain at failure was estimated using the failure-strain correction from MATPRO-11.[13] For a failure temperature of 1 000 K, this correlation predicts a total (uniform plus local) ballooning strain of 80%. Actually, rod-to-rod contact would occur at only 30% strain

TABLE IV

VARIATION IN PIN FAILURE TIME WITH INITIAL ROD PRESSURE

Initial Rod Pressure (MPa)	Failure Time			
	Peak Power Rod		Average Power Rod	
	(s)	(h)	(s)	(h)
2.5	9 237	(2:34)	10 230	(2:50)
3.0	8 840	(2:27)	9 195	(2:33)
3.5	8 679	(2:25)	8 872	(2:28)
4.0	8 614	(2:24)	8 743	(2:26)
4.2	8 582	(2:23)	8 711	(2:25)

calculated using the contact 1.3 square-pitch-to-diameter ratio in the TMI-2 assembly.

b. Cladding Oxidation: Hydrogen Evolution and Swelling

Oxidation of the Zircaloy cladding from the metal-steam reaction was calculated using the Cathcart isothermal parabolic rate equations from MATPRO-11.[13] Because of prolonged high cladding temperatures, these rate equations must be extrapolated beyond the time and temperature range of the available data.

Analysis of the axially dependent TRAC-calculated cladding temperatures indicates that substantial oxidation occurred at a fractional axial height of 0.6-0.9. The oxidation should not have been inhibited severely by steam depletion as indicated by the TRAC-calculated steam velocities. At the hottest axial location, the outer third of the cladding thickness is calculated to oxidize before the onset of cladding melting. This amount of oxidation would generate 130 kg of hydrogen (core-wide). For a typical TRAC-calculated upper plenum temperature of 1 200 K and pressure of 10 MPa, this mass of hydrogen would occupy about 65 m^3, which is equivalent to the volume of the vessel upper head plus part of the upper plenum. High thermocouple readings between 4 and 5 h into the accident indicate possible continued hydrogen generation.

Zircaloy undergoes a 50% volumetric expansion as it oxidizes. Because the inner part of the cladding was unoxidized and hence, unaffected by such swelling, the cladding outside diameter increased only 2%. Thus, the decrease in coolant-channel cross-sectional flow area caused by oxidation was insignificant, and the fuel-bundle coolability was affected only by cladding ballooning.

c. Possible Cladding and Fuel Disruption

Reflood by the high-pressure injection system at 12 000 s (3:20 h) following prolonged elevated core temperatures, may have induced cladding and fuel fragmentation. The likelihood of unoxidized cladding fragmentation was investigated by comparing the calculated cladding thermal stress with a temperature-dependent failure stress.[13] The maximum thermal-shock temperature drop across the cladding was estimated to be 120 K using Kantorovich profiles.[43] Using this value, the maximum circumferential stress was calculated to be 7.2 MPa, well below the failure stress of unoxidized Zircaloy at temperatures below 1 500 K.[37] Thus, fragmentation probably did not occur in the unoxidized cladding.

The Zircaloy oxidation reaction, however, causes the cladding to become very brittle. Experiments[44] indicate that the likelihood of thermal-stress-induced fragmentation increases following high-temperature oxidation. Comparison of these experimental results with the TRAC-calculated cladding thermal conditions indicates that the embrittled cladding over a 0.5 m length of the TMI-2 core may have fragmented. Thereafter, the bared hot fuel, even more brittle than the cladding, probably fragmented also.

The TRAC-calculated temperatures also indicated cladding melting, but not fuel melting. The overall calculated severe core disruption indicates that blockages developed, significantly affecting localized core cooling. This is consistent with the observed large core-wide variation of thermocouple readings at the core outlet at 4-5 h into the accident.[38,39]

These analyses indicate that extensive core damage occurred during the first uncovering of the core. Calculations based on temperatures extrapolated beyond the onset of core disruption are somewhat

speculative. However, the good agreement between the calculated core response and available instrumentation data gives confidence in this analysis.

III. LMFBR SAFETY RESEARCH

(M. G. Stevenson, Q-DO and J. H. Scott, Q-7)

The LMFBR safety research program at LASL consists of several efforts. The SIMMER code is being developed and applied to core disruptive accident (CDA) analysis with support from the Division of Reactor Safety Research (RSR) of NRC. SIMMER is a two-dimensional, coupled neutronics-fluid dynamics code intended for transition phase, core disassembly, and extended fuel-motion analysis. The second version of the code, SIMMER-II, is now being used in the analysis of CDA problems.

In a separate, but closely related, program funded by DOE models are being developed and verified for phenomena important to the progression and consequences of CDAs. Another part of this DOE program is focused on the application of the accident codes, particularly the SIMMER code, to the study of specific aspects of accident sequences. The work in the SIMMER code development and application area is reported in Sec. III.A.

Experimental investigation, including confirmation of reactor safety analysis methods, is an important part of safety research. Section III.B provides a summary of recent analytical and experimental work funded both by NRC/RSR and DOE to support SIMMER model development and testing.

A. SIMMER Code Development and Applications

(C. R. Bell and L. L. Smith, Q-7)

Reports on modifications to SAS3D for automated interfacing with SIMMER-II and an additional whole-core transition-phase analyses for the Clinch River Breeder Reactor (CRBR) are given in the following sections. A large effort is being made to analyze hypothetical core-disruption accident behavior in large heterogeneous breeder reactors. SAS3D data sets have been developed for loss-of-flow accidents (LOFAs) at three stages of core life (beginning-of-life, end-of-equilibrium cycle, and beginning-of-equilibrium cycle).

1. An Automated Interface from SAS3D to SIMMER-II

(R. G. Steinke and P. J. Hodson, Q-7)

The most appropriate physical models for simulating an entire LMFBR hypothetical core disruptive accident (HCDA) are provided through a combined use of the SAS3D and SIMMER-II computer programs. Each of these programs has models appropriate for a different portion of the accident; for example, during the initiating phase of the accident when the fabricated geometry is intact, the SAS3D models are more detailed and provide a more accurate simulation than SIMMER-II. The validity of the SAS3D models, however, breaks down when the geometry becomes disrupted because of melting and breakup. At this point, the spatial-neutronics and fluid-dynamics models of SIMMER-II are needed for a more realistic simulation of the events that follow.

To make a transition from SAS3D to SIMMER-II at the start of melting and breakup requires a data interface for transferring the reactor state. A convenient interface for this is the SIMMER-II input data format. When transferring the reactor state, considerable complications are introduced by having to transform the SAS3D internal/external channel reactor model to a SIMMER-II r-z geometry reactor model. This process has been done manually in the past using the channel parameters edited by SAS. Not all information is provided, resulting in the use of gross estimates for some quantities. A program module called SASSIM has been written for the SAS3D computer program to provide an automated interface from SAS3D to SIMMER-II. At user-specified problem times, SAS3D calls SASSIM to transform the SAS internal/external channel reactor state to r-z geometry. This transformation only involves fluid-dynamics state parameters. These include all material densities and temperatures, their vapor and liquid axial velocities, and hot dimensions. The many procedures and assumptions involved in making this geometry transformation have been documented[45] for user information and error appraisal. Having made the transformation to r-z geometry, SASSIM then edits these parameters in a format ready for

use as SIMMER-II input. SIMMER-II users need only supply additional information on exchange functions, equation of state, and neutronics models to continue the SAS3D analysis with SIMMER-II.

The linking of SIMMER-II to SAS3D is now an easier process although a high degree of user understanding and awareness must be exercised to prevent the unphysical mixing of SAS3D channels to r-z rings. Program module SASSIM has automated the data interface between these programs. Evaluating an HCDA now can be done efficiently using each program for the portion of the analysis where its models are appropriate.

2. Transition-Phase Calculations

(C. R. Bell, Q-7)

Two additional transition-phase calculations were performed based on the initial conditions[14] established for the CRBR homogeneous core. The first calculation was a repeat of the "blocked" boundary core[14] that terminated at about 5 s into the transition phase with a \$70/s reactivity insertion rate. In the present calculation, however, the transport neutronics treatment was employed instead of the diffusion treatment. The second calculation was identical to the first except that a modified lower axial blanket (LAB) was incorporated for the purpose of promoting early core penetration of the LAB. The second case also employed the transport neutronics treatment.

The comparison of the diffusion and transport treatments is complicated somewhat by a small change in the model for heat transfer between subassembly can walls. The power and reactivity for the transport and diffusion treatments are shown in Figs. 67 and 68, respectively. The first power peak in the transient is nearly the same for both treatments. The transport treatment leads to a more severe second peak, as expected, because of the more appropriate treatment of the large axial void that develops at 1.2 s following fuel-steel slumping. Because more energy is delivered to the system during the second burst, more melting occurs, more steel heatup results, and the subsequent transient behavior changes. A \$40/s burst occurs at 4.8 s leading to a two-dimensional disassembly that drives the system highly

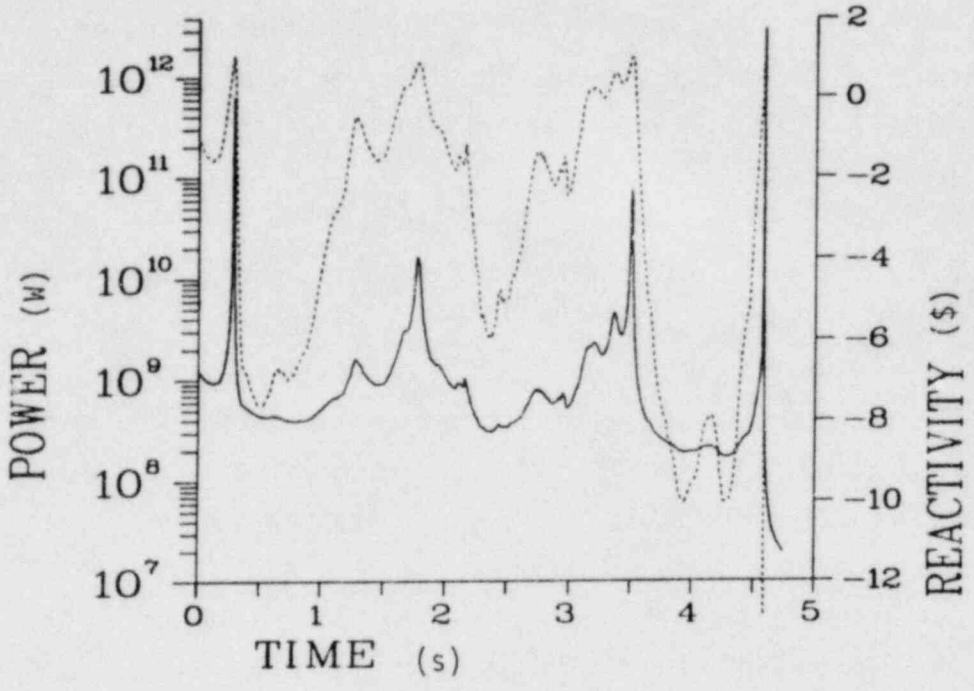

Fig. 67. Power and reactivity transients with diffusion neutronics.

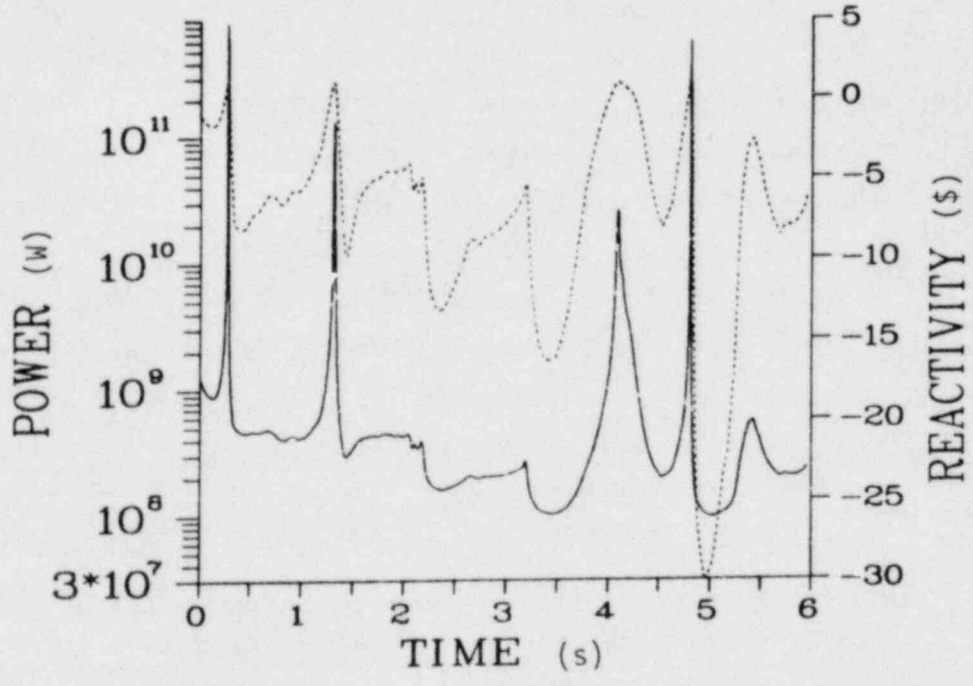

Fig. 68. Power and reactivity transients with transport neutronics.

subcritical. The molten core material again collects at the bottom of the active core region and brings the reactor back to the near-critical regime at a rapid rate of about $80/s. This ramp subsides before recriticality and does not produce a power burst. Subsequent movement of the molten pool gradually raises the reactivity state of the system to about +$0.5.

Several important points are evident from these results. First, there is a trend toward larger and more intensive reactivity swings as more subassembly cans are melted. This leads to greater two-dimensional involvement and coherency in the core motions both in a dispersive and compactive sense. Second, recriticalities will occur unless escape paths for core material or blanket entrainment can produce a large negative reactivity bias in the system. Third, the effects of bouyancy separation of fuel and steel and/or liquid and solid fuel are important to transition-phase development. The degree of stratification can change the reactivity state of the system by many dollars and therefore the requirements for fuel loss from the core region. Finally, the tendency for boilup appears to be dynamic instead of quasi-static; therefore, core sloshing is promoted instead of steady boilup during the time frame of these particular transients.

These analyses represent estimates of transition-phase behavior if fuel is prevented from easily escaping the active core region. Fuel engagement of the LAB is of critical importance if the types of recriticalities estimated in these analyses are to be avoided. The purpose of the second case with the modified LAB is to determine the effect of early penetration of core material into the LAB.

The LAB in the calculations was modified to provide open cavities into which the mobile core material could penetrate without involving the highly resistive, quenching characteristics of normal LAB pin structure. The length of the LAB was doubled to provide a continuous blanket region below the cavities. The cavities were placed in the upper half of the modified LAB as alternate rings of subassemblies. Thus, even though the cavities fill with core material, the reactivity is neutralized by the alternate rings of blanket material. The effect is the easy loss of fuel from the core.

The resulting reactivity and power behavior for this case are shown in Fig. 69 and can be compared to Fig. 68 because the same versions of SIMMER-II and the same initial conditions are used in both. Figure 69 shows the transient to be benign because of early LAB penetration. Also, it appears to be immune to the effects of material stratification because the neutronic state is so highly negative.

These two additional calculations of whole-core transition-phase behavior indicate a definite sensitivity to the neutronics treatment. The important reactivity insertion rates occur in the highly two-dimensional sloshing portion of the transient. Early escape of core material (control channels, radial and axial blanket penetration, or special design features such as the modified LAB) could prevent undesirable recriticalities during the transition phase.

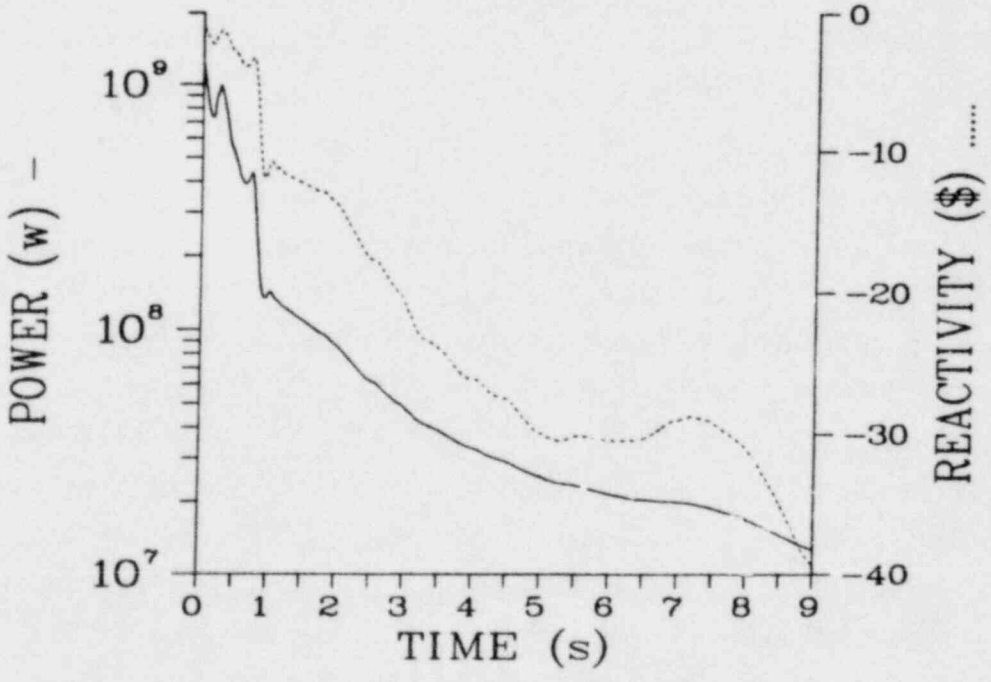

Fig. 69. Power and reactivity transients for the modified lower axial blanket.

B. Experiment Analysis and Planning

(J. H. Scott, Q-7)

During this quarter, the experiment analysis effort has been directed toward

1. development of models for experiment analysis and
2. analysis of SIMMER verification experiments.

In the first area, the LACOBRA model has been debugged and applied to the TREAT transient H6. Excellent agreement with the experiment is noted: this should enhance our ability to calculate in-reactor multipin experiments.

In the area of experiment analysis and performance, considerable emphasis has been placed on analysis of the Purdue-Omega experiments. An assessment of the prototypicality of fuel freezing and plugging simulant experiments has been made. Additionally, the last of the Phase I upper structure dynamics (USD) experiments has been performed.

1. LACOBRA Computer Code Analysis of the TREAT H6 TOP Test

(J. L. Tomkins, Q-7)

The TREAT TOP experiment H6[46] was performed to determine if fast test reactor (FTR) fuel ejected into coolant channels during a TOP-initiated HCDA would be removed permanently from the reactor core in sufficient quantity to cause a shutdown. Also, the H6 experimental results provide data for computer code development and verification.

The H6 experiment is typical of multipin TREAT experiments. The thermal neutron energy spectrum of the TREAT reactor results in large azimuthal and radial power gradients in the outer row of test bundle fuel pins. The azimuthal power gradients result in angular heat transfer within those pins and in circumferential variations in cladding and coolant temperature within the test bundle. Because of the azimuthal power variations in the H6 experiment, it provides appropriate data to test the LACOBRA[14] computer code and to demonstrate the

effect of angular conduction heat transfer on both fuel pin peak temperatures and on the cladding circumferential temperature gradient.

The H6 experiment bundle consists of seven PNL-10[47] FTR fuel pins in the Mark-IIC TREAT test loop. A cross section of the fuel pin bundle showing the hexagonal arrangement of fuel pins is presented in Fig. 70. As shown, the radial boundary is scalloped to simulate partially a row of fuel pins. Spacer wires are used to maintain pin-to-pin spacing and to enhance mixing between coolant channels. A complete description of the test bundle can be found in Ref. 70. Table V lists the flow channel areas and Table VI the fuel pin characteristics for the PNL-10 pins. A diagram of a PNL-10 pin is presented in Fig. 71.

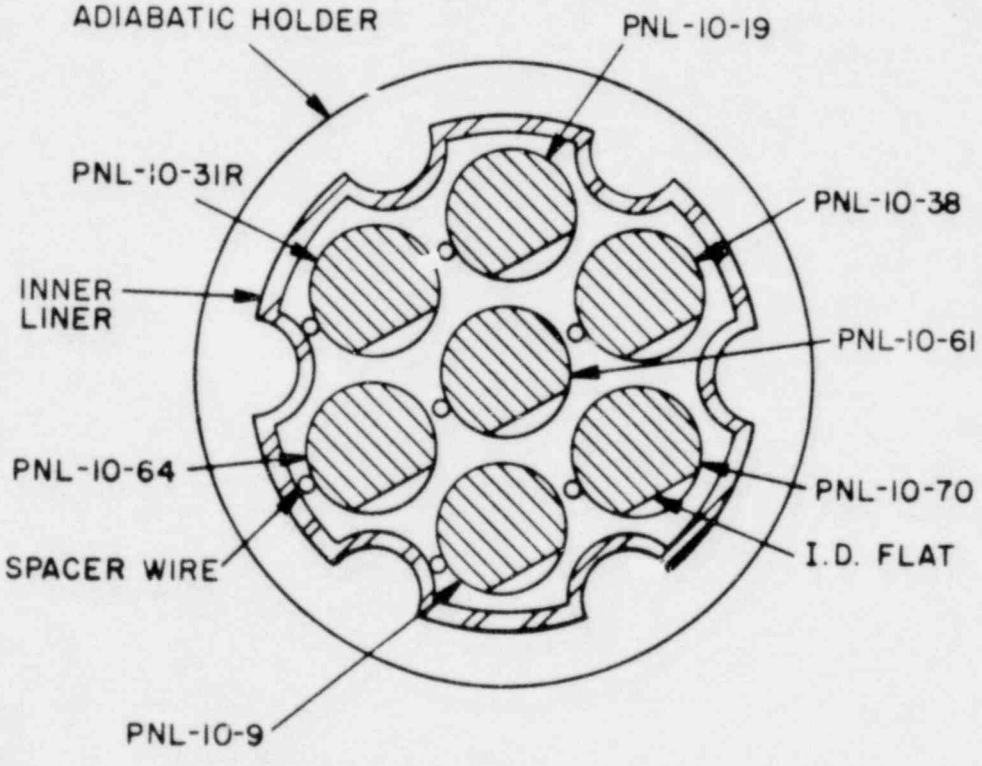

Fig. 70. Cross section of H6 fuel bundle.

TABLE V

COOLANT CHANNEL CHARACTERISTICS

	Pitch (m)	Nominal Flow Area (m^2)	Wetted Perimeter (m)	Heated Perimeter (m)
Inner row of coolant channels	7.2644×10^{-3}	8.352×10^{-6}	9.1766×10^{-3}	9.1766×10^{-3}
Second row of coolant channels	7.2644×10^{-3}	8.352×10^{-6}	9.1766×10^{-3}	6.1177×10^{-7}
Outer row of coolant channels	7.2644×10^{-3}	5.4376×10^{-6}	7.9462×10^{-3}	3.0589×10^{-3}

For the LACOBRA calculations the fuel pins were each divided into eight axial sections, corresponding to

1. bottom end plug,
2. lower reflector,
3. lower blanket,
4. active fuel,
5. upper blanket,
6. upper reflector,
7. fission gas plenum, and
8. top end plug.

The axial dimensions used in the calculations vary somewhat from the actual dimensions for all but the active fuel region because of a required constant axial mesh spacing in LACOBRA. Fuel pin axial regions above and below the active fuel region and the fluted bundle wall were included to account for heat sink and coolant mixing effects. The COBRA-IV[48] wire-wrap model, which is included in LACOBRA, was used to calculate forced cross flows and coolant channel area changes resulting

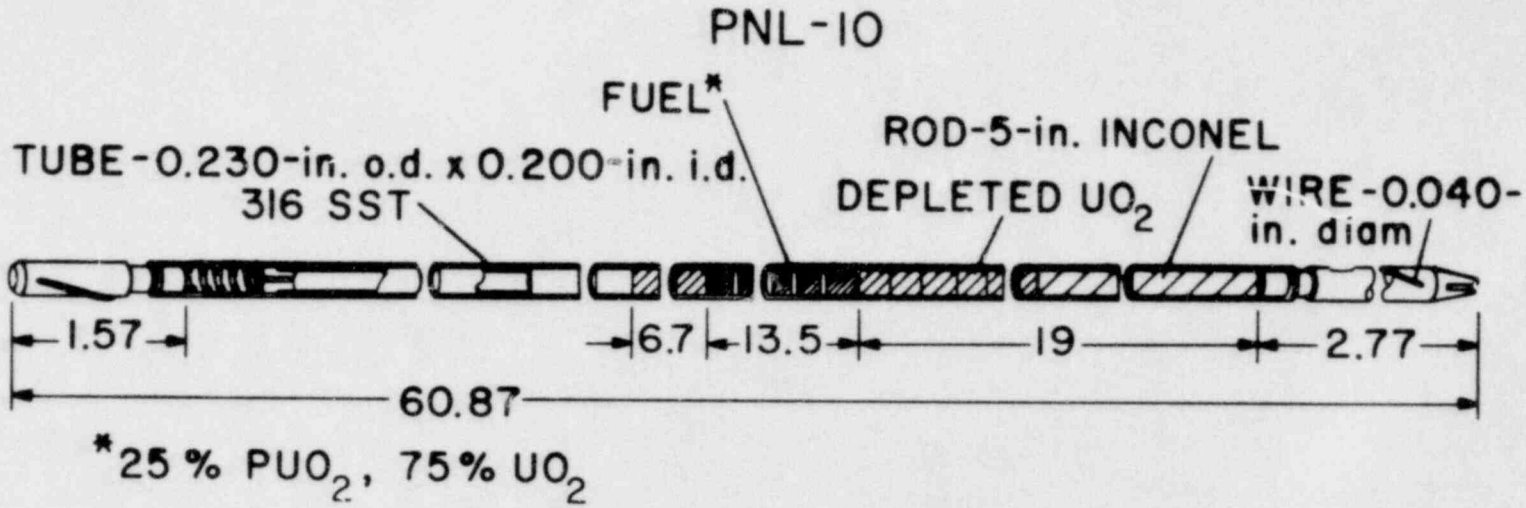

Fig. 71. PNL-10 pin configuration.

TABLE VI

FUEL PIN DESCRIPTION

	PNL-10	LACOBRA Model
Fuel material	$(0.25\ Pu + 0.75\ U)O_2$	$(0.25\ Pu + 0.75\ U)O_2$
Fuel pellet diameter (m)	4.928×10^{-3}	4.928×10^{-3}
Fuel column length (m)	3.429×10^{-1}	3.429×10^{-1}
Fuel pellet density (kg/m^3)	1.006×10^{4} (FE-79) 9.81×10^{3} (FE-92)	1.006×10^{4} (FE-79) 9.81×10^{3} (FE-92)
Fuel cladding diametral gap (m)	1.524×10^{-4}	1.524×10^{-4}
Blanket material	Natural UO_2	Natural UO_2
Blanket pellet diameter (m)	4.928×10^{-3}	4.928×10^{-3}
Lower blanket column length (m)	1.702×10^{-1}	1.524×10^{-1}
Upper blanket column length (m)	3.556×10^{-1}	3.810×10^{-1}
Blanket pellet density (kg/m^3)	9.972×10^{3}	9.972×10^{3}
Reflector material	Inconel 600 (odd pins) 20% CW 316 SS (even pins)	Inconel 600 (odd pins) 20% CW 316 SS (even pins)
Reflector diameter (m)	4.940×10^{-3}	4.940×10^{-3}
Lower reflector length (m)	1.270×10^{-1}	1.143×10^{-1}
Upper reflector length (m)	1.270×10^{-1}	1.524×10^{-1}
Reflector density (kg/m^3)	8.41×10^{3} (Inconel) 7.95×10^{3} (316 SS)	8.41×10^{3} (Inconel) 7.95×10^{3} (316 SS)

TABLE VI (cont)

	PNL-10	LACOBRA Model
Cladding material	20% CW 316 SS	20% CW 316 SS
Cladding o.d. (m)	5.842×10^{-3}	5.842×10^{-3}
Cladding i.d. (m)	5.880×10^{-3}	5.080×10^{-3}
Cladding density (kg/m^3)	7.95×10^{3}	7.95×10^{3}
Gas plenum fill gas	helium	none
Gas plenum column length (m)	3.132×10^{-1}	3.048×10^{-1}
Plenum spring	Inconel x 750 302 SS	none
End plug material	316 SS	316 SS
Lower plug length (m)	7.036×10^{-2}	3.81×10^{-2}
Upper plug length (mm)	3.988×10^{-2}	3.81×10^{-2}
Plug density (kg/m^3)	7.95×10^{3}	7.95×10^{3}
Total fuel pin column length (m)	1.546	1.524
Wire wrap material wire wrap pitch (m)	20% CW 316 SS 3.048×10^{-1}	20% CW 316 SS 3.048×10^{-1}
Wire wrap diameter (m)	1.02×10^{-3}	1.02×10^{-3}

from wire-wrap rotation. All material properties used in the LACOBRA calculations were taken from Ref. 49. Fuel pin power factors for radial, angular, and axial distributions are given in Fig. 72, Table VII, and Fig. 73, respectively. Power vs time for the TREAT reactor is shown in Fig. 74 and the test pin to TREAT reactor coupling factors are in Table VII.

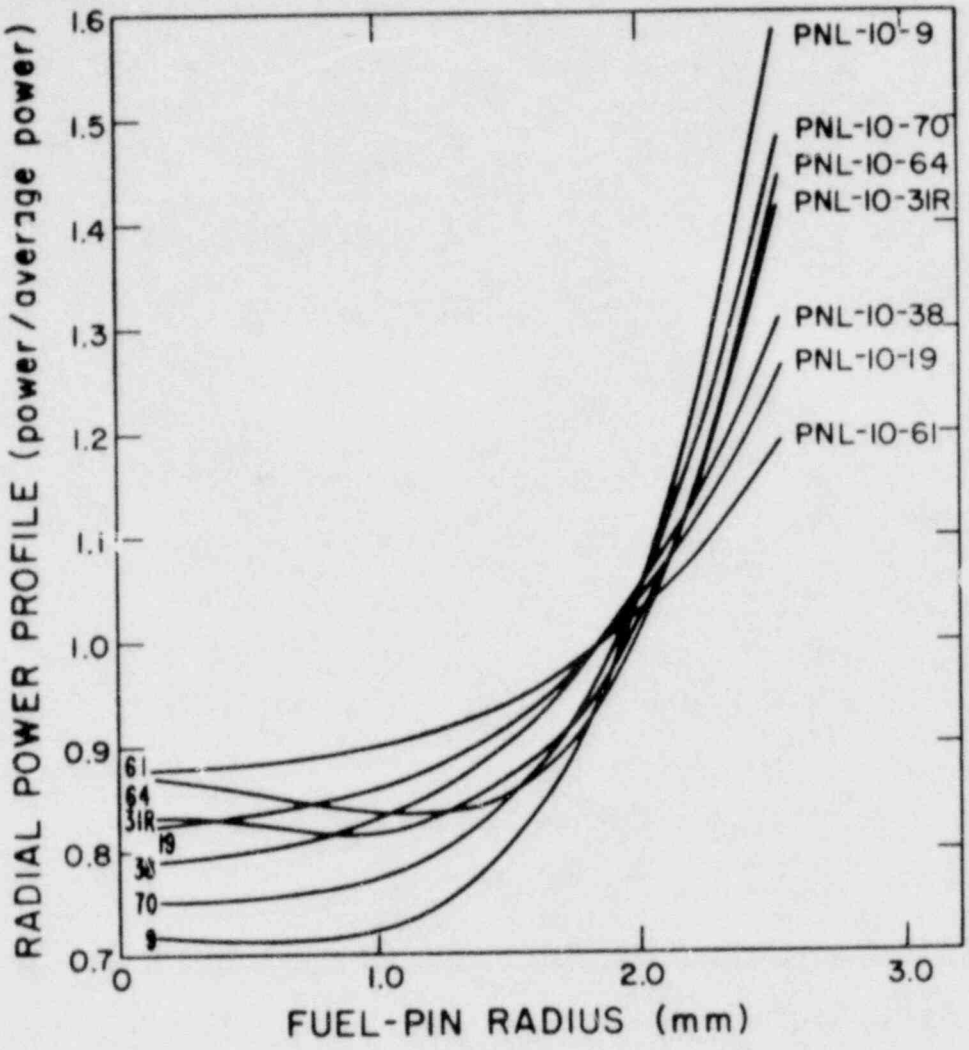

Fig. 72. Radial power profiles.

Temperature profiles from three LACOBRA calculations plus profiles from a COBRA-3M[50] calculation presented in Ref. 46 are given in Figs. 75a-d, respectively. Figure 75a shows the results from LACOBRA for fuel pins divided into six 60° angular sections with radial and angular heat conduction in the active fuel and cladding. Figure 75b gives LACOBRA results for fuel pins divided into six 60° angular sections wtih radial heat transfer only. Figure 75c results are for a LACOBRA calculation without angular divisions in the fuel pins and, therefore, with radial heat conduction only. The COBRA-3M calculation shown in Fig. 75d is presented to provide a direct comparison of the LACOBRA results shown in Fig. 75b. The two calculational models are essentially

TABLE VII

FUEL PIN POWER FACTORS

	Pin (J/kg MJ)	Angular Power Factors (Power/Average Power) 1	2	3	4	5	6
PNL-10-9	2.05×10^3	0.79	0.98	1.22	1.22	0.98	0.70
PNL-10-[illegible]	2.07×10^3	0.79	0.98	1.22	1.22	0.98	0.79
PNL-10-31R	1.94×10^3	0.79	0.98	1.22	1.22	0.98	0.79
PNL-10-19	1.95×10^3	0.79	0.98	1.22	1.22	0.98	0.79
PNL-10-38	1.96×10^3	0.79	0.98	1.22	1.22	0.98	0.79
PNL-10-70	2.03×10^3	0.79	0.98	1.22	1.22	0.98	0.79
PNL-10-61	1.63×10^3	1.0	1.0	1.0	1.0	1.0	1.0

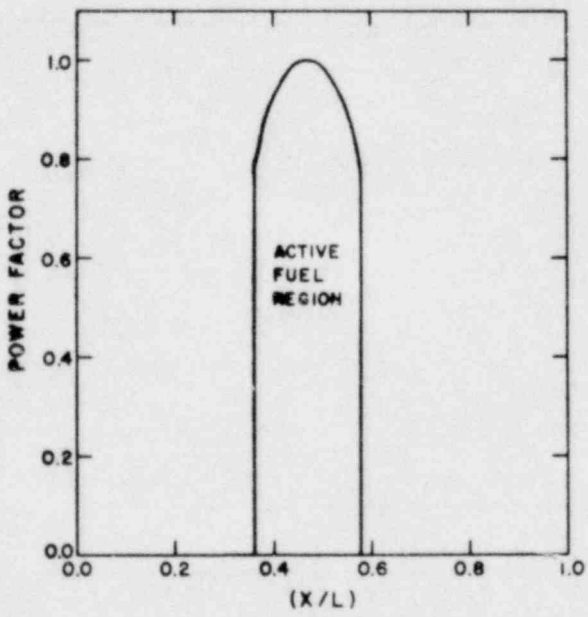

Fig. 73. Axial power factor as a function of distance from the bottom of the test bundle.

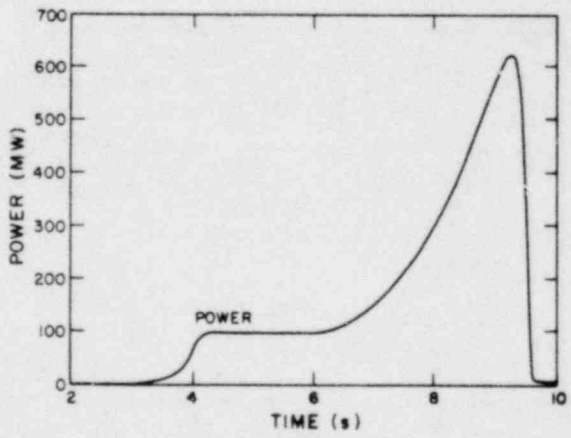

Fig. 74. TREAT power vs time.

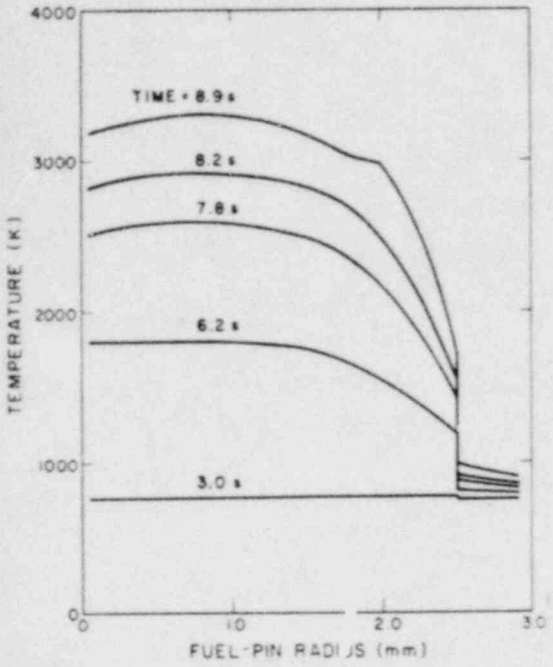

(a)

Fig. 75. Radial temperature profiles of typical peripheral fuel pin at axial midplane.

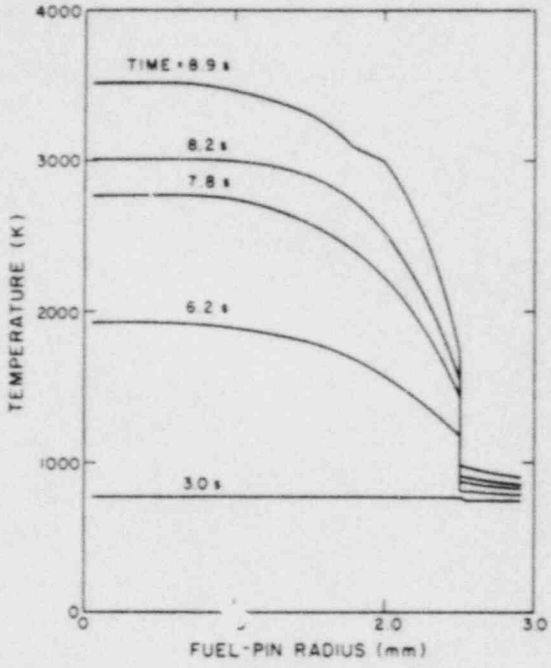

(b)

Fig. 75. LACOBRA calculation of H6, 60° pin sections, radial conduction only.

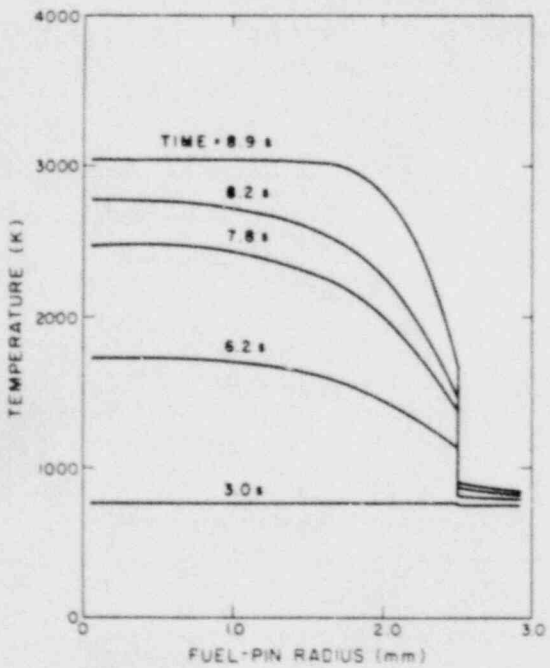

(c)

Fig. 75. LACOBRA calculation of H6, 1-3 60° pin section radial conduction only.

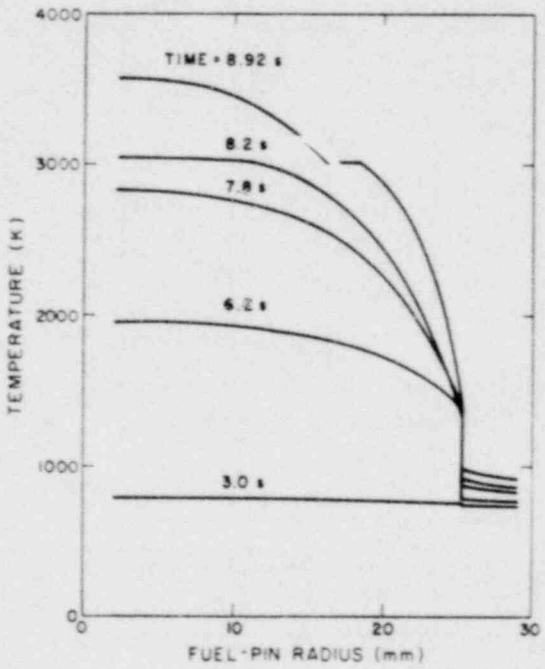

(d)

Fig. 75. COBRA-3M calculation presented on p. 42 of Ref. 46.

the same except for small differences in material properties and in the fuel pellet-to-cladding gap conduction models used. The results are in substantial agreement.

A comparison of Fig. 75a and 75b shows a substantial reduction in peak fuel pin temperatures when angular conduction is included. However, the effective angular averaging in the calculation shown in Fig. 75c results in the lowest peak fuel temperatures. These results indicate that in fuel pins with large azimuthal power variations, neglecting angular conduction probably leads to incorrect fuel peak temperatures and incorrect melt fractions.

Figures 76a-c show cladding and surrounding coolant channel temperatures for each of the three LACOBRA calculations (Figs. 76a-c correspond directly to Figs. 75a-c). A comparison of these results shows that cladding temperatures vary circumferentially around the pin by more than 20 K in 76a and 76b and that the difference in the temperature gradient is about 5K. The approximately 20 K cladding temperature gradient is reduced from what would be expected for uniform coolant temperatures surrounding the fuel pin because the maximum power and temperature pin segments are bounded by coolant channels with temperatures less than the average.

Three main conclusions about the analysis of TREAT experiment H6 with LACOBRA have been reached.

1. Angular conduction is important for the calculation of accurate peak fuel temperatures.

2. An azimuthally averaged fuel pin represents a poor approximation to an angularly divided one when significant azimuthal power gradients exist.

3. LACOBRA can calculate fuel pin heat transfer for detailed geometries such as the TREAT H6 experiment.

Finally, these results indicate that accurate analysis of multipin TREAT tests requires detailed fuel pin thermal and coolant thermal-hydraulics models such as those found in the LACOBRA computer code.

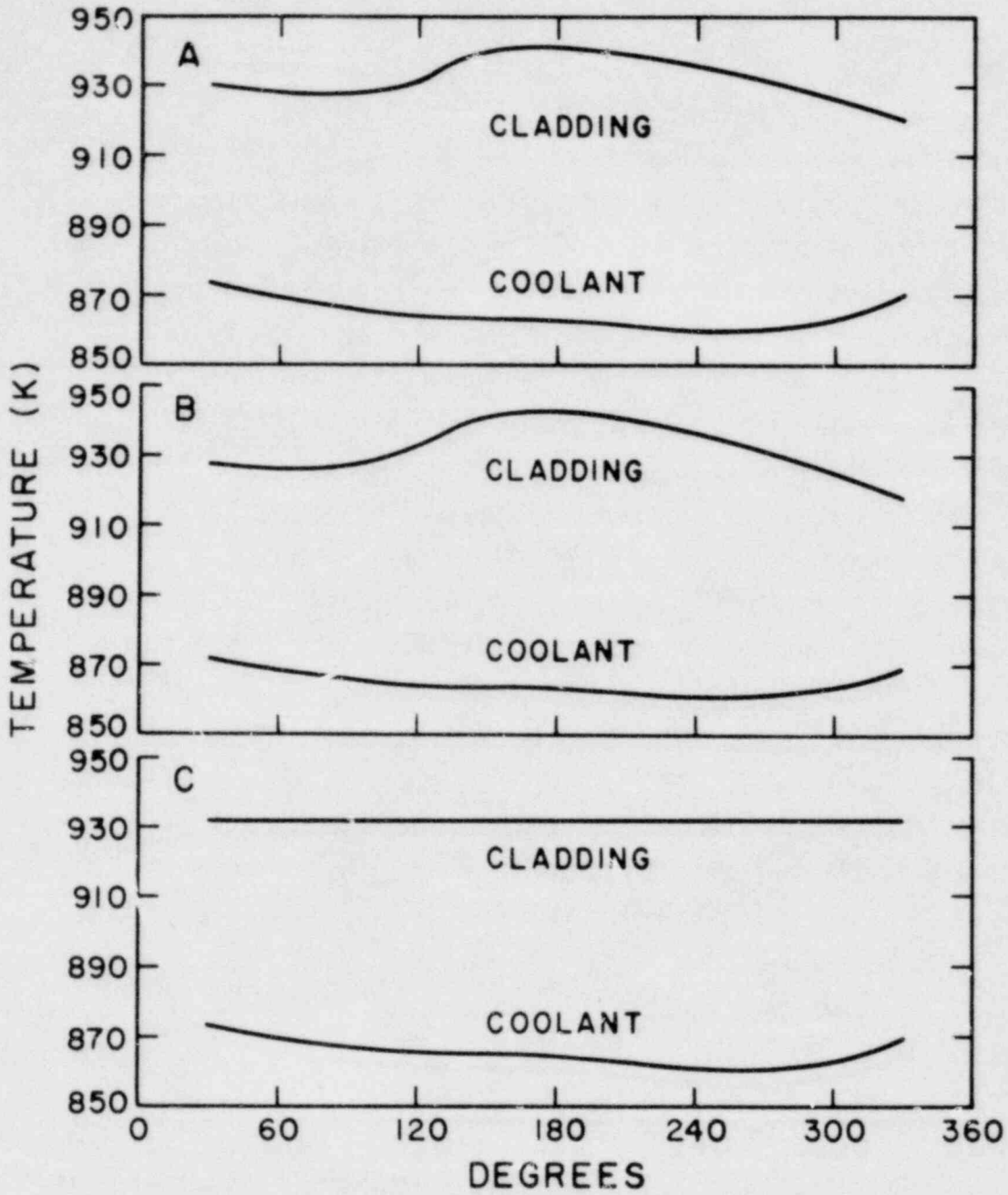

Fig. 76a. Coolant and cladding temperatures at 8.9 s, 60° section fuel pins, radial and angular conduction. Average peripheral pin at axial midplane.

Fig. 76b. Coolant and cladding temperatures at 8.9 s, 60° section fuel pins, radial conduction only. Average peripheral pin at axial midplane.

Fig. 76c. Coolant and cladding temperatures at 8.9 s, 360° section fuel pins, radial conduction only. Average peripheral pin at axial midplane.

2. SIMMER Analysis of the Purdue-Omega Experiments

(A. J. Suo-Anttila, Q-7)

Part of the SIMMER verification program includes the analysis of several Purdue-Omega experiments. These are similar to experiments performed at SRI International except that the scale is much larger -- that is, 1/7 CRBR in the Purdue experiments vs 1/30 CRBR in the SRI International series. The complete description of the apparatus and experimental program has been reported elsewhere.[51]

The Purdue experimental program consists of a series of nitrogen gas and hot flashing water blowdowns into an acrylic vessel. The hot flashing water blowdowns include nonvolatile (water) and volatile (methanol MeOH)[51] pool effects. No results have been reported for the volatile pool experiments at this time. However, SIMMER pretest predictions have been performed.

The first series of Omega experiments analyzed with SIMMER was the high-pressure nitrogen blowdowns. Table VIII shows the excellent agreement between the predicted time of peak pressure (impact) at the top of the vessel and the experimental times.

The magnitude of the pressure peak predicted by SIMMER is considerably higher than that measured experimentally. This discrepancy has been traced to rapid phase transition in the cover gas. In the experiment, the cover gas rapidly decelerates the upward moving water slug. This dynamically unstable situation results in the growth of Taylor instabilities, which eventually leads to a froth at the time of head impact; the froth greatly enhances the surface area for evaporation of the cool water into the warmer, highly compressed cover gas. The evaporation causes the cover gas compression to be more nearly isothermal rather than isentropic as in the SIMMER "no phase transition" calculation. If phase transitions are allowed in the SIMMER calculation, the predicted pressures can be "tuned" to match exactly the experimental pressures by varying the bubble sizes in the cover gas cells.

The agreement between the experimental and predicted head impact times is quite good for both the Purdue-Omega N_2 experiments and the SRI-N_2 experiments and no code modifications were necessary; thus the

TABLE VIII

PURDUE NITROGEN EXPANSION EXPERIMENTS

Source Pressure Mpa (psi)	Experiment Impact Time[a] (ms, ± 1 ms)	SIMMER-II Impact Time[b] (ms)
0.68 (100)	23.5	23.91
1.36 (200)	16.0	16.82
2.04 (300)	13.5	13.94

[a]Nitrogen expansion experiment with 1.9-cm-thick vacuum holder 4.32-cm cover gas gap.

[b]SIMMER-II was an "off the shelf" no-phase-transition version.

purely fluid dynamic effects appear to be modeled adequately with SIMMER in the limit of pure gases and liquids for CRBR scaled geometries. The only variable in these problems is the mesh structure. In general, the finer the mesh, the more accurate the answer. For the Purdue and SRI-N_2 experiment analysis, mesh structures were used of approximately 10-20 radial cells and 30-50 axial cells. Coarser mesh structures result in unacceptably poor comparisons with experiment. Finer mesh structures increase computing time considerably with negligible gains in accuracy.

The results of two Purdue-Omega flashing water experiments have been reported.[51] A SIMMER simulation of these experiments results in a considerable discrepancy in the head impact time for the Omega IV-6 (300 psi) experiment as shown in Table IX. The problem has been traced to unusual critical two-phase flow conditions and the inadequacy of the current SIMMER droplet-radii models to simulate such conditions. Because this situation is caused by modeling omissions, it is not possible to tune the input such that the experimental data and the SIMMER predictions overlap.

SIMMER has calculated near equilibrium, two-phase choking in other situations with acceptable accuracy. The present situation is

TABLE IX

PURDUE FLASHING WATER EXPERIMENT

Description	Impact Time
IV-6 300-psi experiment	~75 ms
SIMMER off-the-shelf	
RPMIN - 10^{-6} m	20.6 ms
RPMIN - 10^{-5} m	20.7 ms
RPMIN - 10^{-4} m	21.0 ms

rather unusual because the exit flow area is very large compared to the volume of material blowing down. In fact, the area/volume ratios for this experiment have not been achieved in any other blowdown experiments.[52] The result of this large area/volume ratio is a highly nonequilibrium critical-flow condition.

The discrepancy between the predicted and measured impact time was overcome by implementing a number density flow-regime model. Briefly, the number density model used is as follows.

1. Define the initial number density of bubbles or droplets in each mesh cell through input data, $N = N_o\ (r, z, t = o)$.

2. During the transient calculation, adjust the number density according to the liquid (droplet) or vapor (bubble) velocity by solving

$$\frac{dN}{dt} = U \cdot \nabla N \ ,$$

where U = vapor velocity if vapor volume fraction < liquid volume fraction or the liquid velocity if liquid volume fraction < vapor volume fraction.

3. Solve for the bubble or droplet radii at each time step by using

$$r_p = \left(\frac{3\alpha_G}{4\pi N}\right)^{1/3} \quad \text{if } \alpha_G < \alpha_L \ , \ \alpha = \text{volume fraction},$$

$$r_p = \left(\frac{3\alpha_L}{4\pi N}\right)^{1/3} \quad \text{if } \alpha_G > \alpha_L \ .$$

In Figs. 77 and 78 predicted head impact times are compared with the initial number density, N_o, for the Purdue-Omega experiments IV-6 and IV-12 (both 300-psi sources). The most important aspect of these figures is the overlap of SIMMER predictions and the experimental measurements. Because head impact time provides a measure of the critical-flow rate, a small amount of nonequilibrium leads to a greater critical-flow rate than would be expected in an equilibrium (large number-density limit) blowdown. Also, a minimum exists in the impact time. This is expected because by decreasing number density, the resistance to phase change is increased until a state must be reached where vapor cannot be produced at a sufficient rate to drive the expansion. Finally, the experimental impact time and the minimum coincide. The reason for this is not clear and possibly could be coincidental. Analysis of other experiments using different materials and pressures could resolve this last point.

Other experiments being performed in the Omega series include complete blowdown (evacuation of the source region) and two-component (volatile pool) experiments. The complete blowdown analyses are being performed as well as the two-component H_2O - MeOH experiments. Preliminary results for the two-component experiments indicate impact times of about 25 ms for a driving source of 1.5 MPa (200 psi) saturated water into a room-temperature methanol pool. However, experimental results are not available yet for comparisons.

3. Scaling Analysis for Simulant-Material Fuel Freezing and Plugging Tests

(E. J. Chapyak, Q-7)

Recent SIMMER calculations of transition-phase phenomena have shown the importance of fuel blockage formation on transition-phase evolution. These results suggest that the position and extent of fuel blockages formed in the early transition phase largely determine the sequencing and severity of recriticality events that occur later

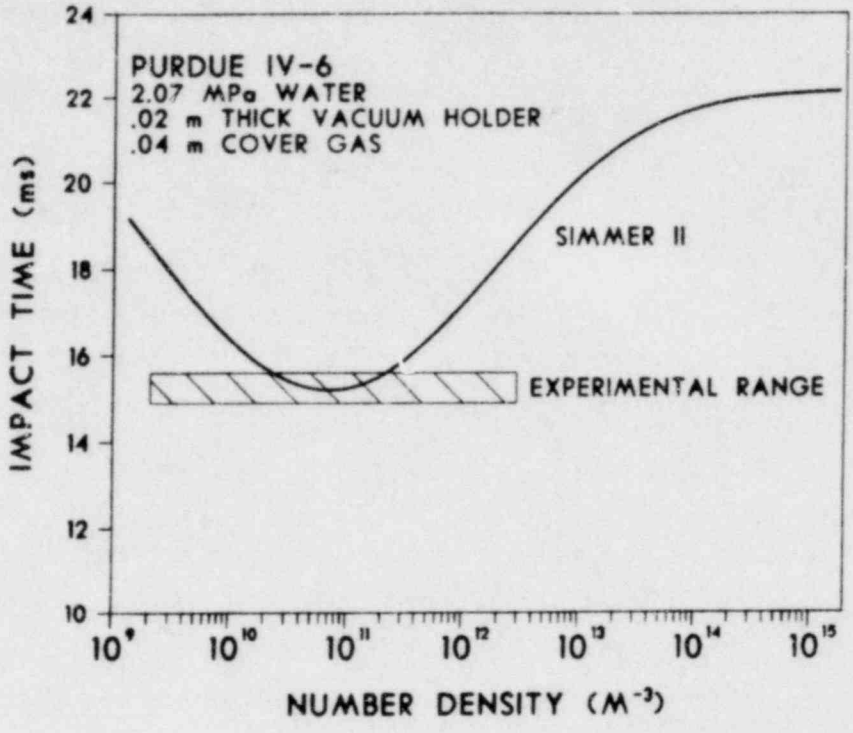

Fig. 77. Initial number density vs impact time for the Purdue IV-6 experiment.

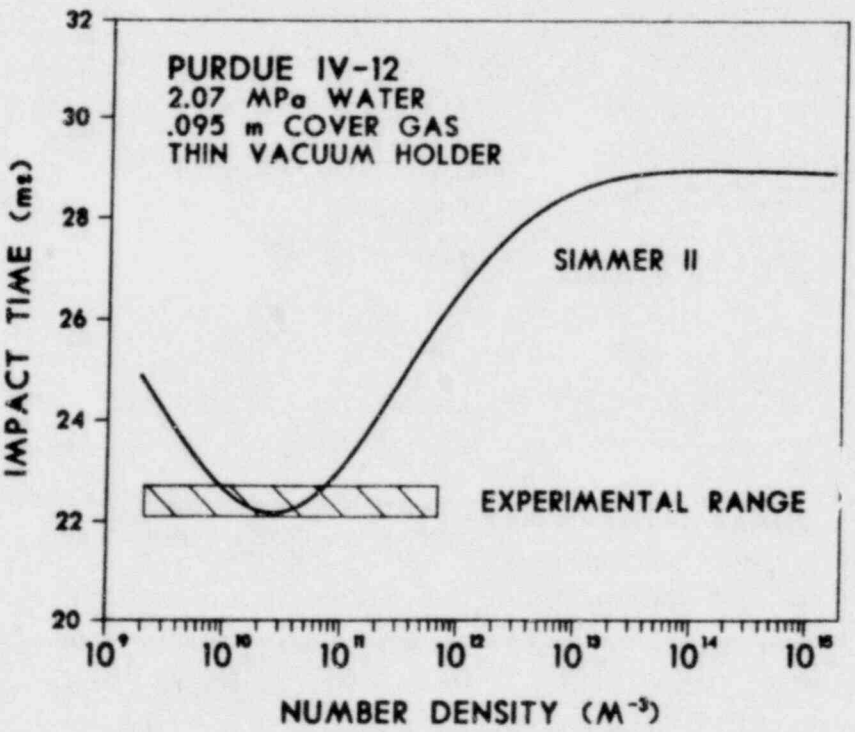

Fig. 78. Initial number density vs impact time for the Purdue IV-12 experiment.

in the accident sequence. Although considerable effort has been devoted to understanding fuel freezing phenomenology, including both real and simulant material experimental programs and model development, large discrepancies remain in the predictions by the various models of fuel blockage penetration distances.[53] Consequently, we have performed a preliminary scaling analysis for fuel freezing and plugging simulant-material experiments to investigate the prototypicality of previous experiments and models derived from them. This analysis not only pinpoints many of the potential problems associated with such tests but also suggests promising approaches for fuel-freezing experiment design.

Table X presents the dimensionless groups appropriate for freezing and plugging simulant-material tests. These parameters were derived from Ref. 54, with the additional assumption that compressibility effects can be neglected in these relatively low-speed, low void-fraction flows. In addition, fuel crust structural properties (appropriate if stable fuel crusts form) have been ignored.

The scaling requirements presented in Table X can be used to assess the prototypicality of simulant materials used in freezing and plugging experiments. For example, Sandia Laboratories in Albuquerque (SLA) recently have performed ice pipe experiments in which ice was employed as the steel simulant and Freon-11 was used to simulate molten fuel.[52] Comparing the water entries in Table X to the ideal (prototypic) values, we see that water's surface tension and thermal conductivity are too low to achieve prototypicality as a steel simulant. Also, the required initial temperature difference between the steel simulant (water) and its associated fuel simulant is quite high (290 K) -- a temperature difference over an order of magnitude larger than was actually employed in the SLA experiments. These observations suggest that the speed of propagation of the melt front in the ice and the amount of ice melted (i.e., thickness of layer) were too small in the ice pipe experiments to approach prototypicality. Consequently, even the qualitative nature of flow phenomena observed in these experiments (for example, steel entrainment) could be quite different from that in prototypic situations.

TABLE X

DIMENSIONLESS GROUPS FOR FREEZING AND PLUGGING

	Group	Description	Ideal Value (Steel)	Simulant Value				Steel Simulant
				H_2O	Li	Ether	CS_2	
1.	$g^{1/3}\ell/\nu_s^{2/3}$	Steel Reynolds number (sets length scale)	$\ell = \ell_p$	$\ell = 1.45\ell_p$	$\ell = 1.4\ell_p$	$\ell = 0.67\ell_p$	$\ell = 0.67\ell_p$	
2.	$\Delta P/\rho_s g\ell$	Pressure ratio (sets pressure drop)	$P = P_p$	$P = 0.2\ P_p$	$P = 0.1\ P_p$	$P = 0.7\ P_p$	$P = 0.12\ P_p$	
3.	$\rho_s^{1/3}\sigma_s/g^{1/3}\mu_s^{4/3}$	Dimensionless surface tension	2.4×10^4	3.3×10^3	3.8×10^4	4.9×10^3	6.3×10^3	
4.	$\mu_s C_s/k_s$	Steel Prandtl number	0.15	6.9	0.05	3.8	2.3	
5.	$C_s\Delta T/L_{fs}$	Ratio of internal-to-latent energies (sets $\Delta T = T_{mf} - T_{ms}$)	3.7 (ΔT= 1300 K)	ΔT=290 K T_i=560 K	ΔT=380 K T_i=800 K	ΔT= 160 K T_i=320 K	ΔT=210 K T_i=370 K	
6.	$(\Delta T/\rho_s)d\rho_s/dT$	Nondimensional thermal expansion						
7.	$\Delta\rho_{sm}/\rho_s$	Nondimensional expansion on melting	UO_2	R-11		R-113	R114B2	UO_2 simulant
8.	k_s/k_f	Ratio of thermal conductivities	7	6.5		1	1.6	
9.	C_s/C_f	Ratio of heat capacities	1.5	4.8		2.4	1.4	
10.	ρ_s/ρ_f	0.7	0.67		0.51	0.8		
11.	ν_s/ν_f	Ratio of viscosities	1.0	3.6		0.4	0.6	
12.	σ_s/σ_f	Ratio of surface tensions	3.8	3.9		1	1	
13.	σ_s/σ_{sf}	Ratio of surface tensions						
14.	L_{fs}/L_{ff}	Ratio of latent heats	1.0	N/A		0.3	N/A	
15.	$\frac{d\rho_s/dT}{d\ell_f/dT}$	Ratio of thermal expansivities						
16.	$\Delta\rho_{sm}/\Delta\rho_{fm}$	Ratio of expansions on melting						

Thus, we believe that water is not a good steel simulant. A potentially better approach would be to select a cryogenic steel simulant such as ether or carbon disulfide (see Table X), where the required driving temperature differences, although still considerable, only require a fuel simulant injection temperature slightly above ambient. Another advantage with cryogenic steel simulants is that fuel freezing can be simulated with suitable fuel simulants such as Freon-13. The best situation occurs when a liquid metal, such as lithium, is employed as the steel simulant. This is the only way heat-transfer processes in the steel can be duplicated correctly. Here, however, the difficulty lies in finding a compatible fuel simulant.

We are continuing to investigate these and other approaches to design useful simulant-material fuel freezing tests and to review available freezing and plugging data and the fuel penetration models derived from such data. This effort will be used to improve SIMMER modeling of fuel freezing phenomena.

4. Upper Structure Dynamics Experiment

(E. J. Chapyak, Q-7; V. S. Starkovich, Q-8; and D. Wilhelm, KfK)

a. Experimental Results

During this quarter, Phase I of the USD experimental program ended with the successful completion of four tests using Freon-113 as the simulant fluid. Phase-I tests were designed primarily to exercise basic experimental design and instrumentation recording capabilities. The first USD test was performed in February 1979 and was reported in a previous report.[23]

USD tests 2 and 3 were performed in September and October 1979. Results from these tests indicated that the base Kulite pressure transducers were performing unsatisfactorily. Subsequent testing suggested that the anomalous readings were probably due to transient thermal effects modifying gauge calibrations. A transducer mounting design change and the application of RTV (an elastic, thermally insulating polymer) to the transducer sensing element appeared to solve this problem.

USD tests 4 and 5, performed in November 1979, provided the first reliable quantitative data from the program. Test 4 was carried out at an initial core pressure of 0.67 MPa and temperature of 390 K. The initial pressure in the upper core structure (UCS) and view chamber was 20 mm of mercury, while the initial temperature was 293 K. Test 5 had similar initial conditions to test 4, except for the presence of a 0.28-kg aluminum piston directly above the UCS. The piston was intended to model inertial effects of the sodium pool above the UCS in prototypic situations. In both tests we employed a total of five pressure transducers located at the core bottom, the spacer region directly above the rupture disk, and at the lower, middle, and upper UCS. Thermocouples were placed at the same locations, except for the spacer region. Those in the UCS were brought to within 1 mm of one of the seven 1.28-cm-diam holes in the aluminum, equivalent-flow-area UCS. Test 5 also had three Bentley-Nevada displacement transducers to trace piston motion through the view chamber.

One of the most interesting observations that can be made with these results concerns the relative effect of the piston. Figure 79 compares the pressure records at the middle UCS station for both tests. For the first 4 ms into the test, the records appear almost identical. Then the reflected pressure wave from the piston (apparently moving at a speed of about 100 m/s) quickly dominates the trace for test 5. Figure 80 shows the Bentley-Nevada transducer records for test 5. Knowing the piston length (10.1 cm) allows us to estimate piston velocities from these data. Velocities appear to be approximately 18 m/s in the lower view chamber (corresponding to an initial acceleration of about 200 g's), 38 m/s at the middle of the view chamber, and 42 m/s at the top of the view chamber. Piston impact also can be seen in Fig. 81, which is the core pressure record for test 5. The noisy signal at about 0.036 s apparently was caused by "ringing" of the experimental structure from piston impact. This ringing also may have caused anomalously low-pressure signals to be observed from the transducer in the upper UCS. Figure 82 shows the middle UCS temperature record in test 5 in the middle UCS. The approximately 0.2-s delay between initial disturbance and thermal response is consistent

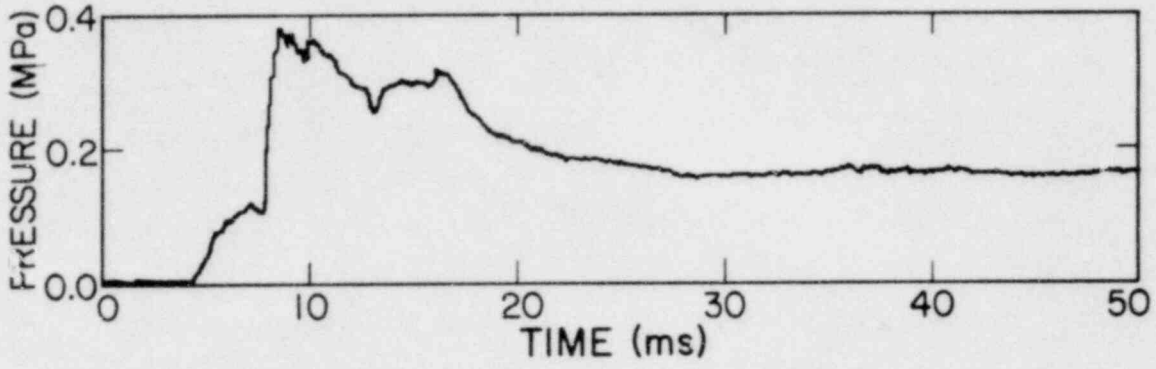

Fig. 79a. Mid-UCS pressure for test 5.

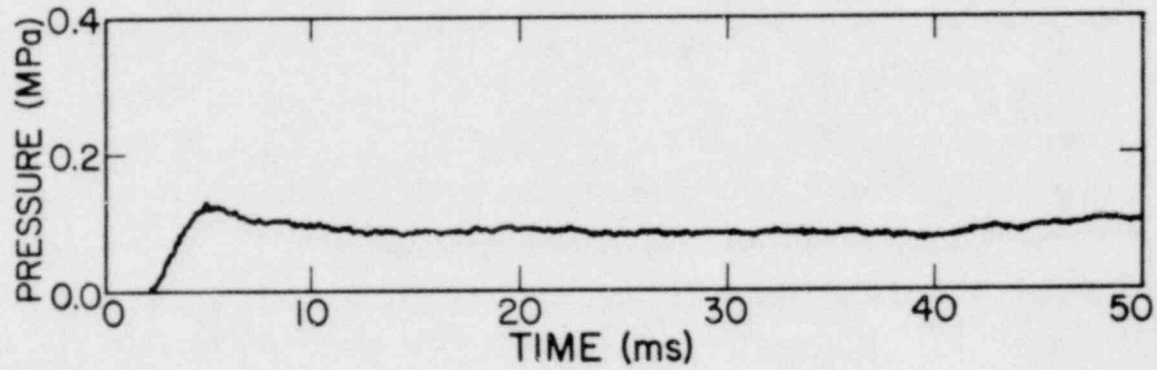

Fig. 79b. Mid-UCS pressure for test 4.

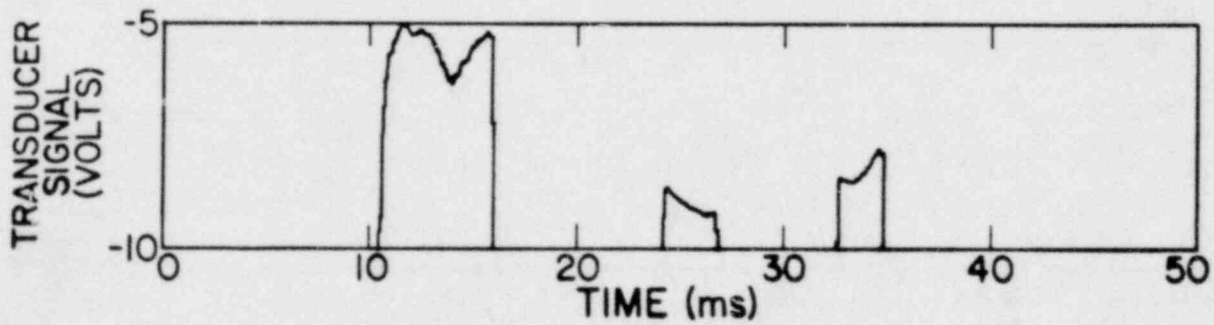

Fig. 80. Bentley-Nevada transducer signals for test 5.

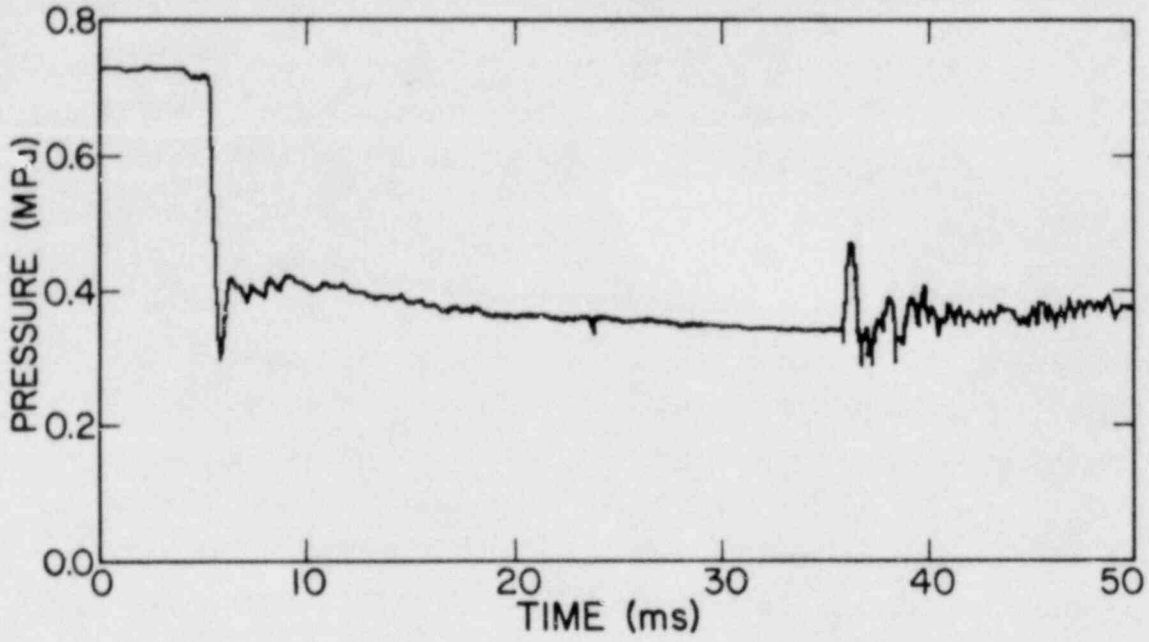

Fig. 81. Core pressure for test 5.

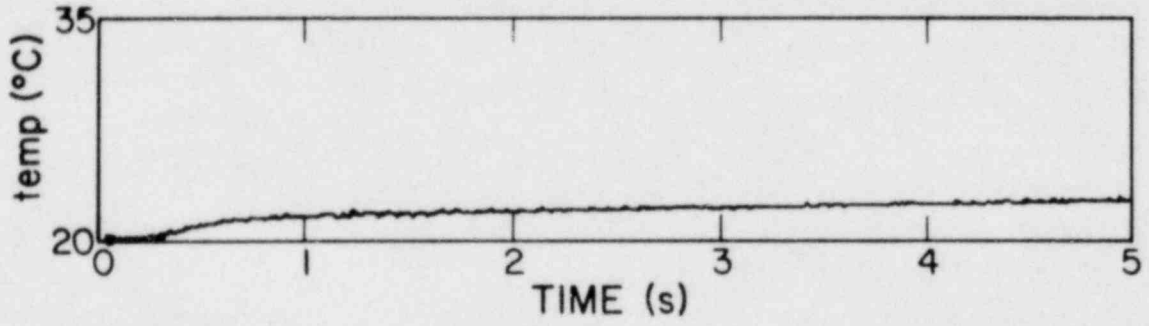

Fig. 82. Mid-UCS temperature for test 5.

with the arrival of the diffusional temperature wave through about 1 mm of aluminum.

Phase II of the USD program will begin with the construction of a new view chamber to accommodate the n-propyl alcohol simulant. In addition, a better shock absorber for the piston is being designed and will be built soon. The test program will resume as soon as these modifications are completed. SIMMER analyses for the tests described above are in progress.

b. Design Considerations

In the USD experiment, the upper sodium pool is simulated by a solid piston. The piston simulates the movement of the interface (between the HCDA bubble emerging from the UCS or UIS) and the sodium pool. The piston has been chosen because it is an appropriate device for modeling the one-dimensional movement of the interface adjacent. It also provides a convenient way of tracing interfacial velocity. The purpose of the following calculation is to derive a design criterion for the USD view chamber.

Without the UIS, the bubble emerging from the UCS has a roughly spherical shape. Further, the SIMMER results show that we can assume a coherent, uniform movement of the upper pool interface toward the vessel head. Thus, the top of the bubble will expand in the axial direction a much longer distance than the flat sodium pool/cover gas interface (see Fig. 83). By comparing the bubble volume and the cover-gas volume we derive the maximum axial distance z that the bubble interface travels in the axial direction by

$$z = 2r - h ,$$

where r is the bubble radius with the bubble center already emerged from the UCS exit plane and h is the height of that part of the bubble that hypothetically still is hidden in the UCS. When we assign a as the height and D the diameter of the cylindrical cover-gas volume and the sodium pool, we have

$$\frac{1}{4}\pi D^2 a = \frac{4}{3}\pi r^3 - \frac{1}{3}\pi h^2 (3r - h), \text{ with } h \leq r. \qquad (8)$$

To simplify calculations, the bubble surface always is supposed to coincide with the upper end of the core periphery. With this assumption only minor effects of the bubble growth in the vicinity of the radial blanket are neglected. Thus,

$$2rh - h^2 = \frac{1}{4} c^2 , \qquad (9)$$

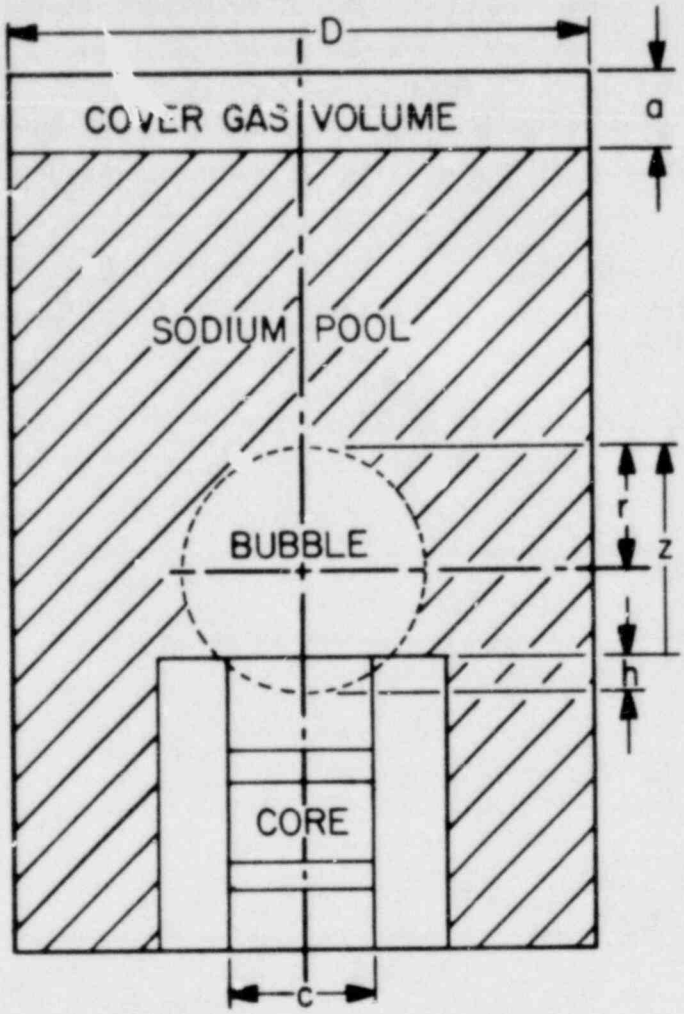

Fig. 83. Model of the HCDA bubble emerging from the UCS (no UIS).

where c is the diameter of the cylindrical periphery of the core. By assuming $h \leq r$ we obtain

$$h = r - \sqrt{r^2 - \frac{1}{4} c^2} \quad . \tag{10}$$

Combination of this formula with the volume-equation yields r as a function of D, C, and a such that

$$\frac{2}{3} r^3 + \left(\frac{2}{3} r^2 + \frac{1}{12} c^2\right) \sqrt{r^2 - \frac{1}{4} c^2} \quad - \frac{1}{4} D^2 a = 0 \; . \tag{11}$$

If we take D = 6 m, c = 2 m, and a = 0.5 m, the radius of the bubble will be r = 1.27 m and z = 2.04 m. Thus, the spherical bubble can emerge into the sodium pool and develop to a maximum height that is approximately four times higher than the displacement of the upper surface of the pool. Because length scales in the USD experiment are reduced to 40% of prototypic lengths, this result implies that a piston flight distance of 0.82 m would be necessary to model the anticipated maximum displacement of the sodium pool.

IV. HTGR SAFETY RESEARCH PROGRAM

(M. G. Stevenson, Q-DO)

Under the sponsorship of the NRC/PNA, LASL is conducting a program of research in High-Temperature Gas-Cooled Reactor (HTGR) safety technology in the following task areas.

- Structure Evaluation
- Phenomena Modeling, Systems Analysis, and Accident Delineation

Progress for this quarter in these two areas is reported below.

A. Structural Investigations

(C. A. Anderson, Q-13)

Activity in this program during the past quarter has been in three different areas:

1. core support block (CSB) thermal stress analyses,*
2. heavy water reactor (HWR) seismic analysis and
3. analysis of prestressed concrete reactor vessels (PCRVs).

In the first task, two- and three-dimensional finite element models of a Fort St. Vrain CSB have been developed and subjected to thermal loadings that have been specified for a Firewater Cooldown (FWCD) accident. Resulting thermal stresses have been significantly greater than stresses produced by the dead weight of the core itself, but have not exceeded the minimum ultimate tensile strength of the graphite structural material for all cases examined to date. In the HWR seismic work, relevant documents were reviewed and specific problems have been identified. Finally, work has been initiated on converting

---

*Mainly supported by a Technical Assistance Contract to the Division of Project Management, NRR.

NONSAP-C to the CRAY computer to allow us to handle large three-dimensional creep analyses of PCRVs.

1. Core Support Block Thermal Stress Analysis

(T. A. Butler, L. M. Carruthers, C. R. Wiig, and C. A. Anderson, Q-13)

Concern has been raised as to the thermal stresses induced in Fort St. Vrain graphite core components caused by the nonuniform core temperatures predicted during a FWCD accident. In the FWCD accident, total loss of forced circulation occurs during a 90-min period before partial (about 2%) forced circulation capability is restored. Figure 84 illustrates the 37 active region average temperatures at station 8 (top of the CSB) of the Fort St. Vrain reactor at 200 min into the accident. The data have been taken from ORECA calculations of the FWCD accident carried out by Sid Ball at ORNL. As much as 1500°F difference -- region to region -- was observed in these calculations.

To get an estimate of thermal stresses in the core, a 19-node, 6-element, two-dimensional finite element thermal model of each region was constructed as shown in Fig. 85a. A fully quadratic temperature field in each of the 6-node triangles was assumed. Nodal temperatures then were calculated by solving the two-dimensional steady-state heat equation with constant internal heat generation (simulating a uniform flux perpendicular to the plane of interest) by Galerkin's method. Coupling to the six adjacent regions at their various temperatures was by conduction across a helium gap. The internal heat generation was adjusted to give the correct (as specified from the ORECA calculation) average block temperature. The resulting temperatures then were used to calculate thermal stresses from the refined mesh shown in Fig. 85b. Here a plane version of the TSAAS code[55] was used, which allows for the specification of a temperature-dependent thermal expansion coefficient for CSB graphite. With these simple models about 3 s of CDC-7600 time was required for each analysis, which allowed for inexpensive parametric studies.

Some typical results are shown in Figs. 86 and 87 and Figs. 88 and 89 for the cases of a hot (2 000°F) block surrounded by six cold (500 °F)

1000 1033

999 903 531 1115 1916 1052

1030 1039 663 2008 946 556 1003

1014 673 773 1936 1778 1558 570 1006

1018 1269 1397 1980 957 774 510 1562 1034

1052 1864 760 569 664 1084 1676 1049

1025 870 662 828 1915 690 1014

1007 1029 496 1677 1718 1039

997 1048

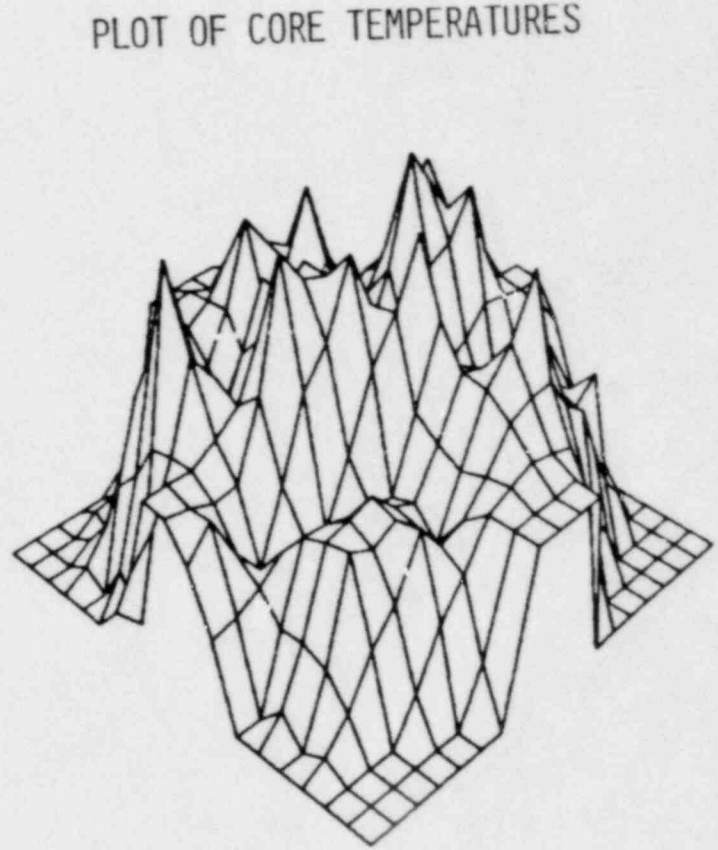

Fig. 84. Temperature (°F) at axial station 8 and 200 min into the FWCD accident.

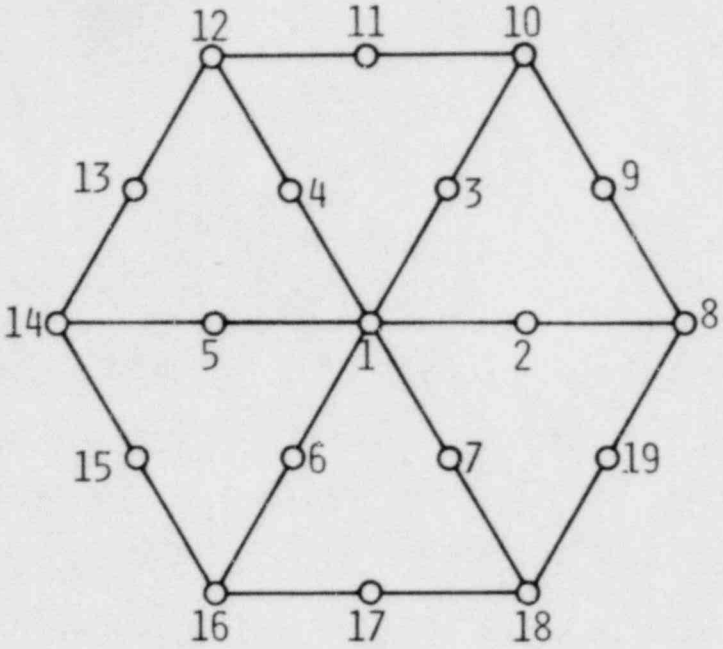

(a)

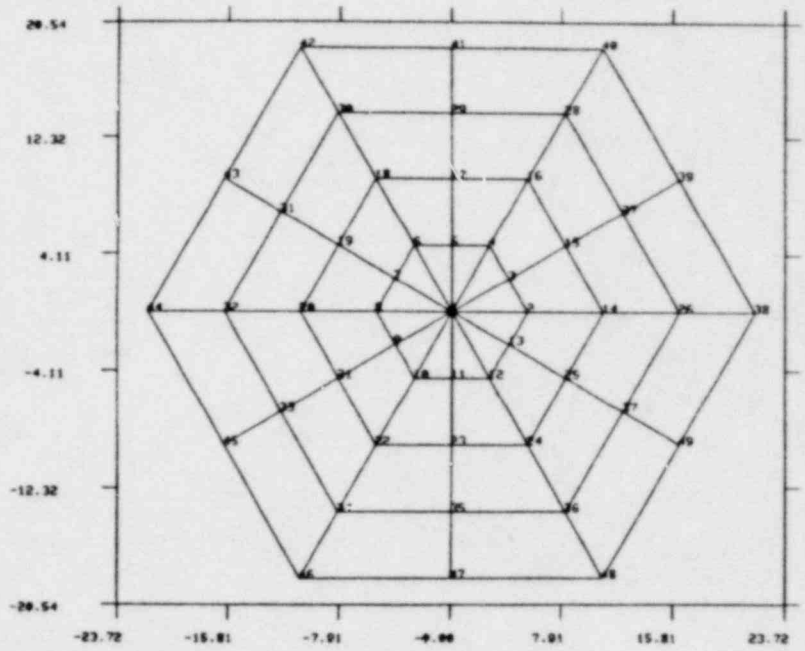

(b)

Fig. 85. Thermal and stress meshes for two-dimensional analysis.

PROBLEM 1, H = 30 BTU/FT^2·H·°F

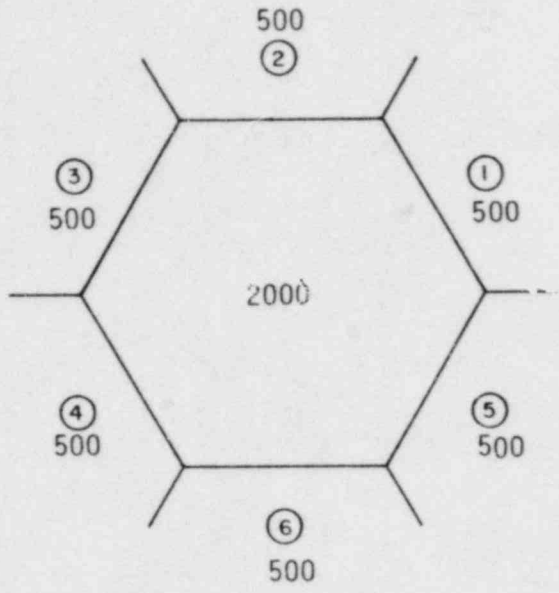

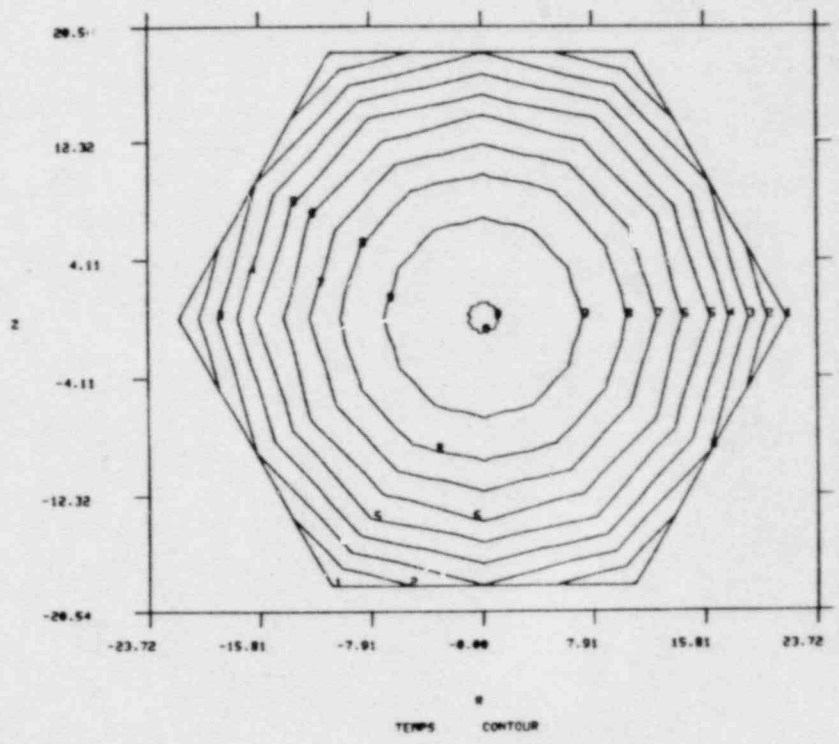

Fig. 86. Temperature contours for a hot block surrounded by six cold blocks.

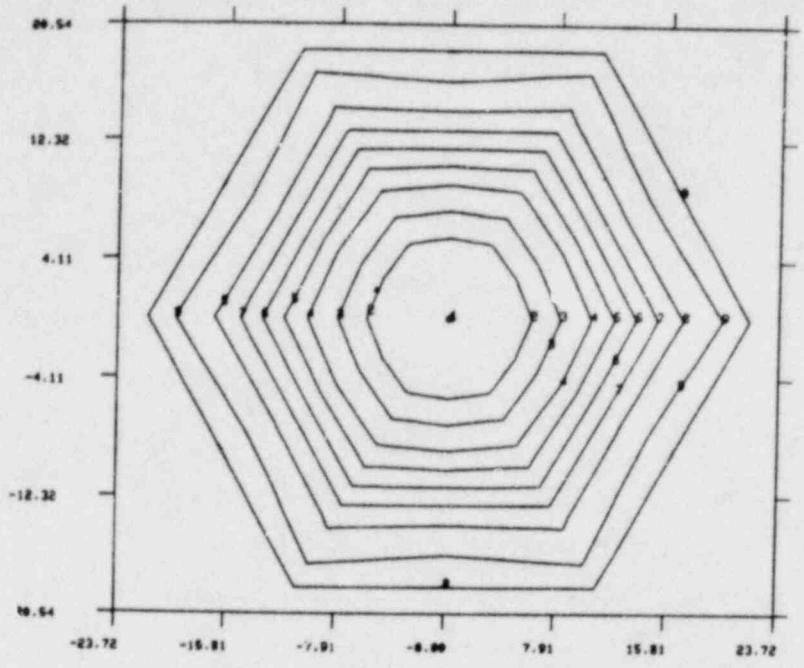

MAXIMUM PRINCIPAL STRESS

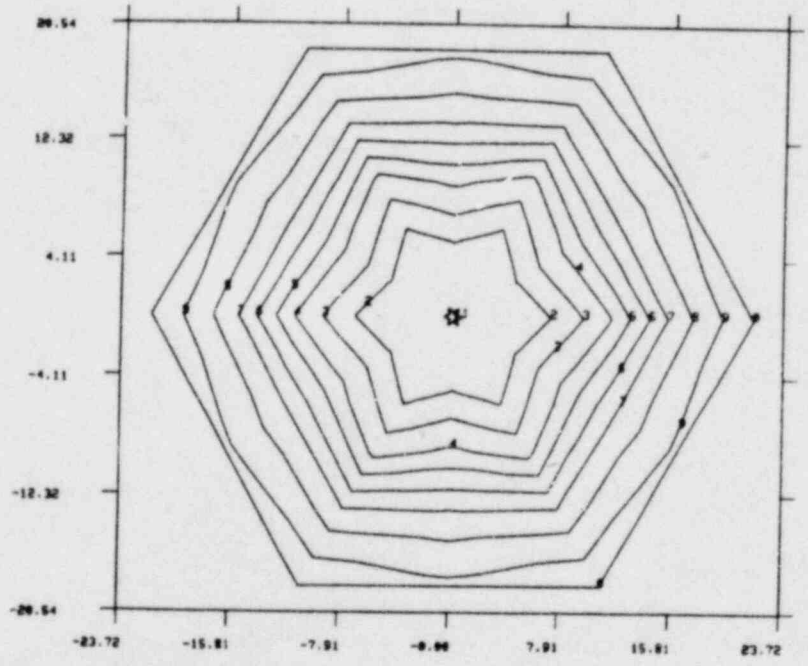

MINIMUM PRINCIPAL STRESS

Fig. 87. Stress contours for a hot block surrounded by six cold blocks.

PROBLEM 1, H = 30 BTU/FT^2·H·°F

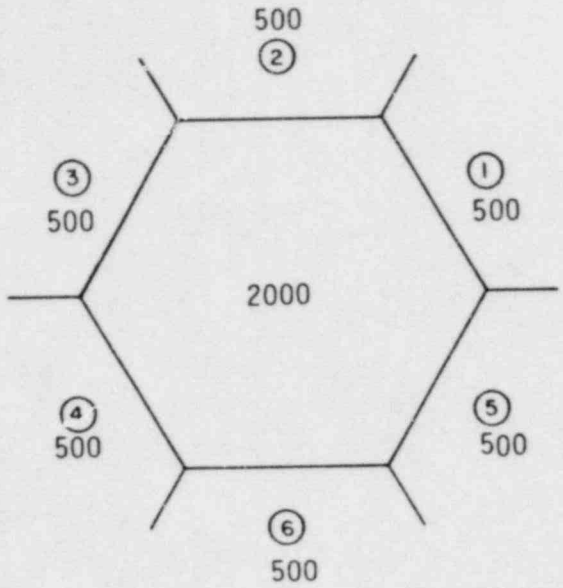

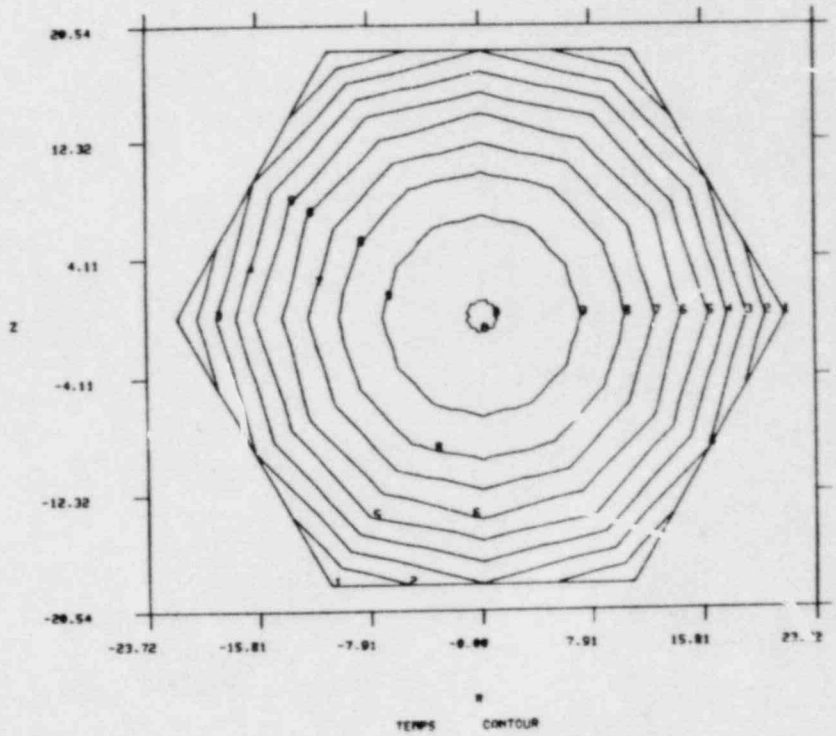

Fig. 88. Temperature contours for worst case region of Fig. 84.

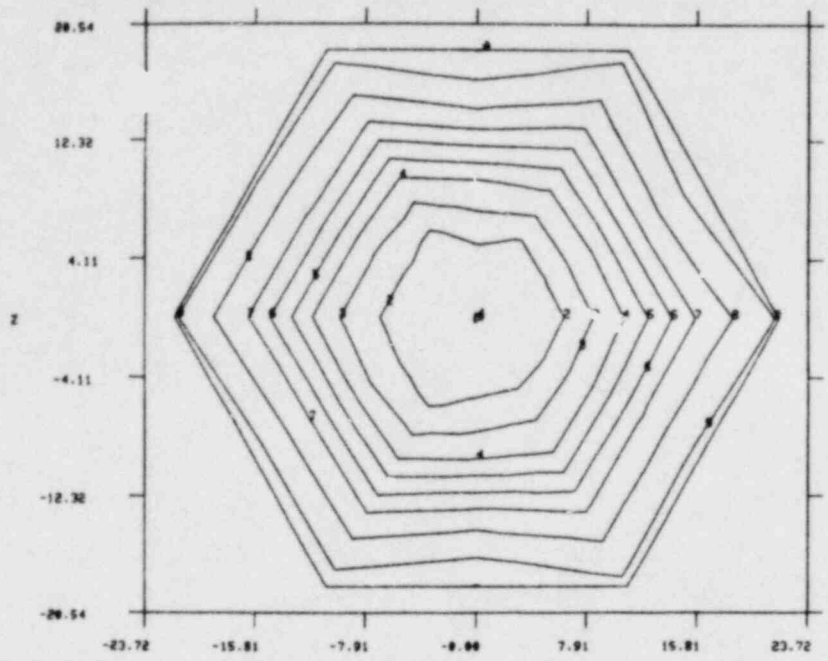

MAXIMUM PRINCIPAL STRESS

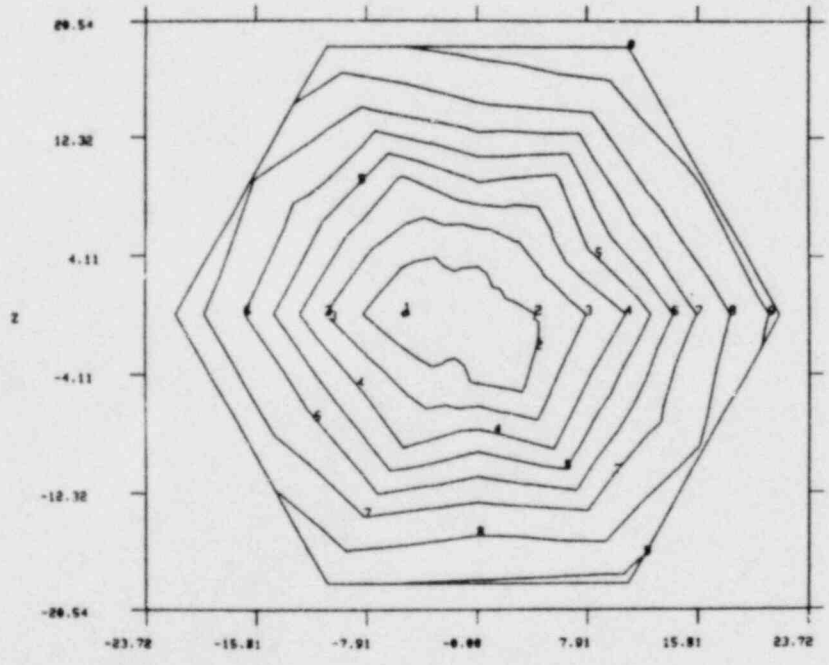

MINIMUM PRINCIPAL STRESS

Fig. 89. Stress contours for worst case region of Fig. 84.

blocks and the worst case gradient of Fig. 84, respectively. The lateral surface heat transfer coefficient was taken to be 30 BTU/ft^2-h-°F for both cases. The maximum principal stress was 560 psi for the worst case gradient, which is about one-half of the minimum ultimate tensile strength of CSB graphite.

The Fort St. Vrain CSB is a truly three-dimensional structural element which is complicated by the presence of six coolant holes and a lug-keyway mechanism for lateral coupling. To examine the complete problem we have carried along in parallel with the two-dimensional model a detailed three-dimensional thermal stress analysis of the Fort St. Vrain CSB to determine its response during a FWCD accident. The computer codes ADINAT and ADINA are being used to perform the finite element calculations. Temperature fields, maximum and minimum principal stresses, and maximum shear stresses are computed and displayed in three-dimensional format.

Even though the CSB is not perfectly cyclically symmetric, we have assumed that a single 60° segment can be used to study the complete block (see Fig. 90). A relatively coarse mesh is being used to solve the three-dimensional problem. The model has 847 node points and 126 finite elements. Once the overall stress field is calculated, we plan to use either fracture mechanics methods or very detailed two-dimensional models to determine stress concentration factors near the lugs and keyways on the block. Figure 91 shows the finite element mesh for the three-dimensional model, which is used for both the thermal and stress field calculations.

For the transient thermal calculations, heat transfer is allowed by convection and conduction into and out of the top of the block. Convection heat transfer is calculated for the coolant holes, the cavity, and the bottom surface of the block. At the outside surface of the block, heat is transferred by convection and radiation to the neighboring block, and by conduction through the helium coolant.

Initial temperatures and transient boundary conditions again are obtained from data supplied by Sid Ball. Because the ORNL model used for the calculations is fairly coarse, we will need to study some of the boundary conditions parametrically.

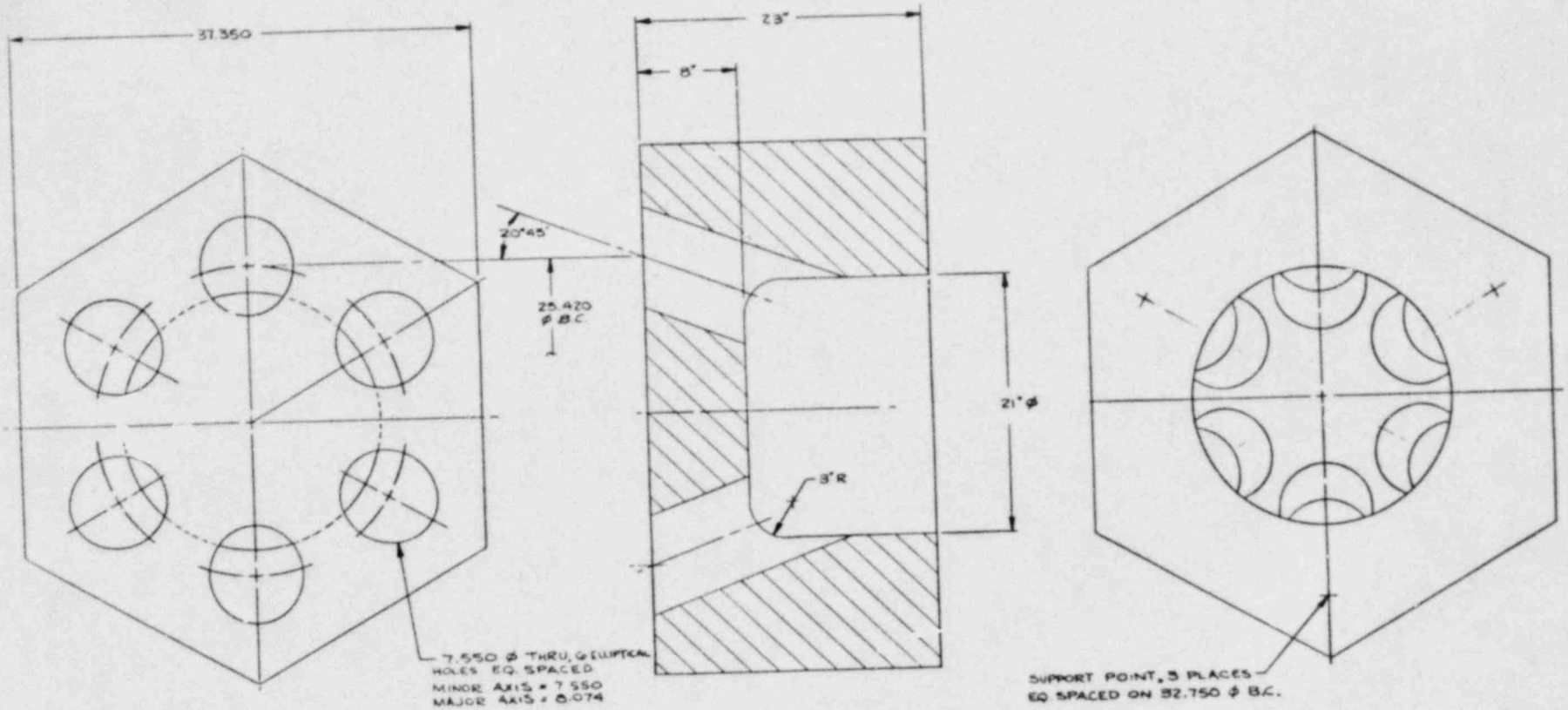

Fig. 90. Simplified support block schematic.

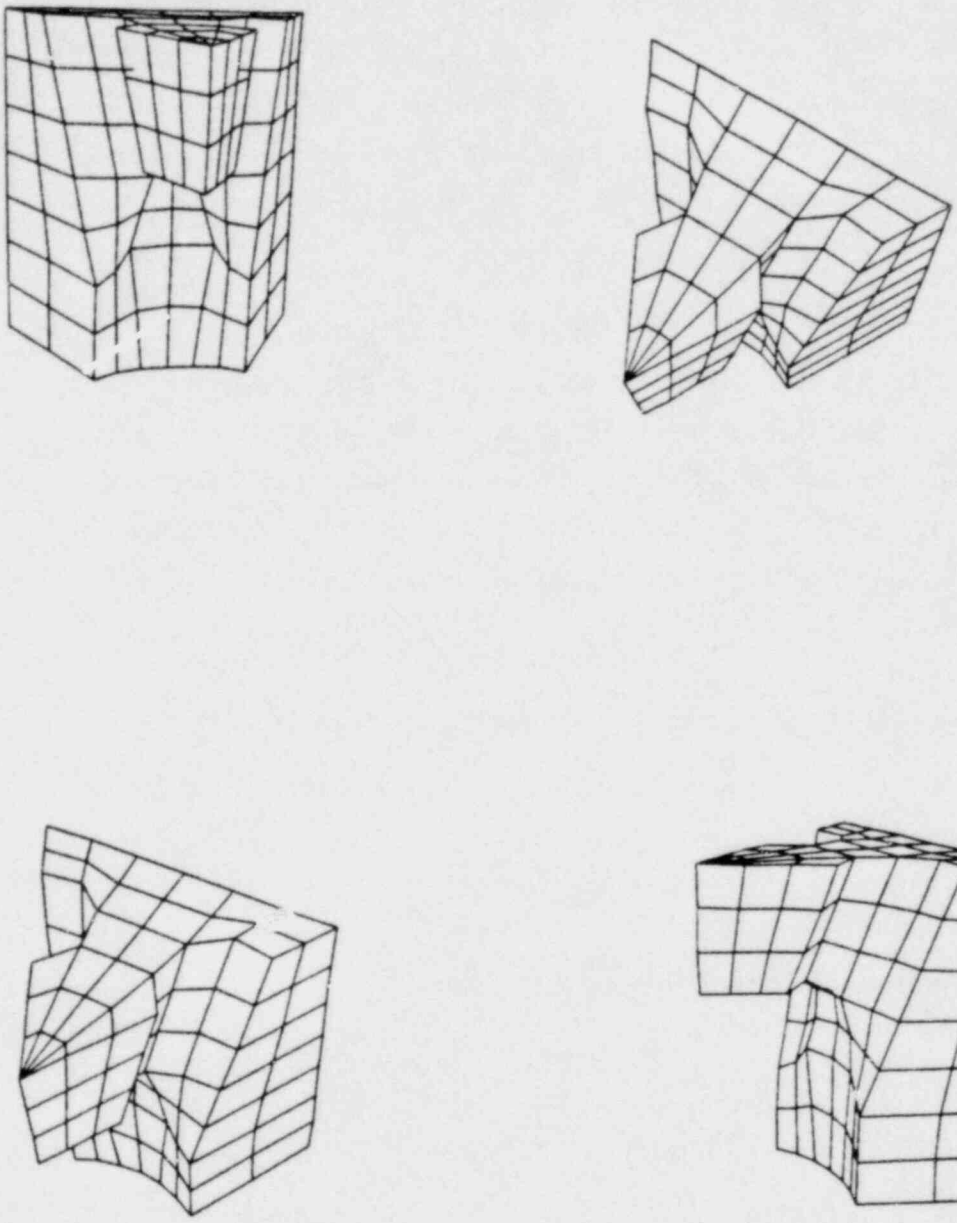

Fig. 91. Views of the three-dimensional finite element mesh.

To date, we have performed one full steady-state analysis to compare the three-dimensional calculations with those made using the two-dimensional model. The block was loaded with a heat flux into the top of 34.5 BTU/hr-ft^2. Heat was convected away from the block on the outer surface with a heat transfer coefficient of 30 BTU/ft^2-h-°F. Figure 92 gives the resulting temperature field and Fig. 93 shows a contour plot of the maximum principal stresses.

2. HWR Seismic Investigation

(J. G. Bennett and R. C. Dove, Q-13)

During the present quarter, work began on the investigation of potential safety issues associated with the HWR primary system pressure boundary adequacy for seismic conditions. Relevant documents were procured and reviewed.[56-58] Following this review, the design of the CANDU-PHW (which may serve as a model for a US-produced HWR) was investigated to determine

1. the limits of the primary pressure boundary,
2. the components within this boundary that would be excited by a seismic event, and
3. the way in which these components might be analyzed.

The primary pressure boundary includes

1. the calandria tubes,
2. the lattice and control tubes,
3. the end fittings,
4. all of the piping between the end fittings and the steam generators, and
5. the fueling machine (one on each end of the reactor) when they are connected to the end fittings for refueling.

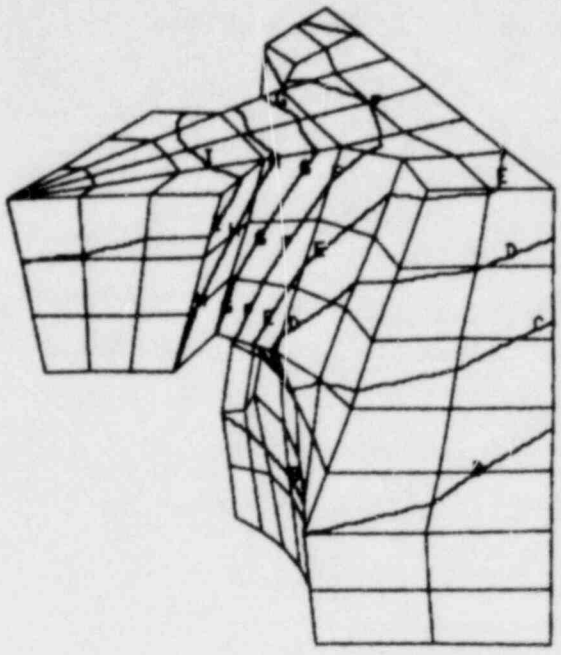

Fig. 92. Temperature contours.

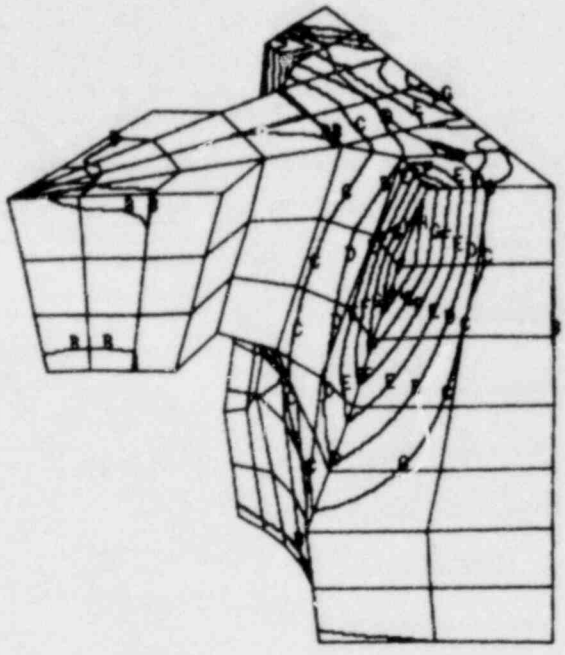

Fig. 93. Maximum principal stress contours.

The piping (item #4, above) already has been identified as requiring extensive redesign if it is to meet NRC requirements. Therefore this program will investigate the components and structures identified in items #1, #2, #3, and #5 as listed above.

Four specific problems have been identified.

1. The need to determine the acceleration-time history applied to the calandria tank (and hence to all of the components which it supports). There is a biaxial spring flexseal joint between the calandria tank and the concrete vault that supports it. Because of this spring connection, the acceleration-time history applied to the reactor base may be considerably modified before being applied to the calandria tank and its contents.

2. The response of the calandria tubes as fixed end beams. A preliminary calculation indicates that during a seismic event, these tubes will be deflected to the extent that they will impact with the shut-off rods that extend vertically through the tank in positions between the calandria tubes.

3. The response of the end fittings as cantilevered beams. The response of the end fittings will be examined when not connected to the fueling machine.

4. The response of an end fitting/refueling machine head when these two items are connected.

After the appropriate seismic input (problem #1 above) and the motion responses have been determined, the stresses developed at critical areas such as pressure seals and joints can be investigated through detailed finite element modeling of the individual components

In accordance with the program plan for this work, all initial calculations will be made using currently available or readily constructed analytical models. However, their shortcomings will be investigated and recommendations will be made concerning the time and cost required for extension of current methods of analysis.

3. PCRV Analysis

(C. A. Anderson and C. R. Wiig, Q-13)

A version of NONSAP-C[59] will be compiled for the CRAY computer. With the CRAY version, large three-dimensional creep problems can be set up and economically run. Because of the requirement that we must store up to 42 pieces of information per integration point of the mesh, our past creep calculations have been confined to relatively small problems.

B. Phenomena Modeling and Systems Analysis

(K. R. Stroh, Q-6)

This task is concerned primarily with the development, verification, and application of Gas-Cooled Reactor (GCR) consolidated plant simulation computer programs. The Composite HTGR Analysis Program (CHAP) consists of a model-independent systems analysis mainframe called LASAN and model-dependent linked modules, each representing a component, subsystem, or phenomenon of the overall HTGR plant model. The Los Alamos Systems ANalysis program (LASAN) has steady-state,

transient, and frequency-response solution capabilities. The standardized modular structure of LASAN/CHAP facilitates modification of component models, modification of solution algorithms, and the addition of new features. An initial version (CHAP-1) modeled the 3000 MW(t) HTGR. A version modeling the Fort St. Vrain HTGR is being developed (CHAP-2).

During this period, the CHAP-2 code and its systems analysis mainframe LASAN were converted to FTN/LTSS. We will no longer support the nonstandard CHAT/LRLTRAN versions. Conversion to FTN required the removal of some module variables from large core memory (LCM), increasing the small core memory (SCM) field length. Subsequent removal of LASL-dependent plot routines from the code has, however, resulted in code that takes less SCM than before. All plot variables are available on disk files for postprocessing. These two changes should greatly enhance the exportability of CHAP and other LASAN-based codes. An added benefit results because the FTN compiler generates code that executes considerably faster. The LASAN documentation will be published as soon as the changes resulting from the CHAT to FTN conversion are incorporated.

CHAP-2 development during this period has concentrated on the steam generator and reheater modules. Coding to model the cold-reheat steam attemperation was incorporated. The reactor test procedure used to set the attemperator flows for Fort St. Vrain was obtained from Public Service Co. of Colorado. We will simulate this procedure with the CHAP-2 code to determine the appropriate fixed valve positions. The steam generator/reheater calculational modules have been refined with the incorporation of the modified Grimison coefficients from the Fort St. Vrain steam generator air-flow tests, and the curvature correction factor (for heat transfer and friction correlations) based on the work of Ito, Mori, and Nakayama.[60] LASL reports are being prepared to document the water property package and the generic shell and tube heat exchanger package.

A new feature was added to LASAN to enhance the CHAP-2 development effort. It is now possible, through the use of subroutine ADJUST and the Symbolic Input Package (SIP), to create a simple differential

equation for any variable in the code having an external name by adding an appropriate "A-card" to the Input Data File (IDF). The "A-card" is free-format, except that the ordering is mandatory and an A must appear in column 1. The form is as follows:

A VNAME MEASUR SETPNT TCONST MOD OMIN OMAX ,

where the A in column 1 alerts the SIP that this card is input to subroutine ADJUST. VNAME and MEASUR are, respectively, the external BCD names of the variable to be adjusted (e.g., CKO for an orifice coefficient) and the plant parameter to be achieved (e.g., POUT for an outlet pressure). SETPNT is a free-format floating point number to which MEASUR is compared. TCONST, OMIN, and OMAX are free-format floating point numbers that define the equation time constant and minimum and maximum constraints on the new state variable VNAME. MOD is an integer number corresponding to the number of the module in which the calculation should be done. The equation derivative is of the form:

$$DT = \frac{\text{INITIAL VALUE(VNAME)}}{\text{SETPNT} \cdot \text{TCONST}} \cdot (\text{VALUE(MEASUR)} - \text{SETPNT}) \ .$$

The sign of DT may be changed by entering TCONST as a negative number.

V. GAS-COOLED FAST REACTOR SAFETY EXPERIMENTS

(D. L. Hanson, Q-13)

The basic assembly module of the GCFR is a subassembly comprising 264 fuel rods, 6 corner support rods, 1 central rod (instrumented), and their surrounding duct. The duct is a right hexagonal cylinder. The purpose of this out-of-pile experimental program is to demonstrate the behavior of the GCFR core module in the event of loss of core coolant flow and subsequent shutdown of reactor power to the level resulting from decay heat alone. The LOFA will be simulated in the steel melting and relocation test (SMART) and the loss-of-pressure accident will be simulated in the depressurized accident condition (DAC) test. These experiments require the development of an electrically heated fuel rod simulator capable of delivering 2 kW of power while operating at surface temperatures exceeding 1 650 K and the development of a fixture that will permit operation of an ensemble of 438 such rods (1 core module thermally guarded by segments of the six surrounding modules) at helium pressures up to 9.1 MPa. This guarded core module (GCM) fixture will be the largest in a sequence of four test fixtures developed in the course of this program. The others are:

- Ten-inch, single-rod fixture,
- One-meter, seven rod fixture, and
- Full-length subgroup (FLS) 37-rod fixture.

The GCM fixture will be used first for the SMART and subsequently for the DAC test.

A. Program Planning

(D. L. Hanson, Q-13)

The FLS3 test system configuration is evolving as a result of a continuing dialogue between LASL and General Atomic (GA) personnel. It has been agreed that the system operating pressure will not exceed

6.6 MPa because of the limitation imposed by the thin wall of the available heat exchanger. It also has been agreed that the input power for the nondestructive tests will be kept below the value used for the destruct test and that the upper temperature limit of the most temperature-sensitive component in the lower piping will not be exceeded. Because GA personnel do not wish to throttle the natural convection flow, these restrictions will preclude the higher cladding temperatures that they initially had requested for the convective tests.

B. Analysis

1. FLS3 Convective Loop Flow, Closed Form Approximation

(D. L. Hanson, Q-13)

The steady-state, free-convection driven mass flow expected in the FLS3 test system first was estimated by means of a simplistic analytical model comprising two vertical legs with connecting horizontal pipes at top and bottom and filled with pressurized helium at two different uniform temperatures. If the gas in the upper, hotter section of this circuit is at uniform temperature, T_H, and that in the lower section is at uniform temperature, T_C, and if the temperature transition points in the two vertical legs are separated by a vertical distance of Δz, then for smooth channels and turbulent flow, the resulting mass flow can be expressed by

$$\dot{m} = \left\{ 6.33 \frac{g\,|\Delta\rho\Delta z|}{\left(\frac{\mu}{\rho}\right)^{1/4} \sum \frac{\Delta L}{D_h^{5/4} A^{7/4}}\Bigg)_H + \left(\frac{\mu}{\rho}\right)^{1/4} \sum \frac{\Delta L}{D_h^{5/4} A^{7/4}}\Bigg)_C} \right\}^{4/7}, \quad (12)$$

where the symbols have their customary fluid dynamic meanings and basic SI units (i.e., without prefix multipliers, except kg) are used throughout. Substituting this mass flow estimate into an expression of the form

$$\dot{Q} = \frac{1}{\zeta}\left[1 - \exp(-\zeta U A_W)\right] \; (T_{in} - T_s) \; , \qquad (13)$$

where

$\dot{Q}$ = heat loss rate, W,

ζ = $1/(\dot{m}\ Cp)_{he} - 1/(\dot{m}\ Cp)_{coolant}$, $K \cdot W^{-1}$,

U = overall heat transfer coefficient, $W \cdot m^{-2}\ K^{-1}$,

A_W = heat transfer surface area inside duct, m^2,

T_{in} = helium temp at the inlet to the component, K, and

T_S = heat sink (cooling water or ambient air) temp, K

yields an estimate for the heat loss from each component in the convection loop piping outside of the pressure vessel (T_{in} for each successive component is determined by computing T_{out} for the preceding one).

This procedure was used to test the adequacy of the available heat exchanger for FLS3 and to size the piping and insulation. The calculated mass flow rates for Δz = 5.2 m are approximately 0.03-0.04 kg/s over an input power range of 20-80 kW. Flow rate decreases with increasing power in this range.

2. FLS3 Convective Loop Heat Transfer Model

(D. Bennett, Q-13)

A more complete solution of the steady-state operating conditions of the FLS3 convective loop is based on pressure, input power, and overall loop dimensions as independent system variables. This numerical approach increments around the loop shown in Fig. 94 to solve for the required helium mass flow and the corresponding pressure vessel inlet and outlet temperatures.

Heat transferred to the helium in the pressure vessel is specified by the simulated fuel rod power gradient. Heat losses in the water-cooled heat exchanger and in the insulated and uninsulated piping are computed from $Q = UA\ \Delta T$ where the overall film coefficient U is

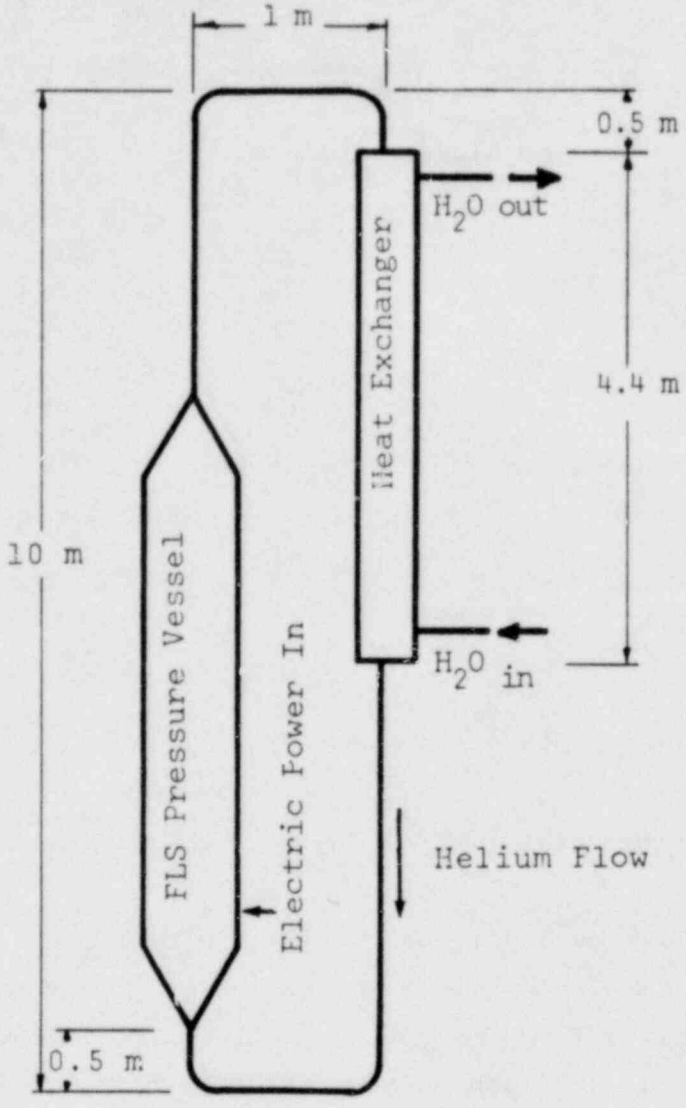

Fig. 94. Initial model for calculation of flow and temperatures due to natural convection of the FLS 3 test loop.

evaluated by common Nusselt number and, where applicable, Grashof number correlations. The momentum, friction, and buoyancy forces affect the static pressure in the constant area sections according to

$$\Delta P = \left(\frac{\dot{m}}{A}\right)^2 \Delta\rho + f \frac{L}{D} \frac{1}{2} \rho V^2 + \rho g \Delta z \ , \qquad (14)$$

where the symbols have their customary meanings. The friction coefficient f is evaluated as a function of the Reynolds number. Additional static pressure losses from entrances, exits, bends, etc., are determined from velocity head loss coefficients obtained from Ref. 61.

Preliminary results are indicated in Tables XI and XII. The possibility of double-valued mass flows and temperatures for the same input power is being studied.

3. FLS3 Differential Pressure Measurements

(D. L. Hanson, Q-13)

GA has requested differential pressure measurements across the FLS rod bundle and across the heat exchanger. A preliminary assessment of this problem was made, based on the analytical models described above and assuming an isothermal vertical leg in the external tubing necessary to connect each differential pressure transducer. At the 50 kW power level for free convection at a pressure of 6.6 MPa, for example, it was found that the transducer connected across the heat exchanger was found to indicate about 250 Pa while the one across the rod bundle would indicate only about 10 Pa. The difficulty of this latter measurement is indicated by the fact that it is equivalent to measuring the differential hydrostatic pressure of a column of atmospheric air only 1 m high, and the measured pressure differential is only one part per million of the pressure level. Because of this, we plan to employ a daisy chain of four differential transducers connecting at four pressure taps around the FLS3 loop. The sum of the measurements thus made should be zero, thus providing an independent test for credibility of the measurements.

TABLE XI

PRELIMINARY FLS3 CHARACTERISTICS AT 65 ATMOSPHERES OF HELIUM PRESSURE

Power, kW	Pressure Vessel inlet temp, K	Pressure Vessel outlet temp, K	System mass flow, kg/s
25	373	488	0.041 9
30	387	522	0.040 9
35	402	573	0.039 8
40	416	617	0.038 8
45	430	660	0.037 7
50	444	706	0.036 9

TABLE XII

PRELIMINARY FLS3 CHARACTERISTICS AT 30 ATMOSPHERES OF HELIUM PRESSURE

Power, kW	Pressure Vessel inlet temp, K	Pressure Vessel outlet temp, K	System mass flow, kg/s
25	398	658	0.018 6
30	416	733	0.018 3
35	434	819	0.017 5
40	453	928	0.016 3
45	473	1 059	0.014 8
50	494	1 247	0.012 8

4. Heater-Rod/Spacer-Grid Interaction

(J. G. Bennett and F. Ju, Q-13)

The simplified finite element convective heat transfer code and the efficient beam column finite element for thermoelastic deformation that were discussed in the previous report[14] have now been coupled together. The geometry of the two-dimensional sample problem devised to illustrate the effect of coupling is shown in Fig. 95a. It consists of a rectangular cavity containing a symmetrically positioned, plane heating generating wall. The pinned ends of the wall are allowed to rotate freely up to an angular displacement of 0.015 rad (to simulate a loose-fitting fuel rod in a stiff spacer grid). One vertical wall of the cavity is maintained at constant temperature. The other three walls are adiabatic.

This sample problem was devised as a crude representation of an axial segment of heater rod (the internal wall) between two spacer grids (the two pin joints) situated radially between the center of a rod bundle (the adiabatic vertical cavity wall) and its surrounding duct (the isothermal cavity wall). The resulting convective flow field and deformation of the internal wall are shown in Fig. 95b. With this successful coupling of the convective code and the finite thermoelastic element, a quantitative analytical tool for studying heater-rod/spacer-grid interaction is close at hand.

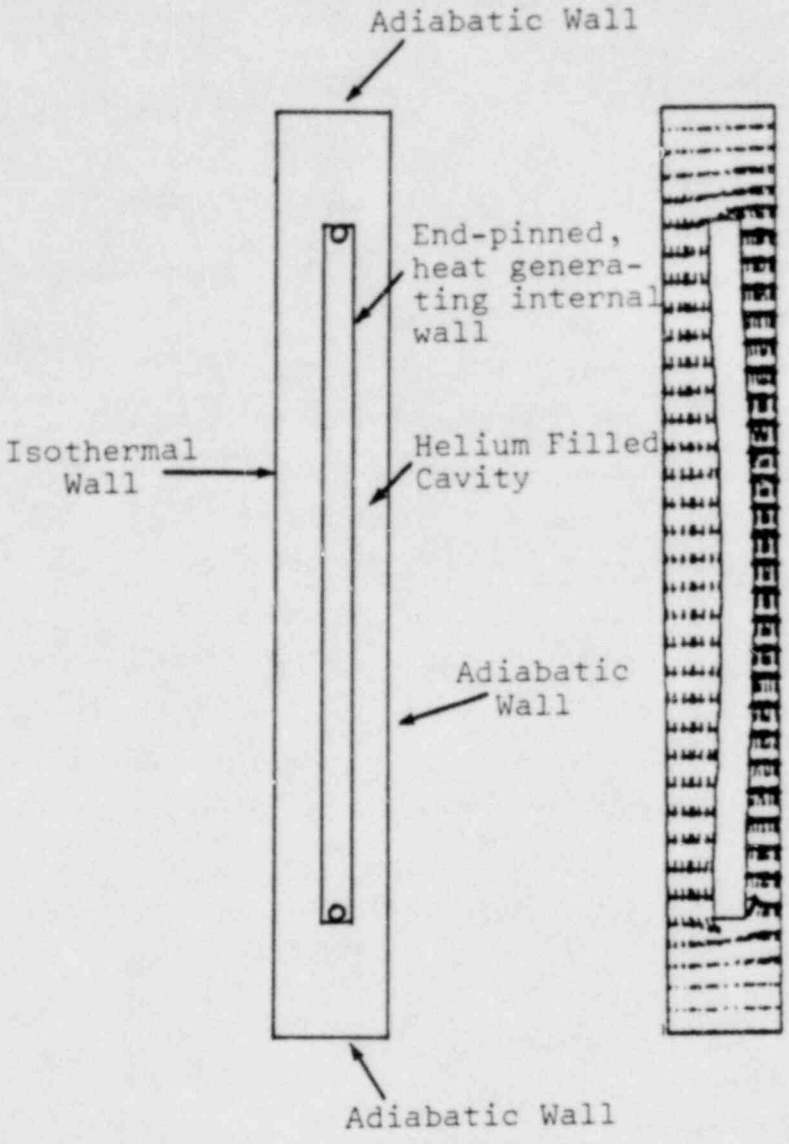

(a)

Initial geometry (two-dimensional).

(b)

Convective flow field and internal wall deformation.

Fig. 95. Sample problem combining the finite element convective code and the efficient beam column finite thermoelastic element.

C. Design

1. FLS3

(E. O. Ferdinand, D. Bennett, and D. L. Hanson, Q-13)

The available heat exchanger for FLS3 has a single tubular stainless steel gas passage 68.8 mm i.d. by 2.1-mm wall by 4.4 m long, surrounded by an annular water jacket. The width of the annulus is 3.1 mm. Calculations using the closed-form approximation described in Sec. V.B indicate that this heat exchanger will accommodate an input power to the test bundle of 50 kW at a helium pressure of 6.6 MPa, but to do so the bundle inlet temperature may exceed 400 K while the outlet temperature will be less than 750 K. The same calculations suggest the use of large piping to minimize pressure losses and to accommodate an effective thickness of internal insulation. For this reason, 146 mm i.d. (6 in.) schedule 80 pipe has been chosen for the gas conduit. In the hot leg of the circuit, this will be fitted internally with a fibrous alumina-silica insulation having 146 mm o.d. and 76 mm i.d. Drawings are being made for the flange transition pieces required for adapting the piping to the heat exchanger and the test fixture.

2. GCM Preheater

(W. E. Dunwoody, Q-13)

We plan to use the 27-rod FLS3 test fixture as a preheater in the SMART tests. The power supply to be used for the preheater is a 250 v, 2 000 A dc generator. LASL Group CMB-6 is making carbon and mixtures of carbon and graphite heater rods so that we can match the heater rod resistance at operating temperatures to our power supply. Results of testing candidate electrode formulations are presented in Sec. V.F. We could probably use any of these materials by properly selecting the diameter to give a suitable overall resistance. The final material section will be made from mechanical considerations and fabrication properties.

3. First 271-Rod GCM Experiment (SMART I)

(A. J. Giger, Q-13 and J. Churchman, SD-2)

Design was completed for the upstream electrical connections for the experiment, from the power crossover through the pressure vessel (PV) power pass through. This includes upstream connections to the guard heaters.

A particular problem in this area is the PV power pass through. This item must carry 17.5 kA, be sealed against 9.1 MPa, be water cooled, and have correct alignment for connection to a part that moves slightly during testing (electrical connection in the support frame). A seal system using a filled teflon part and "O" rings will allow some motion of the 63.5-mm-diam, internally cooled, copper rod to accommodate differential thermal expansion between PV and support frame. A short, thin section copper bellows will allow bending to align the rod. This thin section, which terminates on a long nut into which the rod will thread, cools by conduction to the rod. A flexible crossover transmits power to the upstream end of the guard heaters and allows for differential motion. Detailed drawings of parts in this area are 25% complete. The experiment's downstream electrical connections were redesigned to avoid the possibility of having to develop a ball contact joint while retaining high contact losses. The slip joint-ball connection to the experiment top was replaced with a multiple layered zig-zag flexing copper lead composed of 23 layers, 0.76 mm thick by 203 mm wide.

Cooling within the GCM PV has been limited to the support frame and the two power pass throughs. Components not related to the cooling loops will be exposed to the temperature of their environs. Circuit components will have [illegible] generation and little chance for cooling. For noncooled electrical components for GCM experiments the design approach is operation in a time-limited transient. One hour has been set as the maximum operating time, 30 min as the minimum, when operating at 4.6% of GCFR-rated power (FLS-1 and FLS-2 test times were 6.9 and 12.7 min, respectively).

Reduction in ohmic heating is done most effectively by use of high conductivity materials. This is illustrated by Figs. 96 and 97,

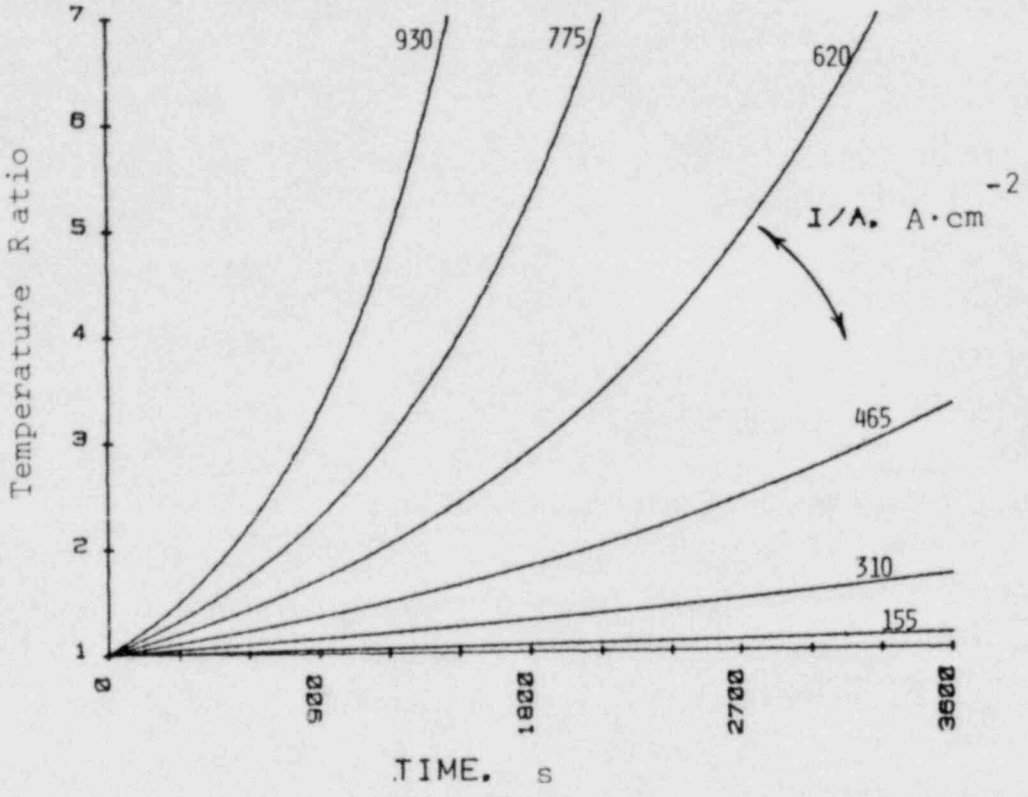

Fig. 96. Final-to-initial temperature ratio vs time for copper components during adiabatic heating due to electrical conduction.

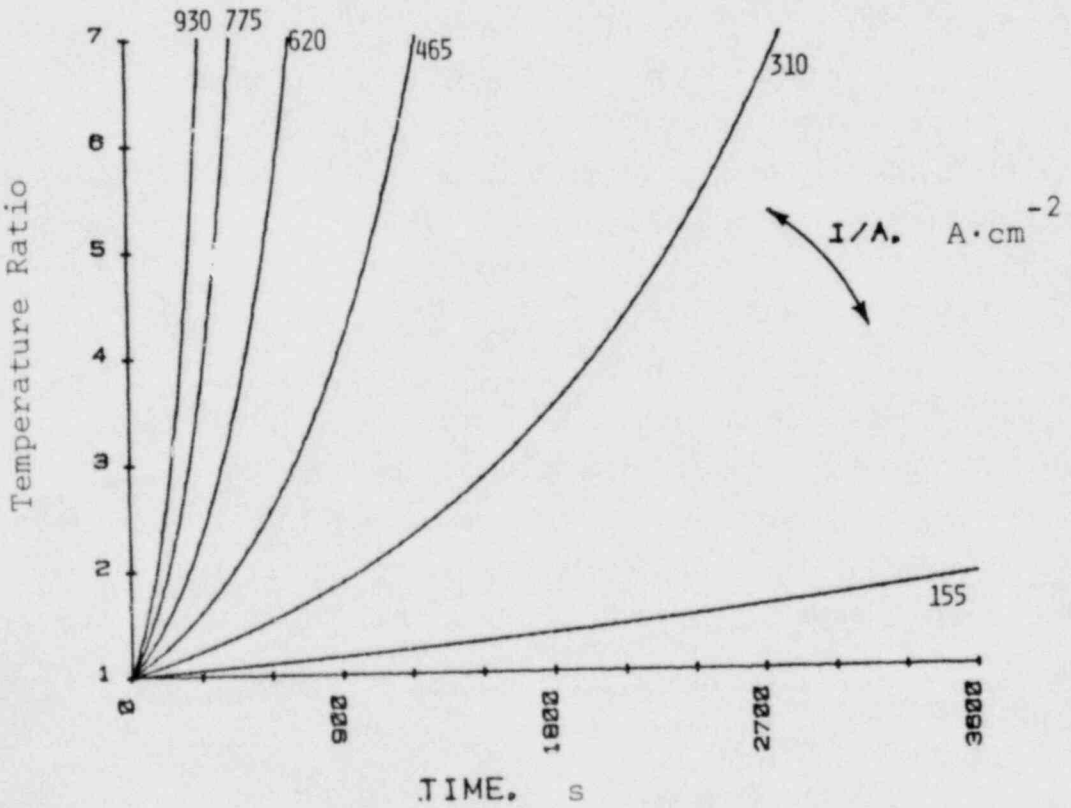

Fig. 97. Final-to-initial temperature ratio vs time for molybdenum components during adiabatic heating due to electrical conduction.

for copper and molybdenum, respectively. The figures show the ratio of final-to-initial temperature as a function of time with current density a parameter.

A final review of shunt design was made before fabrication. Minor changes were incorporated.

Evaluation of a previous component test shows that approximately 25 W contact heating occurs at each heater rod slip joint with the graphite. These slip joints are imbedded in the shunts. An additional 6.6 kW of heating thus has been identified in an area previously thought to have 2.0. Gas cooling of the shunt bolts is a possibility to cope with this problem if the thermal capacitance in this area proves inadequate.

D. Procurement and Fabrication

1. FLS3

(E. O. Ferdinand and J. H. Anderson, Q-13)

An order for 15.2 m of type ASH alumina-silica insulating cylinders has been placed with Aircar Fibrous Ceramics. This insulation is in 305-mm-long cylinders, 146 mm o.d. by 76 mm i.d. This dimension should readily allow insertion into the 146 mm i.d. (6 in.) schedule 80 pipe. The only cutting will be for pieces that have to be inserted in elbows, etc.

An order has been initiated for four differential pressure transducers and their associated electronics units from MKS Instruments, Inc. Two transducers each of 133-Pa and 1 330-Pa ranges are being ordered.

2. SMART I Test Assembly

(A. J. Giger, Q-13 and J. Churchman, SD-2)

Delivery was taken on 1 000 clad end fittings and retainers. These parts, from a local vendor, are of very high quality.

Two jig-bored straightness gauges for the alumina sleeves were received but were rejected, as they were only straight within 0.165 and 0.178 mm. The requirement is 0.038 mm. A local procurement was made of a gauge made from clad tubing. In mock up, this gauge checked straight within 0.008 mm. Lack of this gauge has held up delivery on the 4150 Al_2O_3 insulation sleeves that have been completed by Coors but await inspection for straightness.

Spline plates and fittings have been shipped to LASL.

Module support frame insulation and the insulation spring insulators have been received.

Fabrication of the support frame is about 80% complete.

All guard heater shells have been received.

An order was placed for fabrication of the experiment support plate.

3. Main Power Extension Cables

(J. H. Anderson, Q-13)

A purchase request has been initiated for four 5 000 MCM (0.000 25 m^2 cross-sectional area) water-cooled copper cables, each approximately 8.5 m long. These will extend the dc power from the bus terminal in Test Cell 1 to the proximity of the GCM fixture in the high bay. By using two conductors for each current direction, the guard heater current (7 500 A) can be supplied at a different voltage than the center module current (10 000 A) if this appears necessary to compensate for radial outward heat loss from the guard heaters. The cables are rated at 11 500 A each.

4. GCM Pressure Vessel

(W. E. Dunwoody, Q-13)

The guarded core module pressure vessel has been received and installed in the high bay addition to Test Cell 1.

E. Assembly, Installation, and Verification

GCM Pressure Vessel

(J. H. Anderson and R. E. Ortega, Q-13)

The Guarded Core Module pressure vessel was hoisted into place in the high bay by a large, portable crane (the 2 Mg capacity of the high bay bridge crane was inadequate for this operation). Access by the crane to the interior was gained by removing the roof of the building. The vessel was subsequently shimmed to within 0.03 mm of vertical over its 5 m length and was fastened in place.

F. Testing

1. X-Ray Techniques

(D. Bennett, Q-13; L. A. Bryant, M-1; and A. Hasenkamp, SLA)

A full-scale, cross-sectional model of the 271-pin array with hexagonal duct, guard heaters, and rod cladding was used to determine x-ray feasibility for SMART testing. Two sources from M-1 were tried, with varying success. A 300-keV source, capable of real-time imagery, had insufficient energy to produce any image of the model. The 2.3-MeV source produced a very satisfactory image with good density and resolution. However, this system is limited in that it produces an image only once every 45-60 s.

Further investigation indicated that SLA had real-time x-ray image capabilities. The GCM mockup was sent to Mr. Art Hasenkamp at SLA and testing using a 250-Ci ^{60}Co source. The source was used in conjunction with a Delcalix, a device employing television fluoroscopy. A complex set of optics reproduces the screen image light onto the cathode of a light intensifier tube. The light then moves through coupling optics and finally to an Isocon television camera tube. The signal can then be observed, real time, on a television monitor, and recorded on a video tape recorder.

Results from the SLA experiments indicate that the ^{60}Co source/ Delcalix combination has definite possibilities in GCFR experimental

work. Resolution of three to four channels between rod rows on either side of center is moderately good. A large source of about 1 000 Ci would provide better resolution and contrast. The availability of such a source is being investigated.

2. GCM Preheater Electrodes

(R. E. Ortega, J. H. Anderson, W. E. Dunwoody, and D. Bennett, Q-13)

Three different preheater electrode formulations were prepared by LASL Group CMB-6 and tested in the ten-inch fixture. All were mixtures of graphite and amorphous carbon. The electrical resistivities exhibited by the sample electrodes at 1 475 K were:

Mixture Per Cent		Resistivity
Carbon	Graphite	(μΩ·m)
100	0	41.6
75	25	31.8
50	50	22.7

For comparison, the resistivity of the graphite used for the core region of the simulated GCFR fuel rods is about 8 μΩ·m. These results indicate that good impedance-matching of the preheater load to the existing power supply is possible.

VI. REACTOR SAFETY ANALYSIS

(R. G. Gido, Q-6)

The following section summarizes the progress in the area of reactor safety analysis funded by the NRC, Division of Systems Safety (DSS).

TMI-2 Severe Overcooling Transient

(G. J. E. Willcutt, Jr., Q-6)

We have completed a TRAC code simulation of a 250 s TMI-2 severe overcooling transient. We assumed that the reactor is initially at 100% power and that the feedwater flow rate remains at the 100% level, even after the reactor is scrammed 0.5 s into the transient, thus providing severe overcooling. When the hot-leg pressure decreases to 11.14 MPa at 48.1 s, the reactor coolant pumps are tripped and one HPIS pump is turned on with its output split between the two loops. With the reactor coolant pumps turned off, the flow in each of the loops coasts down rapidly to about 23% of the full-power flow in the first 100 s and then decreases slowly to about 14% of the full-power flow by 250 s.

The void fraction in the hot leg attached to the pressurizer peaks at about 12.6% at 67 s and then decreases to 4% by the end of the transient. In the other hot leg, the void fraction never exceeds 3% because it is not as closely connected to the pressurizer void source. In the vessel, the void fraction stays below 3.5% except in the top head where it increases to over 80%. There is no evidence from the TRAC run that bubbles in the loops stop the natural convection flow.

This transient was modeled using the TMI-2 accident model repo·ted[14] with the changes indicated in Table XIII.

TABLE XIII

TMI-2 SEVERE OVERCOOLING TRANSIENT CHANGES FROM TMI-2 ACCIDENT MODEL[14]

1. 100% power level.

2. Scram at 0.5 s.

3. Full feedwater flow for entire transient.

4. Different steam generator secondary pressure curve.

5. Use of conventional pressurizer model with surge pipe connected to hot leg instead of detailed break model used in TMI-2 accident analysis. No pressurizer heaters were used.

6. The letdown system was not assumed to be operational.

7. Only one HPIS pump was used with its flow split between the two loops.

8. When the pressure in the hot leg drops below 11.14 MPa, the reactor coolant pumps are tripped and the HPIS is turned on.

9. The three-cell pump model was separated into a single cell pipe between the steam generator and pump and a two-cell pump model to better represent the pump momentum source.

10. A loss coefficient was added to the pump after it was tripped to improve the TMI-2 pump resistance model during coastdown and natural convection.

REFERENCES

1. J. F. Jackson and M. G. Stevenson, "Nuclear Reactor Safety Quarterly Progress Report for the Period January 1-March 31, 1979," Los Alamos Scientific Laboratory report LA-7867-PR, NUREG/CR-0868 (June 1979).

2. D. A. Mandell, A. C. Peterson, K. A. Williams, and J. L. Creel, "TRAC Pretest Calculations of LOFT Nuclear Test L2-3," American Nuclear Society Trans., 33, 490-491 (November 1979).

3. J. M. Cozzuol, M. A. Langerman, R. F. Farman, and T. K. Larson, "Semiscale Test S-02-8 Mini-Topical for Standard Problem Five," EG&G Idaho, Inc. report TREE-NUREG-1015 (November 1976).

4. J. C. Vigil and K. A. Williams, "TRAC-P1A Developmental Assessment," Los Alamos Scientific Laboratory report LA-8056-MS, NUREG/CR-1059 (October 1979).

5. TRAC-P1A, "An Advanced Best Estimate Computer Program for PWR LOCA Analysis," Los Alamos Scientific Laboratory report LA-7777-MS, NUREG/CR-0665 (May 1979).

6. G. A. Berna, M. P. Bohn, and D. R. Coleman, "FRAPCON-1: A Computer Code for the Steady-State Analysis of Oxide Fuel Rods," EG&G Idaho, Inc. report CDAP-TR-78-032-R1 (November 1978).

7. L. J. Siefken, M. P. Bohn, S. O. Peck, and J. A. Dearien, "FRAP-T5, A Computer Code for the Transient Analysis of Oxide Fuel Rods," EG&G Idaho, Inc. report NUREG/CR-0840 (June 1979).

8. B. A. Boley and J. H. Weiner, Theory of Thermal Stresses, (John Wiley and Sons, Inc., New York, 1960).

9. P. Mast, "The Los Alamos Failure Model (LAFM): A Code for the Prediction of LMFBR Fuel Pin Failure," Los Alamos Scientific Laboratory report LA-7161-MS (March 1978).

10. S. W. Hatch and D. A. Mandell, "An Improved Gap Conductance Model for the TRAC Code," Los Alamos Scientific Laboratory informal report LA-UR-79-2945 (November 1979).

11. M. McCormick-Barger, "Experiment Data Report for LOFT Power Ascension Test L2-2," EG&G Idaho, Inc. report NUREG/CR-0492 (February 1979).

12. A. W. Bennett, G. F. Hewitt, H. A. Kearsey, and R. K. F. Keys, "Heat Transfer to Steam-Water Mixtures Flowing in Uniformly Heated Tubes in Which the Critical Heat Flux has been Exceeded," Atomic Energy Research Establishment report AERE-R5373 (1967).

13. "MATPRO-Version 11: A Handbook of Materials Properties for Use in the Analysis of Light Water Reactor Fuel Rod Behavior," Idaho National Engineering Laboratory report NUREG/CR-0497 (February 1979).

14. J. F. Jackson and M. G. Stevenson, "Nuclear Reactor Safety Quarterly Progress Report for the Period July 1-September 30, 1979," Los Alamos Scientific Laboratory report LA-8[illegible]1-PR, NUREG/CR-1201 (December 1979).

15. R. Seban, "UC-B Reflood Program: Experimental Data Report," Electric Power Research Institute report NP-743 (April 1978).

16. E. R. Rosal, C. E. Conway, and M. C. Krepinevich, "FLECHT Low Flooding Rate Skewed Test Series Data Report," Westinghouse Electric Corporation report WCAP-9108 (1977).

17. E. R. Rosal, "FLECHT Low Flooding Rate Cosine Test Series Data Report," Westinghouse Electric Corporation report WCAP-8651 (1975).

18. W. G. Craddick, "PWR Blowdown Heat Transfer Separate Effects Program Data Evaluation Report - Heat Transfer for THTF Test Series 100," Oak Ridge National Laboratory report ORNL/NUREG-45 (September 1978).

19. C. B. Mullins, "PWR Blowdown Heat Transfer Separate Effects Program Data Evaluation Report - THTF Test Series II," Oak Ridge National Laboratory report ORNL/NUREG-53 (April 1979).

20. C. B. Mullins, Oak Ridge National Laboratory to J. S. Gilbert, Los Alamos Scientific Laboratory, personal communication (June 25, 1979).

21. L. S. Tong, US Nuclear Regulatory Commission, personal communication, July 26, 1979.

22. "Preliminary Calculation Related to the Accident at Three Mile Island," Los Alamos Scientific Laboratory informal report LA-UR-79-2425 (August 1979).

23. J. F. Jackson and M. G. Stevenson, "Nuclear Reactor Safety Quarterly Progress Report for the Period April 1-June 30, 1979," Los Alamos Scientific Laboratory report LA-7968-PR, NUREG/CR-0993 (August 1979).

24. "TRAC News," Number 1, July 1979.

25. J. P. Adams, "Quick-Look Report on LOFT Nuclear Experiment L3-1," EG&G Idaho, Inc. report LOFT-5057, Project No. P 394 (November 1979).

26. "Specifications-LOBI Preprediction Exercise," Technical Note No. 1.06.01.79.25, Commission of the European Communities, Joint Research Centre, ISPRA Establishment (February 1979).

27. "Corrigendum and Addendum to Specification-LOBI Preprediction Exercise," Commission of the European Communities, Joint Research Centre, ISPRA Establishment (May 22, 1979).

28. "Single-Phase Performance Characteristics of the LOBI-Pump," "Technical Note No. 1.06.01.79.80, L. Piplies and J. Bachler, C.E.C.-J.R.C., ISPRA Establishment (August 1979).

29. J. F. Jackson and M. G. Stevenson, "Nuclear Reactor Safety Quarterly Progress Report for the Period July 1-September 30, 1978," Los Alamos Scientific Laboratory report LA-7567-PR, NUREG/CR-0522 (1978).

30. M. L. Reocreux, "Experimental Study of Steam-Water Choked Flow," Proceedings of a Specialists Meeting on Transient Two-Phase Flow, Toronto, Canada (August 3-4, 1976).

31. N. Abuaf, G. A. Zimmer, B. J. C. Wu, and O. C. Jones, Jr., "Nonequilibrium Phase Change Studies," Light Water Reactor Safety Information Meeting, Gaithersburg, MD (November 1979).

32. C. Y. Chen, "Filtration of Aerosols by Fibrous Media," Chem. Rev. 55, 595 (1955).

33. "Reactor Safety Study: An Assessment of Accident Risks in US Commercial Nuclear Power Plants," US Nuclear Regulatory Commission report WASH-1400, NUREG-75/014 (1975).

34. Ford-MITRE, "Nuclear Power Issues and Choices," Nuclear Energy Policy Study Group report (Ballinger Publishing Co., 1977).

35. "Risk Assessment Review Group Report to the USNRC," US Nuclear Regulatory Commission report NUREG/CR-0400 (1978).

36. J. R. Ireland, "Three Mile Island System Thermal-Hydraulic Analysis Using TRAC," submitted to the American Nuclear Society Topical Meeting on Thermal Reactor Safety (Knoxville, Tennessee, April 8-11, 1980).

37. W. L. Kirchner, J. R. Ireland, and P. K. Mast, "Fuel Thermal Damage Estimates for Three Mile Island," submitted to the American Nuclear Society Topical Meeting on Thermal Reactor Safety (Knoxville, Tennessee, April 8-11, 1980).

38. "Investigation into the March 28, 1979 Three Mile Island Accident by Office of Inspection and Enforcement," US Nuclear Regulatory Commission Investigative report 50-320/79-10, NUREG-0600 (August 1979).

39. "Analysis of Three Mile Island - Unit 2 Accident," Nuclear Safety Analysis Center report NSAC-1 (July 1979).

40. J. L. Straalsund, R. L. Fish, and G. D. Johnson, "Correlation of Transient-Test Data with Conventional Mechanical Properties Data," Nuclear Technology 25 (March 1975).

41. D. G. Hardy, "High-Temperature Expansion and Rupture Behavior of Zircaloy Tubing," Topical Meeting on Water Reactor Safety (Salt Lake City, Utah, March 1973).

42. "Three Mile Island Nuclear Station, Unit 2," License Application, FSAR, Vol. 1-10 (Metropolitan Edison Co., 1974).

43. V. S. Arpaci, Conduction Heat Transfer (Addison-Wesley Publishing Co., Reading, Massachusetts, 1966) pp. 76-83.

44. H. M. Chung, A. M. Garde, and T. F. Kassner, "LWR Safety Research Program Quarterly Progress Reports, Part III," Argonne National Laboratory report ANL-78-25, NUREG/CR-0089 (October-December 1977).

45. R. G. Steinke and P. Hodson, Los Alamos Scientific Laboratory, personal communication (September 21, 1979).

46. R. J. Page, C. L. Fink, P. A. Froehle, and A. B. Rothman, "Interim Report for TREAT Test H6," Argonne National Laboratory report ANL/RAS 78-44 (September 1978).

47. J. H. Scott, S. A. Chastain, T. T. Arey, and E. D. Jensen, "Preliminary Data Report: Postirradiation Examination of Fuel Pins PNL-10-23 and PNL-10-63," Hanford Engineering Development Laboratory report HEDL-TME 74-23 (May 1974).

48. C. W. Steward, C. L. Wheeler, R. J. Cena, C. A. McMonagle, J. M. Cuta, and D. S. Trent, "COBRA-IV: The Model and the Method," Battelle Pacific Northwest Laboratories report BNWL-2214 (July 1977).

49. L. Leibowitz, E. C. Chang, M. G. Chasanov, R. L. Gibby, C. Kim, A. C. Millunzi, and D. Stahl, "Properties for LMFBR Safety Analysis," Argonne National Laboratory report ANL-CEN-RSD-76-1 Supplement 1, LMFBR Safety (April 1976).

50. W. W. Marr, "COBRA-3M: A Digital Computer Code for Analyzing Thermal-Hydraulic Behavior in Pin Bundles," Argonne National Laboratory report ANL-8131 (March 1975).

51. M. Saito and T. G. Theofanous, "The Termination Phase of Core Disruptive Accidents in LMFBRs," presented at Specialists Workshop on Prediction Analysis of Material Dynamics in LMFBR Experiments, Los Alamos, March 13-15, 1979 (Los Alamos Scientific Laboratory, Los Alamos 1979) LA-7938-C; also presented at International Meeting on Fast Reactor Safety Technology, Seattle, Washington, August 19-23, 1979.

52. T. G. Theofanous, Purdue University, personal communication (October 1979).

53. S. W. Eisenhawer, "A Study of Heat Transfer from a Flowing Liquid to a Melting Wall," Proceedings of the International Meeting on Fast Reactor Safety Technology, Seattle, Washington (August 19-23, 1979).

54. E. J. Chapyak and V. S. Starkovich, "The Role of Similitude in the Design of LMFBR Safety Related Experiments," Proceedings of the International Meeting on Fast Reactor Safety Technology, Seattle, Washington (August 19-23, 1979).

55. R. V. Browning, D. G. Miller, and C. A. Anderson, "TSAAS: Finite Element Thermal Stress Analysis of Axisymmetric Solids with Orthotropic Temperature-Dependent Material Properties," Los Alamos Scientific Laboratory report LA-5599-MS (May 1974).

56. "Licensing Assessment of the CANDU Pressurized Heavy Water Reactor," United Engineers and Constructors, Inc., Philadelphia, Pennsylvania document COO-2477-4 (Vol. 2) (June 1977).

57. J. B. van Erp, "Preliminary Evaluation of Licensing Issues Associated with U.S.-Sited CANDU-PHW Nuclear Power Plants," Argonne National Laboratory report ANL-77-97 (December 1977).

58. "Candu Core Seismic Test - 1/5 Scale Model Seismic Tests," untranslated Japanese report EPDC-MISM (1979).

59. P. D. Smith and C. A. Anderson, "NONSAP-C: A Nonlinear Stress Analysis Program for Concrete Containments Under Static, Dynamic, and Long-Term Loadings," Los Alamos Scientific Laboratory report LA-7496-MS (October 1978).

60. D. P. Carosella, "Steam Generator Thermal Performance Model Verification by Use of Fort St. Vrain Nuclear Station Startup Test Data," General Atomic Company report GA-A14799 (June 1979).

61. I. E. Idel'chik, Handbook of Hydraulic Resistance-Coefficients of Local Resistance and of Friction, National Science Foundation report AEC-tr-6630 (1960).

DISTRIBUTION

	Copies
Nuclear Regulatory Commission, R4, R7, and R8, Bethesda, Maryland	875
Technical Information Center, Oak Ridge, Tennessee	2
Los Alamos Scientific Laboratory, Los Alamos, New Mexico	50
	927

☆U.S. Government Printing Office: 1980 — 677-115/103